Supporting Information

Triggering favorable energy landscape: a general approach towards highly-efficient and photostable organic solar cells

Kangning Zhang,[a] *Xiaoyan Du,**[a] *Jiawei Qiao,*[a] *Haixia Hu,*[a] *Wenqing Zhang,*[a] *Linghua Wang,*[a] *Mingsheng Gao,*[a] *Hang Yin,*[a] *Wei Qin,*[a] *Xiaotao Hao**[ab]

[a]School of Physics, State Key Laboratory of Crystal Materials, Shandong University, Jinan, Shandong 250100, P. R. China
E-mail:duxy@sdu.edu.cn (X.Y.D); haoxt@sdu.edu.cn (X.T.H)

[b]ARC Centre of Excellence in Exciton Science, School of Chemistry, The University of Melbourne, Parkville, Victoria 3010, Australia

Full Names of the Used OPV Materials

PM6: Poly[(2,6-(4,8-bis(5-(2-ethylhexyl-3-fluoro)thiophen-2-yl)-benzo[1,2-b:4,5-b’] dithiophene))-alt-(5,5-(1’,3’-di-2-thienyl-5’,7’-bis(2-ethylhexyl)benzo[1’,2’-c:4’,5’-c’] dithiophene-4,8-dione)]

L8-BO: 2,2 -((2Z,2Z) -((12,13-bis(2-ethylhexyl)-3,9-(2-butyloctyl)-12,13-dihydro-[1,2,5] thiadiazolo[3,4-e]thieno[2",3’:4’,5] thieno[2,3:4,5]pyrrolo[3,2 -g]thieno[2,3:4,5]thieno[3,2 -b]indole-2,10-diyl)bis(methanylylidene))bis(5,6-difluoro-3-oxo-2,3-dihydro-1H-indene-2,1-diylidene))dimalononitrile

Y6: (2,2′-((2Z,2′Z)-((12,13-bis(2-ethylhexyl)-3,9-diundecyl-12,13-dihydro-[1,2,5]thiadiazolo [3,4-e]thieno[2,"3″:4’,5′]thieno[2′,3′:4,5]pyrrolo[3,2-g]thieno[2′,3′:4,5]thieno[3,2-b]indole-2,10-diyl)bis(methanylylidene))bis(5,6-difluoro-3-oxo-2,3-dihydro-1H-indene-2,1-diylidene))dimalononitrile)

N3: 2,2 -((2Z,2Z) -((12,13-bis(3-ethylheptyl)-3,9-diundecyl-12,13-dihydro-[1,2,5]thiadiazolo [3,4-e]thieno[2,3:4,5]thieno[2,3:4,5]pyrrolo[3,2 -g]thieno[2,3:4,5]thieno[3,2 -b]indole-2,10-diyl)bis(methanylylidene))bis(5,6-difluoro-3-oxo-2,3-dihydro-1H-indene-2,1-diylidene))dimalononitrile

BTP-eC9: 2,2 -[[12,13-Bis(2-butyloctyl)-12,13-dihydro-3,9-dinonylbisthieno[2,3:4,5] thieno[2,3:4,5]pyrrolo[3,2 -e:2,3 -g][2,1,3]benzothiadiazole-2,10-diyl]bis[methylidyne(5,6-

chloro-3-oxo-1H-indene-2,1(3H)-diylidene)]]bis[propanedinitrile]

PY-IT: (Poly[(2,2 -((2Z,2Z) -((12,13-bis(2-octyldodecyl)-3,9-diundecyl-12,13-dihydro[1,2,5] thiadiazolo[3,4e]thieno[2″,3″:4′,5′]thieno[2′,3′:4,5]pyrrolo[3,2-g]thieno[2′,3′:4,5]thieno[3,2-b]-indole-2,10-diyl)bis(methanylylidene))bis(5-methyl-3-oxo-2,3-dihydro-1H-indene-2,1-diylidene)) dimalononitrile-co-2,5-thiophene)

IT-M: 3,9-bis(2-methylene-((3-(1,1-dicyanomethylene)-6/7-methyl)-indanone))-5,5,11,11-tetrakis(4-hexylphenyl)-dithieno[2,3-d:2',3'-d']-s-indaceno[1,2-b:5,6-b']dithiophene

N2200: poly{[N,N'-bis(2-octyldodecyl)-naphthalene-1,4,5,8-bis(dicarboximide)-2,6-diyl]-alt-5,5′-(2,2′-bithiophene)}

Experimental Section

Materials

PM6, Y6, N3, BTP-eC9, PY-IT, IT-M, N2200 and PDINN were purchased from Solarmer Materials (Beijing) Inc. L8-BO was obtained from Hyper, Inc. V_2O_5 and LiF were supplied by Shanghai Aladdin Biochemical Technology Co., Ltd. PEDOT:PSS (Clevios PVP Al 4083) was purchased from Xi'an Polymer Light Technology Corp. All reagents and solvents including chloroform, methanol, 1,8-Diiodooctane (DIO) and 1-chloronaphthalene (CN) were purchased from Sigma Aldrich and used without further purification.

Device Fabrication and Measurements

***Device fabrication*:** Organic solar cells with the ITO/V_2O_5/PEDOT:PSS/active layer/LiF /PDINN/Ag configuration were fabricated according to the following procedure. The patterned indium tin oxide (ITO) glass substrates were sequentially cleaned by ultrasonication in detergent, deionized water, acetone, ethanol and isopropanol for 20 min each. The precleaned ITO glass substrates were treated in an ultraviolet-ozone chamber for 15 min. The V_2O_5 powder was dissolved in deionized water and stirred overnight to form its saturated solution. The V_2O_5 solution filtered with a 0.45 μm PTFE filter was deposited onto the ITO substrates at 2000 rpm for 50 s and baked at 150 °C for 5 min under ambient conditions. Then, PEDOT:PSS (Clevios

PVP Al 4083) filtrated through a 0.45 μm nylon filter was spin-coated on the V_2O_5 surface at 4000 rpm for 50 s and dried on a heating plate at 150 °C for 15 min. The PM6:L8-BO blend solution (1:1.2, wt%, 17.6 mg ml^{-1} in CF with 0.25% DIO), PM6:BTP-eC9 blend solution (1:1.2, wt%, 17.6 mg ml^{-1} in CF with 0.5% DIO), PM6:Y6 blend solution (1:1.2, wt%, 15.4 mg ml^{-1} in CF with 0.5% CN), PM6:N3 blend solution (1:1.2, wt%, 15.4 mg ml^{-1} in CF with 0.5% CN) and PM6:PY-IT blend solution (1:1, wt%, 14 mg ml^{-1} in CF with 1% CN) were prepared and stirred at 45 °C for at least 2 hours. The corresponding ternary blend solution were obtained by adjusting the doping ratio of IT-M or N2200 in acceptors. The PM6:acceptor (L8-BO, BTP-eC9, Y6 and N3) blend solution were spin-coated on top of the PEDOT:PSS layer at 3000 rpm for 30 s and treated with thermal annealing at 100 °C for 10 min in a high-purity N_2-filled glove box to form the active layers of ~110 nm. The PM6:PY-IT blend solution was spin-coated on top of the PEDOT:PSS layer at 3000 rpm for 30 s and treated with thermal annealing at 95 °C for 5 min to form the active layers of ~110 nm. After cooling to room temperature, a 1 nm LiF layer was deposited by thermal evaporation on the top of the active layers. A 5 nm PDINN (1 mg ml^{-1} in methanol) layer was spin-coated on the surface of LiF layer at 3000 rpm for 30 s. Finally, a 100 nm Ag electrode layer was deposited under high vacuum in an evaporation chamber. The active area of OPV devices defined by a shadow mask is ~4 mm^2. The hole-only devices were fabricated with a structure of ITO/V_2O_5/PEDOT:PSS /active layer/MoO_3/Ag. A 7.5 nm MoO_3 layer was thermally evaporated on the top of active layer. The electron-only devices were fabricated with a structure of ITO/ZnO/active layer/LiF/PDINN/Ag. The ZnO solution was spin-coated on the patterned ITO substrates at 4000 rpm for 50 s and baked under 200 °C for 1 hour in air.

Device measurements: The *J-V* measurements of OSCs were performed in an N_2-filled glove box by empolying a computer-controlled Keithley 2400 source under the illumination of AM 1.5 G irradiation (100 mW cm^{-2}) with a simulated solar simulator (SOFN INSTRUMENTS CO., LTD) at room temperature. The standard monosilicon solar cell was used to calibrate irradiation intensity of the simulated solar simulator. The EQE spectra was measured with a commercial 7-SCSpec test system. The encapsulated OSCs with different device structures were fabricated to conduct the photostability measurement under the continuous illumination of a 100 mW cm^{-2} white LED at room temperature.

The dark current characteristics of the hole-only and electron-only devices under forward bias were extracted to obtain charge carrier mobilities according to the space-charge-limited current (SCLC) method by the following equations,[1, 2]

$$J \times d = \frac{9}{8}\varepsilon_0\varepsilon_r\mu_0 exp(0.89\beta\sqrt{F})F^2$$

where J is the current density, d is the thickness of photoactive layer, ε_0 is the permittivity under vacuum (8.85×10^{-14} F/cm), ε_r is the average dielectric constant of photoactive layer (3), μ_0 is the zero-field hole or electron mobility, β is the Poole-Frankel (PF) slope, F is the the applied electric field.

Contact Angle Measurements

The surface energy parameters of materials used in this work can be obtained from contact angle measurements as below,[3, 4]

$$\gamma_{\mathrm{sol}}(1 + cos\theta) \ = \ 2\sqrt{\gamma_{\mathrm{sol}}^{d}\gamma^{d}} + 2\sqrt{\gamma_{\mathrm{sol}}^{p}\gamma^{p}}$$

where γ_{sol} is the surface energy, $\gamma_{\mathrm{sol}}{}^{\mathrm{d}}$ and $\gamma_{\mathrm{sol}}{}^{\mathrm{p}}$ are the dispersion and polar components, respectively, θ is the contact angle data.

The Flory-Huggins interaction value χ can be used to describe quantitatively the miscibility of materials as below,[3, 4]

$$\chi \propto (\sqrt{\gamma_{\mathrm{X}}} - \sqrt{\gamma_{\mathrm{Y}}})^2$$

where γ_{X} and γ_{Y} are the surface energy data of materials (X and Y), respectively.

Temperature-Dependent Photoluminescence (PL) Spectra Measurements

The encapsulated samples were placed in a liquid nitrogen chamber (TC280, East Changing, Inc.) to modulate the target temperature. The Ti:sapphire amplifier (Astrella, Coherent) supplies 800 nm pulse to excite the encapsulated samples and generate the PL signals. The temperature-dependent PL spectra were collected by a spectrometer (PG2000 Pro, Fuxiang Inc.) from fluorescence lifetime imaging microscopy (FLIM). The samples were encapsulated in a high-purity N_2-filled glove box for the temperature-dependent PL measurements.

Energy Barrier Calculation for Back Charge Recombination in BTP-based Acceptors

The energy barrier (E_a) for back charge recombination from electronic carriers to excitonic species can be calculated by fitting the temperature-dependent integrated PL intensity with the Arrhenius equation as below,[5]

$$I(T) = \frac{I_0}{1 + Aexp(-E_a/k_B T)}$$

where I_0 is the integrated PL intensity at 0 K, A is the frequency factor, k_B is the Boltzmann constant, T is the thermodynamic temperature.

Time-Resolved Photoluminescence (TRPL) Spectra Measurements

The TRPL spectra measurements were performed through a laser-scanned confocal imaging microscopy (Nanofinder FLEX2, Tokyo Instruments, Inc.) combined with a time-correlated single-photon counting (TCSPC) module (Becker & Hickl, SPC-150). The 800 nm pulsed laser was focused by an objective lens (50×) into a near diffraction-limited spot to excite the samples. A neutral density filter coupled with a power meter was used to regulate the excitation density at samples. The fluorescence signals were collected by the high-resolution detectors. Herein, the appropriate optical filters were employed to realize excitonic PL collection with > 800 nm for "edge state" emission. Furthermore, the two-dimensional (2D) TRPL scanning consists of

32×32 pixels. The samples were encapsulated in a high-purity N_2-filled glove box for TRPL measurements.

Excitonic and Electronic Emission Dynamics from TRPL Data in BTP-based Acceptors

In general, the PL intensity of neat BTP-based acceptor films is determined by the radiative recombination of the luminescent excitons and free carriers, which can be well described with a simple rate equation as shown in the following.[6, 7]

$$\frac{dn(t)}{dt} = -A_{nonrad}n(t) - B_{rad}n(t)^2$$

where n(t) represents the photoexcited density of excitons and free carriers, A_{nonrad} and B_{rad} stand for the nonradiative and radiative recombination constants, respectively.

The exact solution of the above equation is given as[6, 7]

$$n(t) = \frac{n(0)exp(-A_{nonrad}t)}{1 + \frac{B_{rad}}{A_{nonrad}}n(0)[1 - exp(-A_{nonrad}t)]}$$

where n(0) represents the density of excitons and free carriers generated by the pulsed laser at zero delay time. It is noted that the initial n(0) is proportional to the excitation intensity of the pump laser.

Steady-State and Ultrafast Transient Absorption (TA) Spectroscopy

The steady-state absorption spectra of the samples were recorded on an Agilent Cary 5000 spectrophotometer. Femtosecond transient absorption spectroscopy is based on an Ultrafast Helios pump-probe optical system (the nonlinear frequency mixing techniques, a fiber-coupled multichannel spectrometer and so on) combined with a regenerative amplified Ti:sapphire laser system from Coherent (800 nm, 100 fs, 7 mJ/pluse and 1 KHz repetition rate). The delay between pump and probe pulses can be controlled by a motorized delay stage, leading to a maximum delay time of 8 ns. The intensity of pump pulse can be tailored by a variable neutral-density filter wheel and measured by a power meter. The samples were encapsulated in a high-purity N_2-filled glove box for TA measurements.

Excitonic and Electronic Dynamics from TA Spectroscopy in BTP-based Acceptors

According to detection principles, the TA signals can reflect the population and depopulation processes from the sum of excitonic and electronic species.

The kinetics equation of excitons can be described as:[8]

$$\frac{dN_{EX}}{dt} = -k_{rad}N_{EX}(t) - k_{nonrad}N_{EX}(t) - k_{diss}N_{EX}(t) + k_{recomb}{N_{FC}}^{2}(t)$$

where N_{EX} and N_{FC} are the density of excitons and other electronic species (free carriers and/or polarons), respectively; k_{rad} and k_{nonrad} are the radiative and nonradiative recombination coefficients of excitons, respectively; k_{diss} is the dissociation rate constant of excitons; k_{recomb} is the coefficient of free carriers rebound into excitons.

The kinetics equation of free carriers and/or polarons can be described as:

$$\frac{dN_{FC}}{dt} = -k'_{nonrad}N_{FC}(t) + k_{diss}N_{EX}(t) - k_{recomb}{N_{FC}}^{2}(t)$$

where k'_{nonrad} is the nonradiative recombination coefficients of free carriers.

The kinetics equation of the total photocarriers can be obtained by the sum of depopulation rates of excitons and free carriers:

$$\frac{dN_{TP}}{dt} = \frac{dN_{EX}}{dt} + \frac{dN_{FC}}{dt} = -k_{rad}N_{EX}(t) - k_{nonrad}N_{EX}(t) - k'_{nonrad}N_{FC}(t)$$

where N_{TP} is the density of the total photocarriers.

Herein, we assume that all of photocarriers are excitons at initial time under close-bandgap excitation (800 nm). Therefore, the densities of the total photocarriers N_{TP}, excitons and free carriers can be expressed by

$$N_{EX} = (1 - \eta_{diss})N_{TP}$$

$$N_{FC} = \eta_{diss}N_{TP}$$

where η_{diss} is the exciton dissociation efficiency. As discussed above, the density of the total photocarriers can be further transformed into the following solution given by

$$\frac{dN_{TP}}{dt} = -k_{rad}N_{EX}(t) - k_{nonrad}N_{EX}(t) - k'_{nonrad}(\frac{\eta_{diss}}{1-\eta_{diss}})N_{EX}(t)$$

thus reading,

$$\frac{dN_{TP}}{dt} = -k_{rad}N_{EX}(t) - \left[k_{nonrad} + k'_{nonrad}\left(\frac{\eta_{diss}}{1-\eta_{diss}}\right)\right]N_{EX}(t)$$

herein, we defined k_{rad} and $\left[k_{nonrad} + k'_{nonrad}\left(\frac{\eta_{diss}}{1-\eta_{diss}}\right)\right]$ as k and γ, respectively. In addition, the relationship among k, γ and N_{EX} (t) can be described as[9]

$$N_{EX}(t) = \frac{N_{EX}(0)exp(-kt)}{1+\frac{\gamma}{k}N_{EX}(0)[1-exp(-kt)]}$$

Hence, the time-resolved density of the total photocarriers can be transformed into an exact solution as below

$$\frac{dN_{TP}}{dt} = -kN_{EX}(t) - \gamma N_{EX}(t) = -(k+\gamma)\frac{N_{EX}(0)exp(-kt)}{1+\frac{\gamma}{k}N_{EX}(0)[1-exp(-kt)]}$$

thus reading,

$$N_{TP}(t) = (k+\gamma)\frac{N_{EX}(0)exp(-kt)}{1+\frac{\gamma}{k}N_{EX}(0)[1-exp(-kt)]}$$

Accordingly, the population and depopulation processes of the total excitonic and electronic species can be well expressed by the above equation closely related to the excitonic dynamics in neat NFA films.

Electroluminescence (EL) Spectra Measurements

The EL measurements were performed by using a spectrometer (PG2000 Pro, Fuxiang Inc.) from fluorescence lifetime imaging microscopy coupled with the external voltage source. The applied voltage was controlled by a Keithley 2400 source meter.

Trap Density Measurements

The frequency-dependent capacitance (*C*) spectra were measured to quantitatively evaluate the evolution of trap density in binary and ternary OSCs with different device structures before and after continuous LED illumination. Herein, we transformed the frequency axis (*f*) into the energy axis (E_ω) as below[10]

$$E_\omega = kTln\left(\frac{2\upsilon_0}{\omega}\right)$$

where ω is the angular frequency calculated from $\omega = 2\pi f$, υ_0 is the attempt-to-escape frequency (10^9 Hz), k is the Boltzmann constant, T is the thermodynamic temperature. The trap density N_t (E_ω) at energy E_ω can be obtained from the derivative of the measured capacitance relative to the frequency described by[10]

$$N_t(E_\omega) = -\frac{V_{bi}}{qL}\frac{dC}{d\omega}\frac{\omega}{kT}$$

where q is the elementary charge, L is the film thickness, V_{bi} is the built-in potential calculated from the Mott-Schottky plot ($1/C^2$ versus V) as[10]

$$\frac{1}{C^2} = \frac{2(V_{bi} - V)}{q\varepsilon_0\varepsilon N_{ap}}$$

where V is the applied bias voltage, ε_0 is the permittivity under vacuum (8.85×10^{-14} F/cm), ε_r is the average dielectric constant of photoactive layer, N_{ap} is the doping parameter.

Then the energy distribution for the density of states (DOS) can be expressed by a Gaussian shape distribution given by[10]

$$N_t(E) = \frac{N_t}{\sqrt{2\pi}\sigma} exp\left[-\frac{(E_t - E)^2}{2\sigma^2}\right]$$

where N_t is the total density (cm^{-3}), E_t is the center of the DOS, σ is the disorder parameter.

FTPS-EQE and EQE$_{EL}$ Measurements

The FTPS-EQE measurements were performed by empolying a Fourier-transform infrared

(FTIR) spectrometer equipped with a halogen lamp light source and an external detector option. The photocurrent generated from the devices with illumination light modulated by the FTIR instrument was amplified by a low-noise current amplifier. The corresponding photocurrent spectrum were recorded by the FTIR software. The $\mathrm{EQE}_{\mathrm{EL}}$ spectra were collected through the devices (ELCT-3010, Enlitech).

Voltage Loss Analysis

The voltage losses can be determined as:[11, 12]

$$E_{loss} = E_g - qV_{OC} = \left(E_g - qV_{OC}^{rad}\right) + \left(qV_{OC}^{rad} - qV_{OC}\right)$$

where E_g and $V_{\mathrm{OC}}^{\mathrm{rad}}$ are the band gap and the V_{OC} when only considering radiative recombination with realistic absorption edges, respectively.

When all recombination is radiative, the related radiative limit V_{OC}^{rad} can be calculated according to the following equation[13, 14]

$$V_{OC}^{rad} = \frac{kT}{q}\ln\left(\frac{J_{SC}}{J_0^{rad}} + 1\right) = \frac{kT}{q}\ln(\frac{q\int_0^{\infty} EQE_{PV}(E)\cdot \emptyset_{AM1.5}(E)dE}{q\int_0^{\infty} EQE_{PV}(E)\cdot \emptyset_{BB}(E)dE} + 1)$$

Non-radiative recombination energy loss ($\Delta E_{\mathrm{nonrad}}$) is related to the luminescence efficiency of photovoltaic materials, which can be given by[15, 16]

$$\Delta E_{nonrad} = q\Delta V_{OC}^{nonrad} = -KTln(EQE_{EL})$$

where EQE_{EL} represents the electroluminescence (EL) quantum efficiency of the actual devices.

In addition, the E_g^{PV} can be extracted from the FTPS-EQE spectrum of OSCs according to the following equation,[17, 18]

$$E_g^{PV} = \frac{\int_a^b E\cdot P(E)\cdot dE}{\int_a^b P(E)\cdot dE}$$

where $P(E)$ is the distribution of a "band gap" ($P(E) = \mathrm{d}EQE/\mathrm{d}E$). It should be noted that the integral boundaries (a, b) have been selected where $P(a) = P(b) = 0.5\max[P(E)]$.

AFM and GIWAXS Characterizations

The tapping AFM measurements were performed by a Nano Scope IIIA instrument to collect the corresponding height images. The GIWAXS characterizations were performed by a Xeuss 2.0 instrument with a SAXS detector of Pilatus 300K. The distance of sample-to-detector and incidence light wavelength are 150 mm and 1.54189 Å, respectively. The *d*-spacing is the π-π stacking distance calculated from $d\text{-spacing} = 2\pi/q_{z(010)}$. The CCL value can be obtained from the Scherrer equation: $CCL = 2\pi k/FWHM$, where k and FWHM are the Scherrer constant of 0.9 and the full width at half the maximum of (010) π-π stacking peak in the OOP direction.

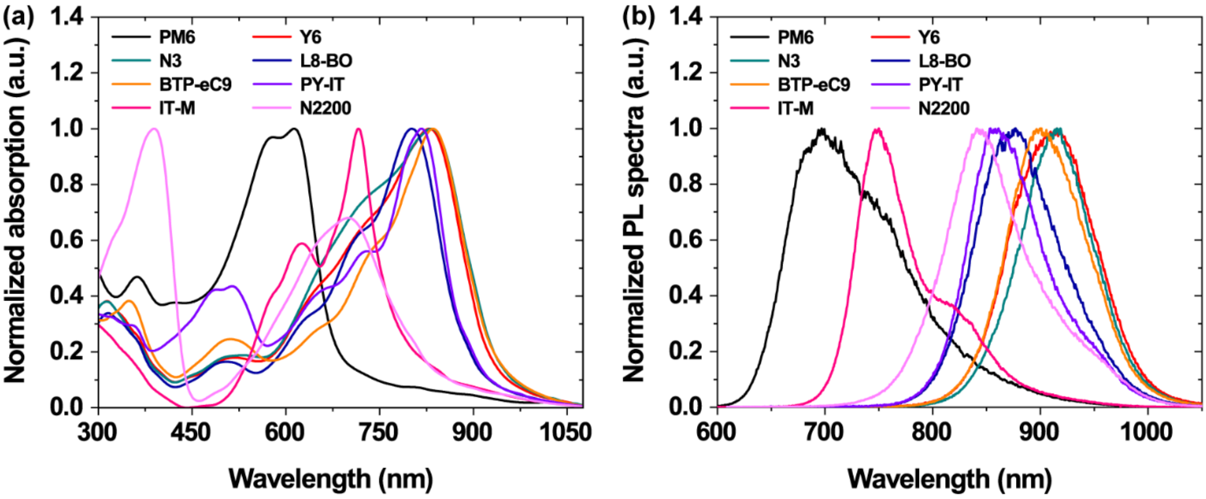

Fig. S1 Normalized (a) UV-vis absorption and (b) PL spectra of neat PM6, Y6, N3, L8-BO, BTP-eC9, PY-IT, IT-M and N2200 films.

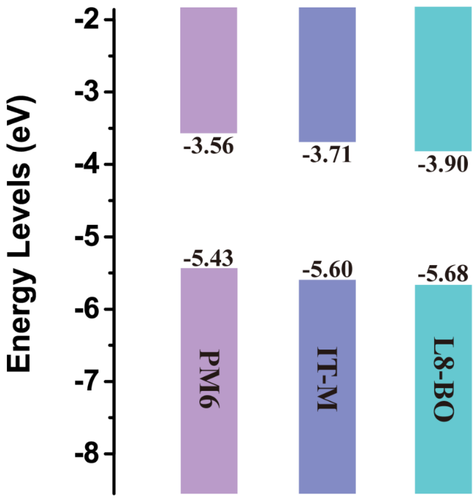

Fig. S2 Energy band diagram of PM6, IT-M and L8-BO.

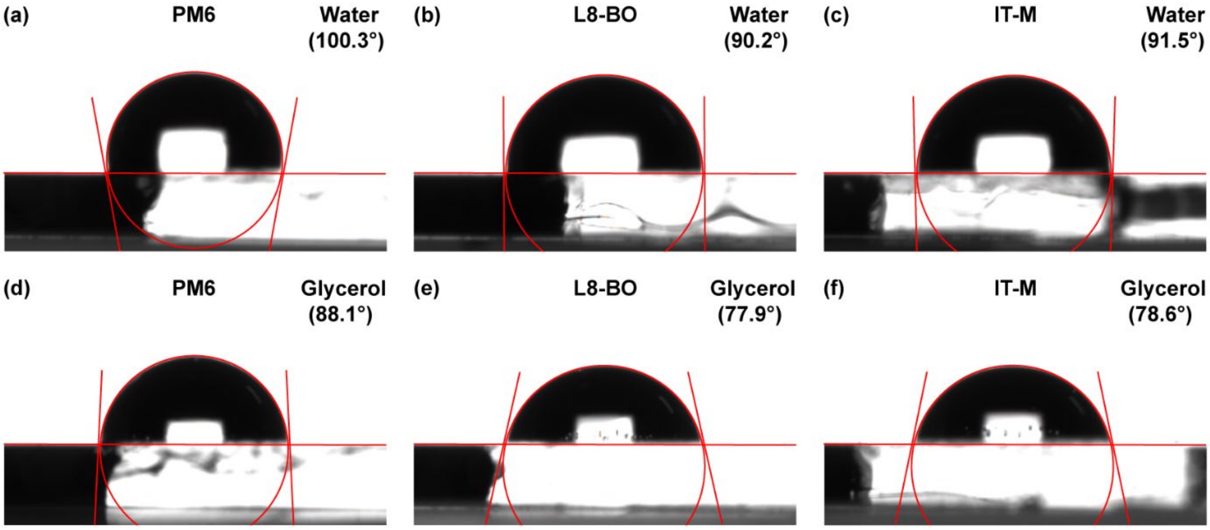

Fig. S3 Contact angle images of pure PM6, L8-BO and IT-M films with water and glycerol droplet on top.

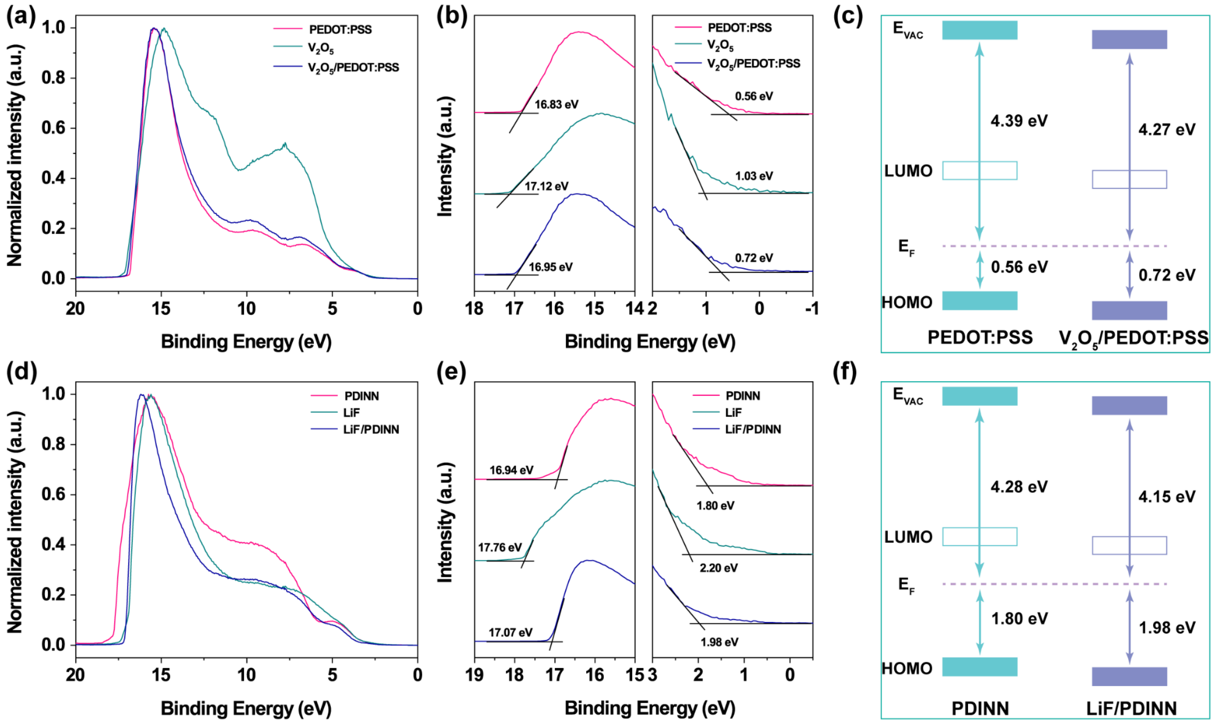

Fig. S4 (a-b) Ultraviolet photoelectron spectroscopy (UPS) spectra of PEDOT:PSS, V_2O_5 and V_2O_5/PEDOT:PSS bilayered interfaces. (c) The determined energy levels before and after inserting V_2O_5 between PEDOT:PSS and ITO. (d-e) UPS spectra of PDINN, LiF and LiF/PDINN bilayered interfaces. (f) The determined energy levels before and after inserting LiF between active layer and PDINN.

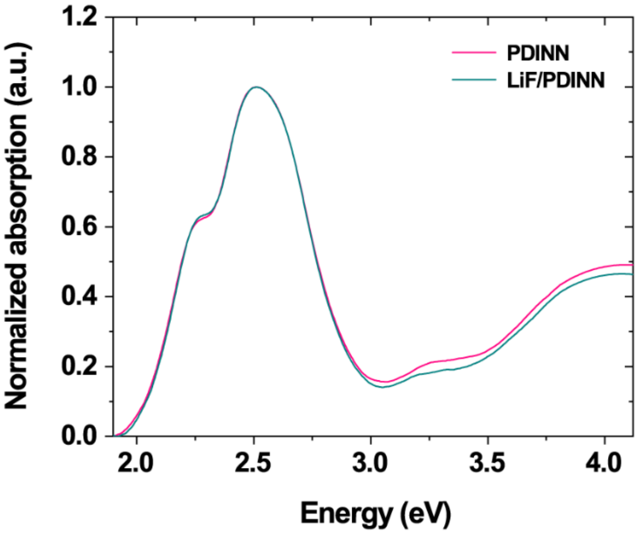

Fig. S5 Normalized absorption spectra of PDINN and LiF/PDINN bilayered interfaces. The bandgap of PDINN and LiF/PDINN bilayered interfaces was experimentally determined to be about 2.02 eV.

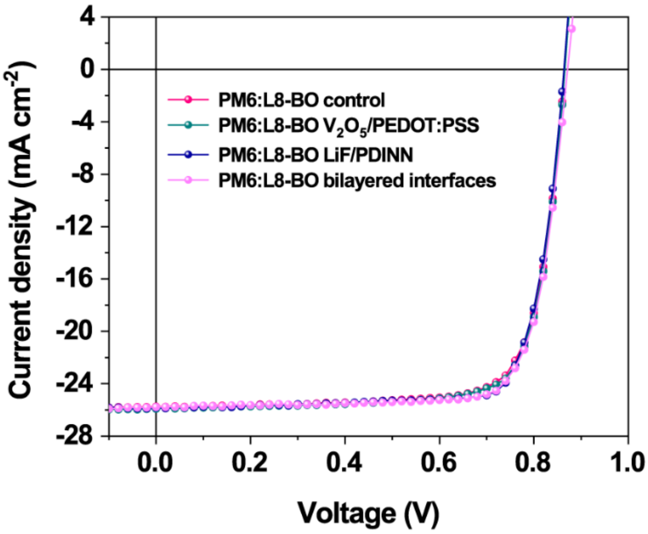

Fig. S6 *J*-*V* characteristics of binary PM6:L8-BO OSCs with different device structures.

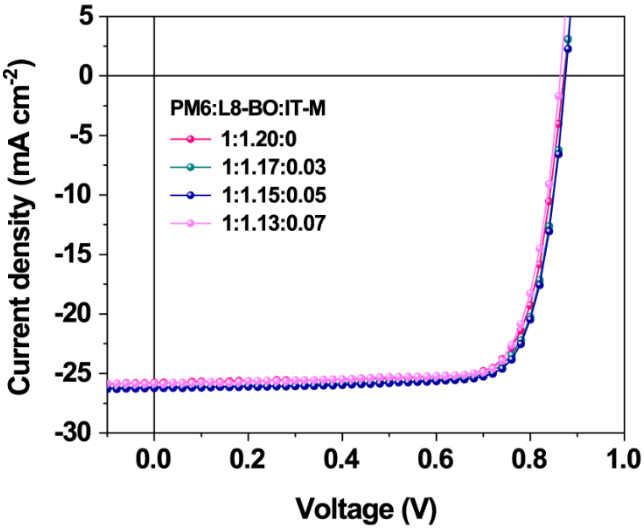

Fig. S7 *J*-*V* characteristics of PM6:L8-BO-based ternary OSCs with various IT-M content.

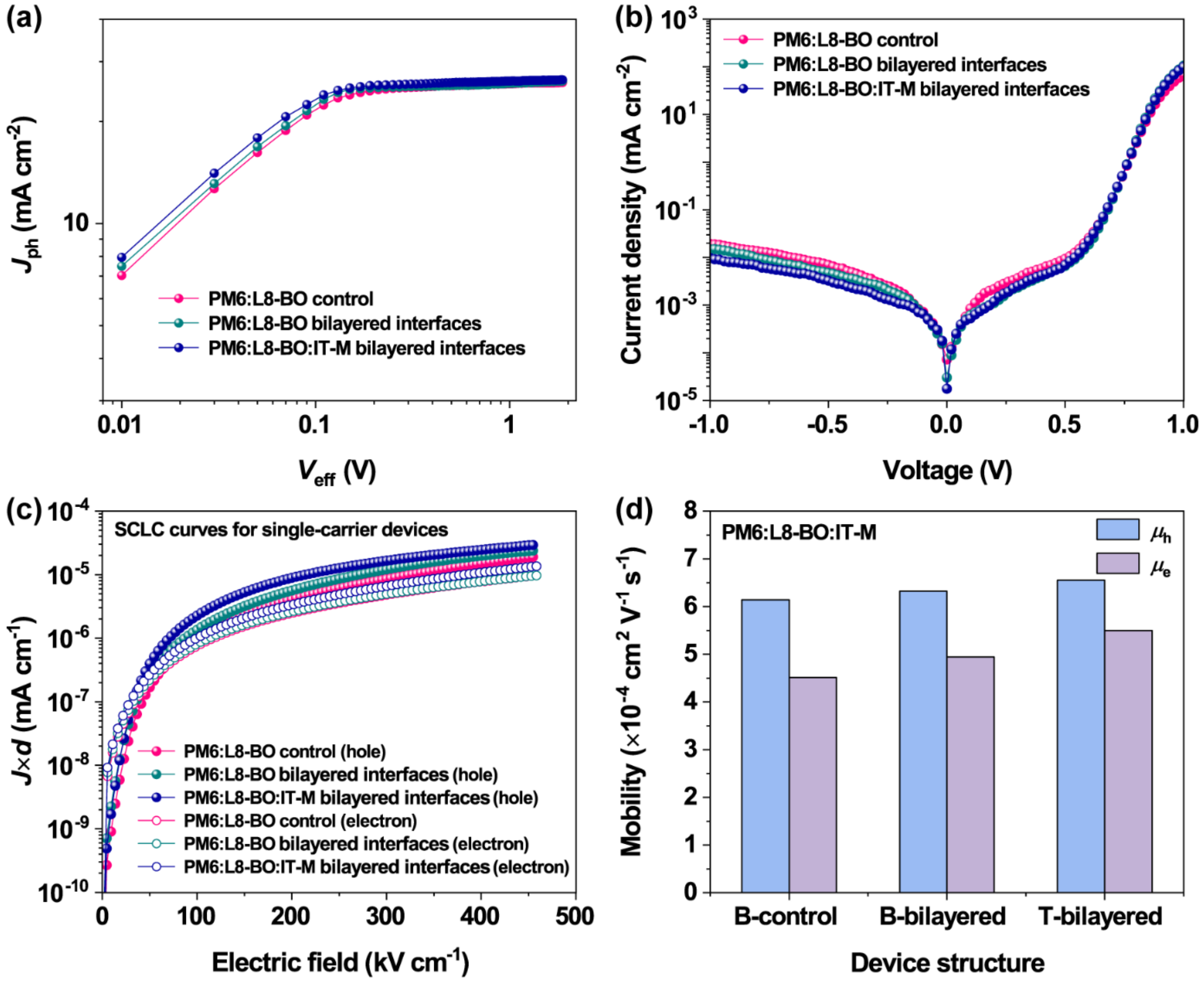

Fig. S8 (a) J_{ph}-V_{eff} curves, (b) dark J-V characteristics, (c) SCLC curves and (d) charge carrier mobility of PM6:L8-BO-based binary and ternary OSCs with different device structures.

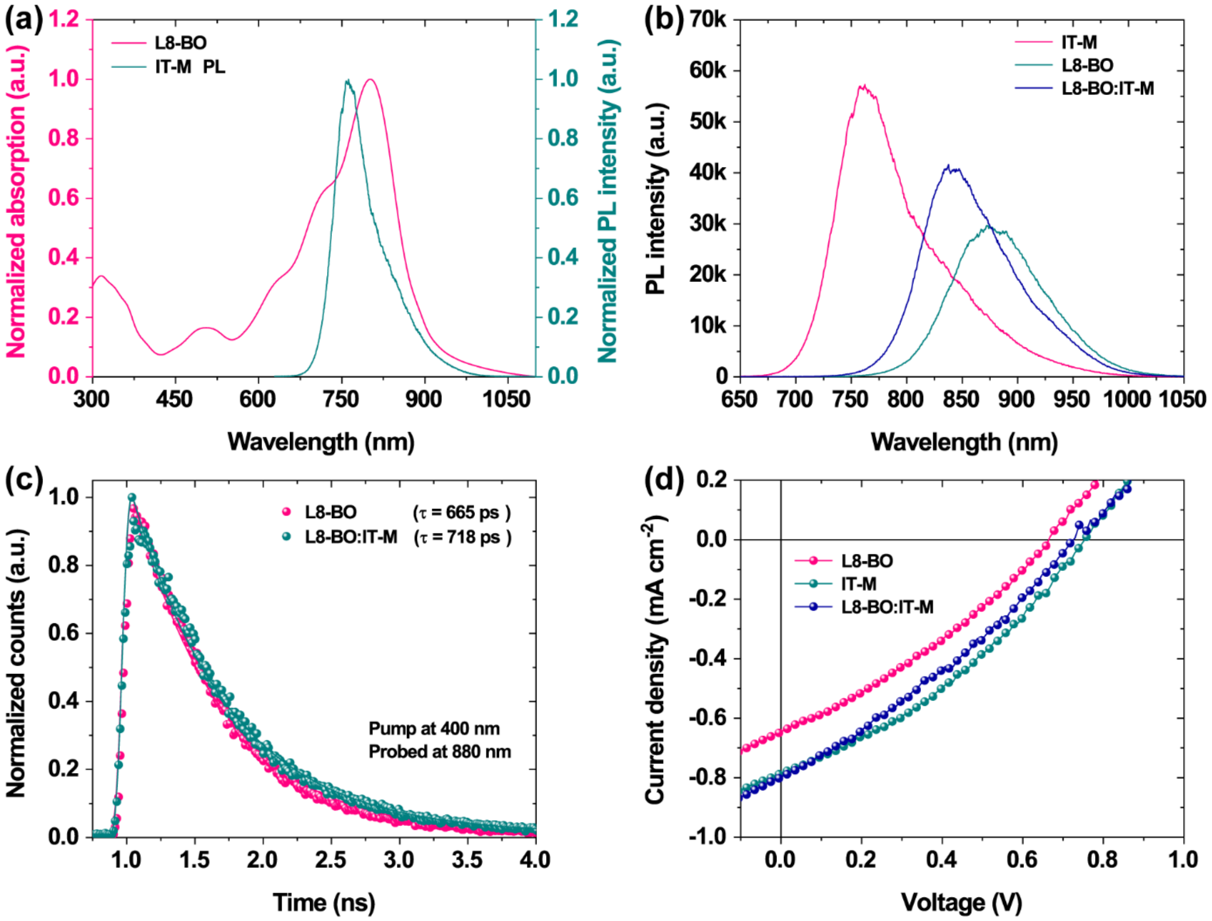

Fig. S9 (a) Normalized absorption spectra of neat L8-BO film and PL spectra of pristine IT-M film. (b) PL spectra of neat IT-M, L8-BO and L8-BO:IT-M (1:1) blend films. (c) Normalized TRPL spectra of neat L8-BO and L8-BO:IT-M (1:1) blend films. (d) The *J*-*V* curves of OPV devices based on neat IT-M, L8-BO and L8-BO:IT-M (1:1) blend films.

The photophysical and device characterizations were conducted to investigate the underlying charge and/or energy transfer dynamics between L8-BO and IT-M. The obvious spectral overlap between the absorption of L8-BO and the PL of IT-M indicate the existence of Förster resonance energy transfer (FRET) in theory (**Fig. S9a**). The increased emission intensity and fluorescence lifetime of L8-BO:IT-M (1:1) blend compared to those of neat L8-BO film further confirm efficient FRET process from IT-M to L8-BO (**Fig. S9b** and **S9c**), where IT-M and L8-BO are the energy donor and energy acceptor, respectively. Furthermore, the L8-BO:IT-M (1:1) blend-based devices show a higher J_{SC} value relative to that of IT-M and L8-BO OSCs (**Fig. S9d**), manifesting charge transfer also occurs between IT-M and L8-BO. Hence, charge transfer and energy transfer processes are interwined in L8-BO:IT-M blend.

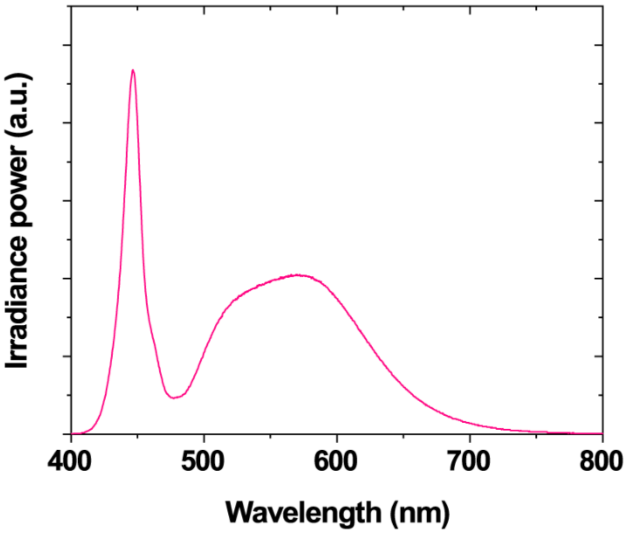

Fig. S10 Light spectrum of the white LED used for photostability test in this work.

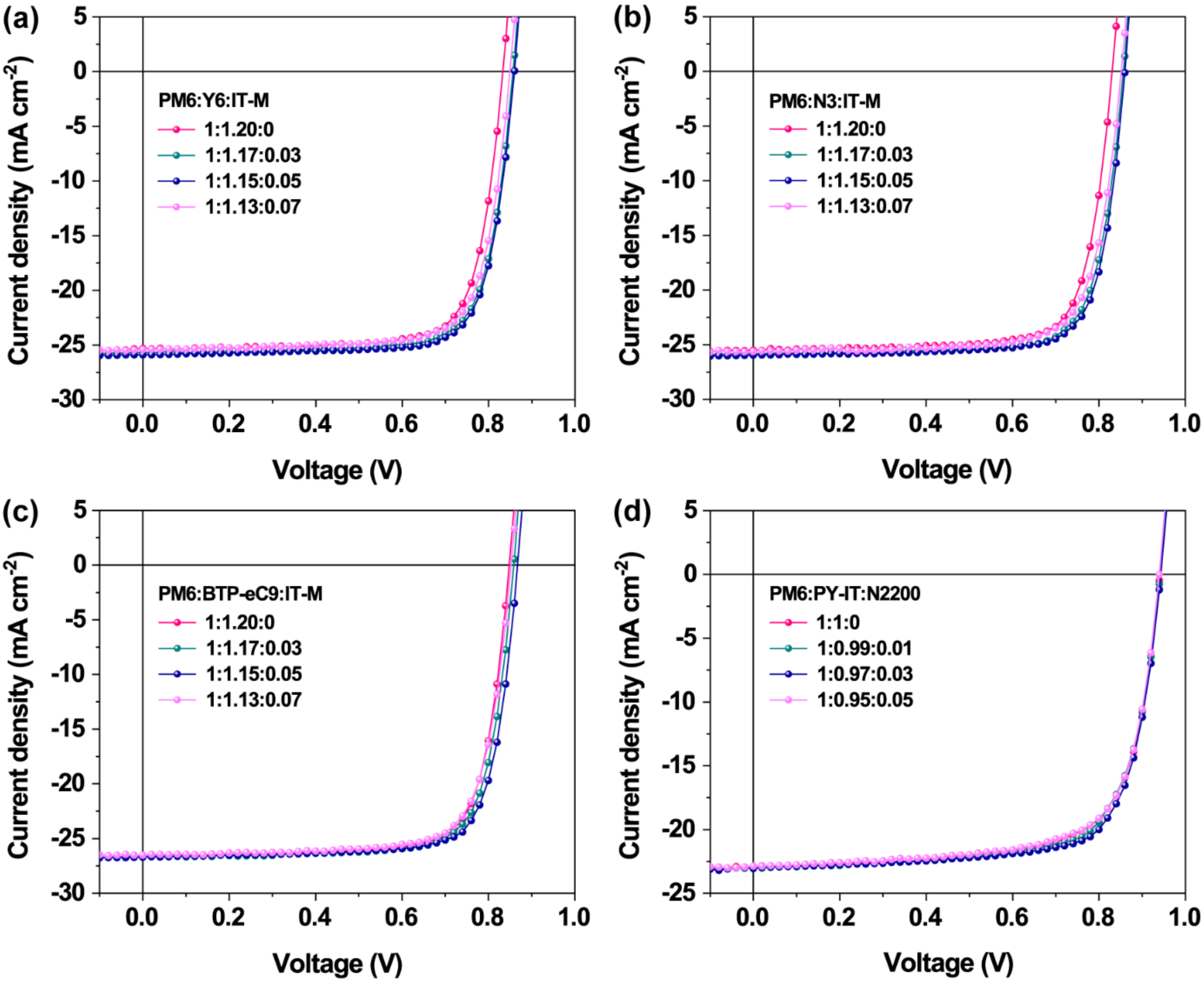

Fig. S11 *J*-*V* characteristics of (a) PM6:Y6, (b) PM6:N3 and (c) PM6:BTP-eC9-based ternary OSCs with various IT-M content as well as (d) PM6:PY-IT-based ternary OSCs with various N2200 content.

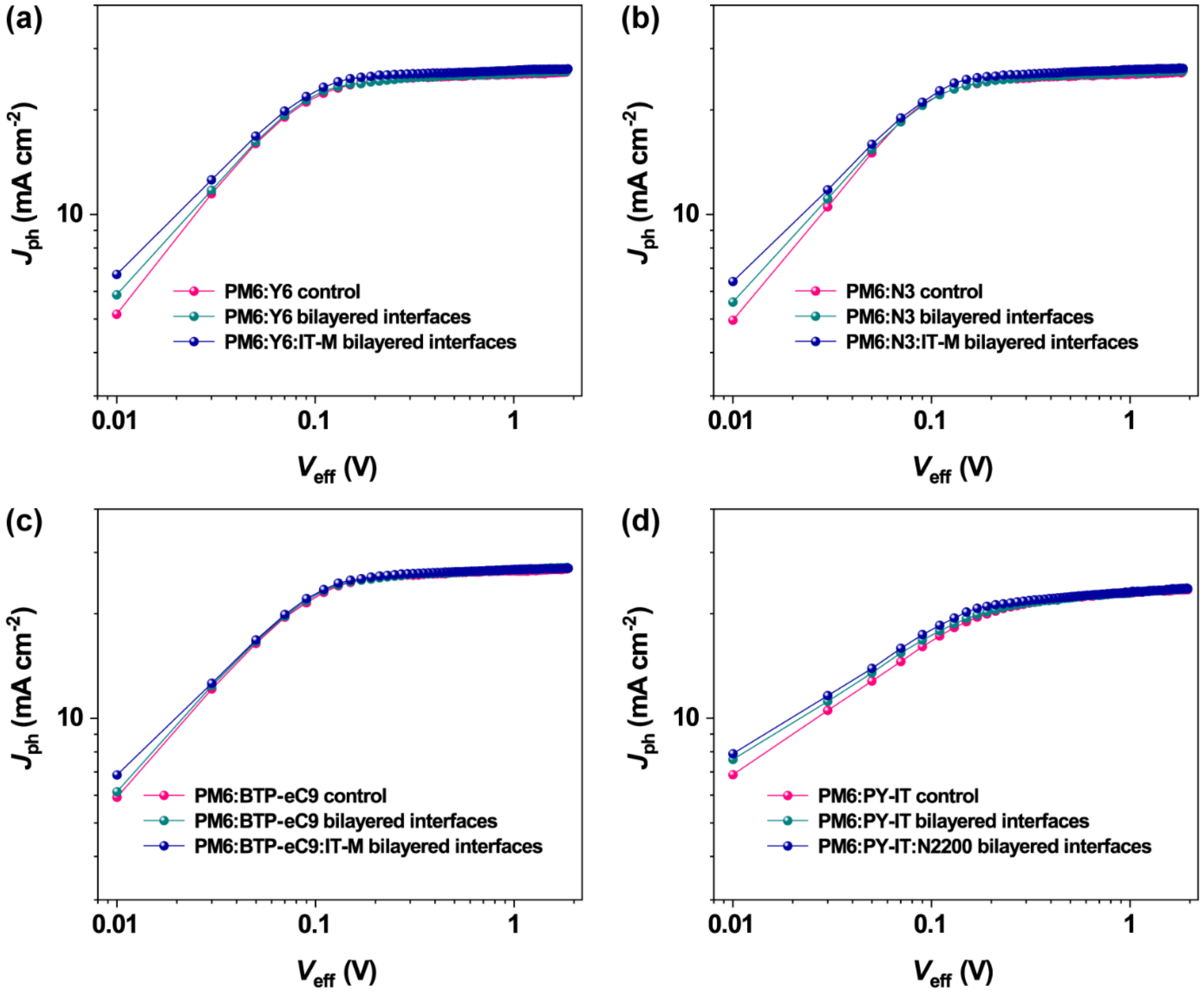

Fig. S12 J_{ph}-V_{eff} curves of (a) PM6:Y6, (b) PM6:N3, (c) PM6:BTP-eC9 and (d) PM6:PY-IT-based binary and ternary OSCs with different device structures.

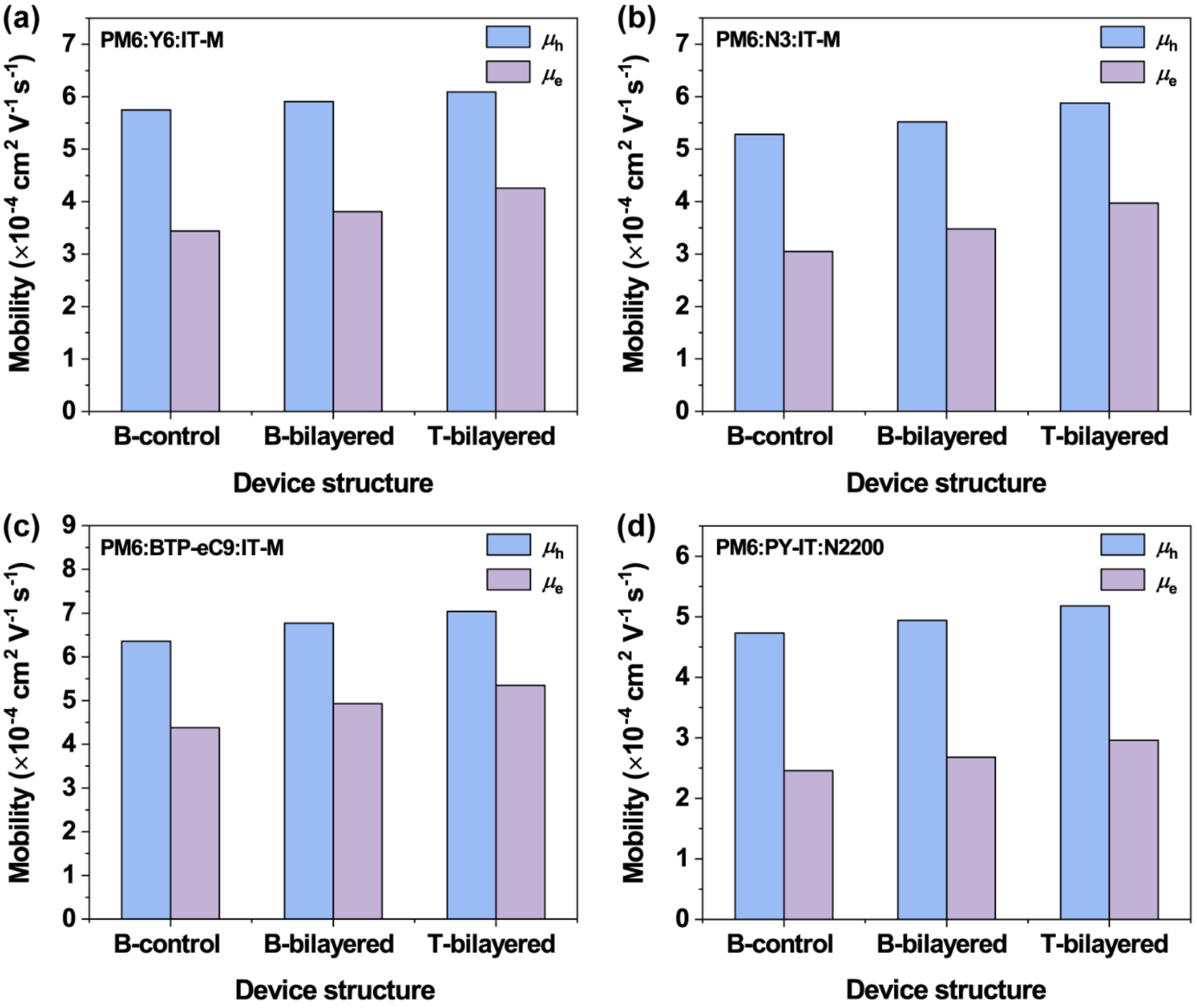

Fig. S13 Charge carrier mobilities of (a) PM6:Y6, (b) PM6:N3, (c) PM6:BTP-eC9 and (d) PM6:PY-IT-based binary and ternary OSCs with different device structures.

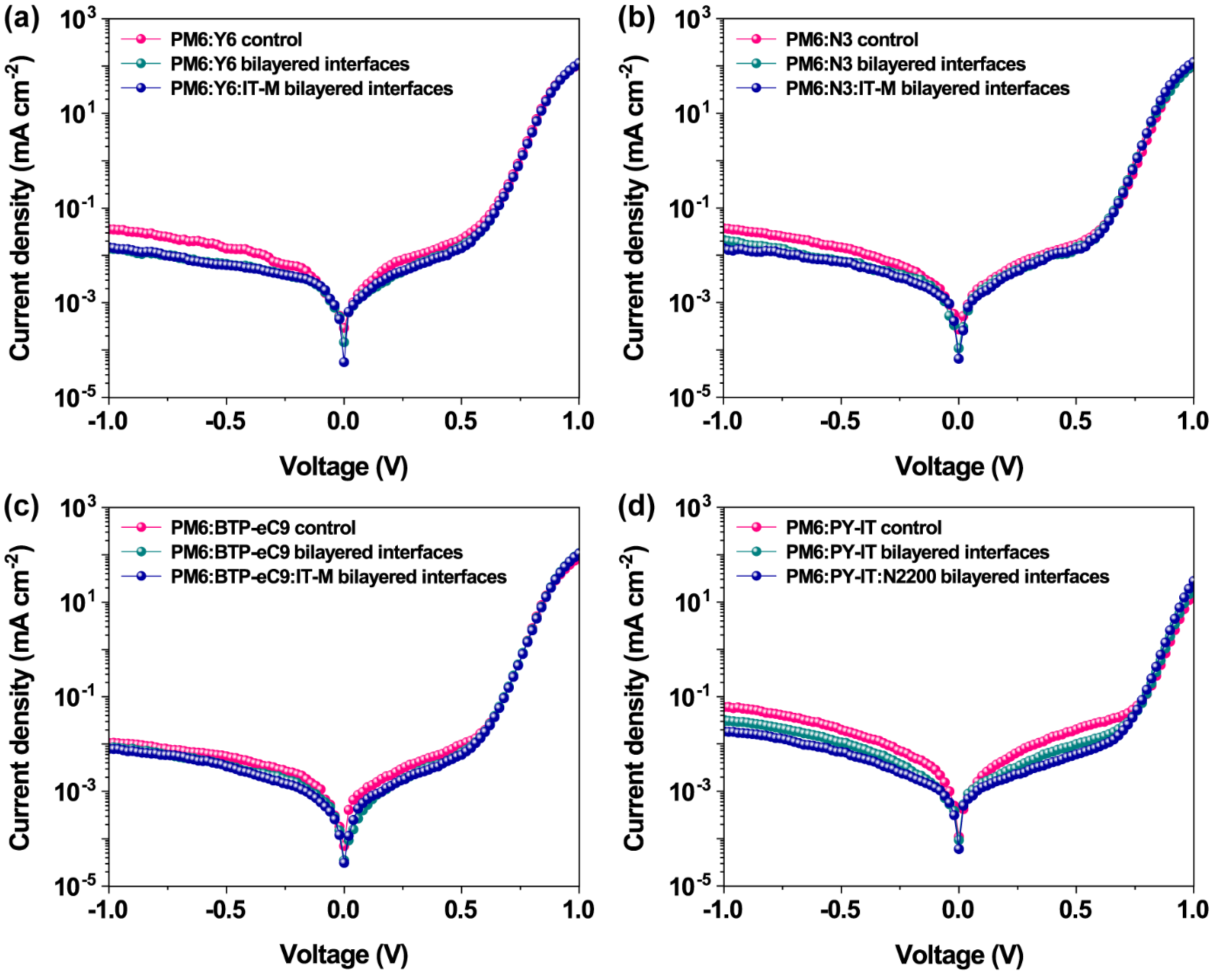

Fig. S14 Dark *J*-*V* characteristics of (a) PM6:Y6, (b) PM6:N3, (c) PM6:BTP-eC9 and (d) PM6:PY-IT-based binary and ternary OSCs with different device structures.

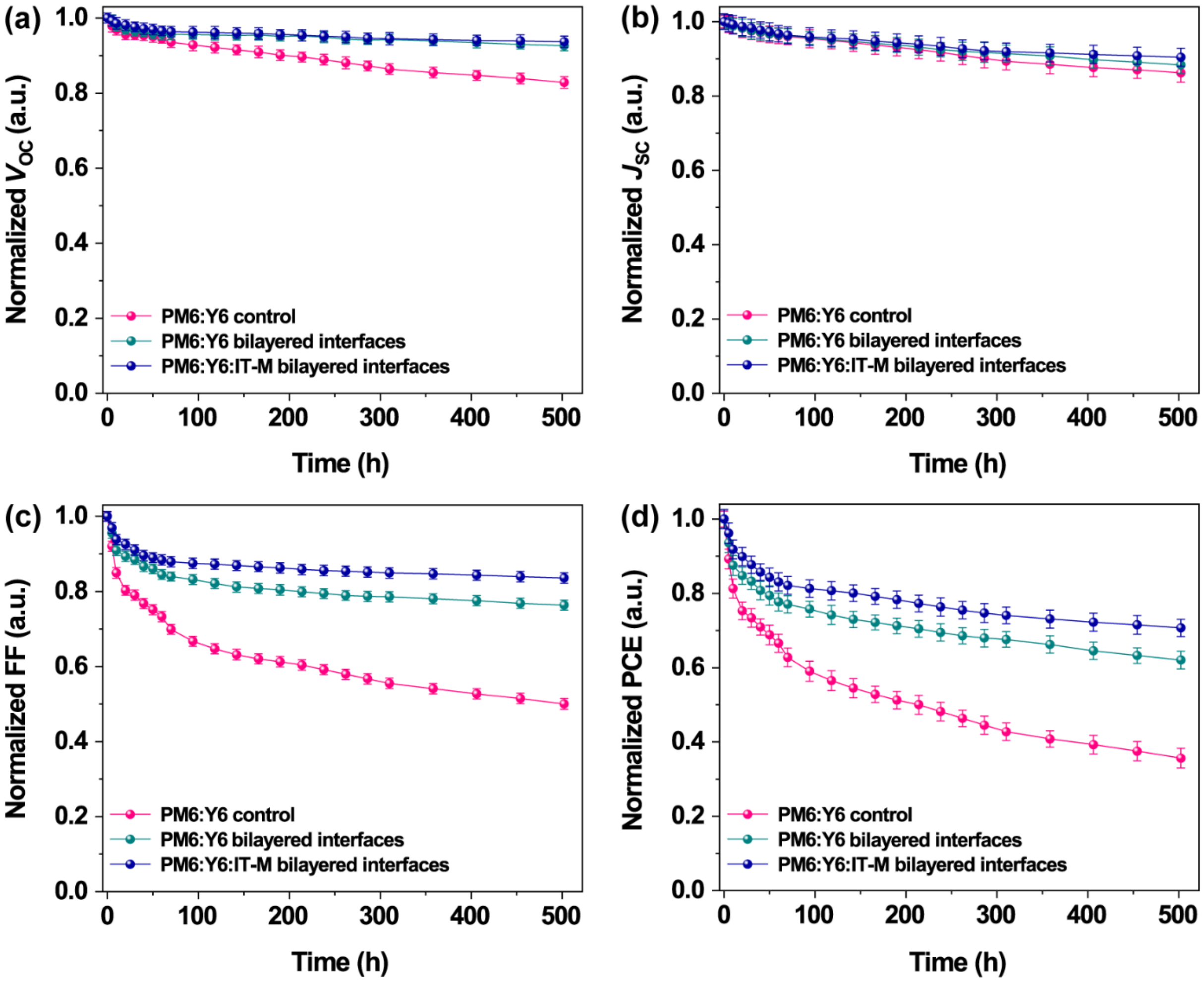

Fig. S15 Normalized (a) V_{OC}, (b) J_{SC}, (c) FF and (d) PCE decay curves of PM6:Y6-based binary and ternary OSCs with different device structures under continuous illumination of a 100 mW cm^{-2} white LED.

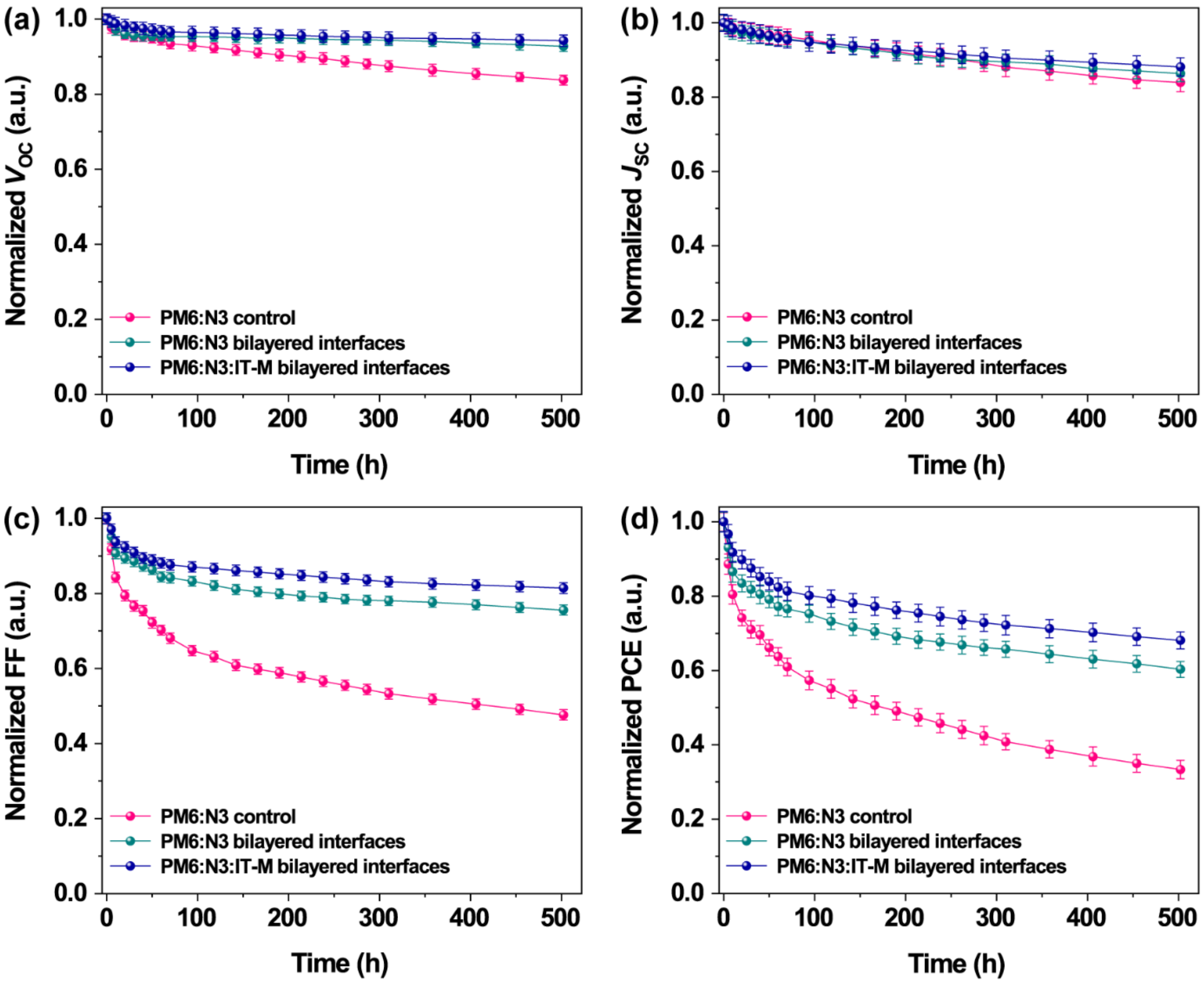

Fig. S16 Normalized (a) V_{OC}, (b) J_{SC}, (c) FF and (d) PCE decay curves of PM6:N3-based binary and ternary OSCs with different device structures under continuous illumination of a 100 mW cm^{-2} white LED.

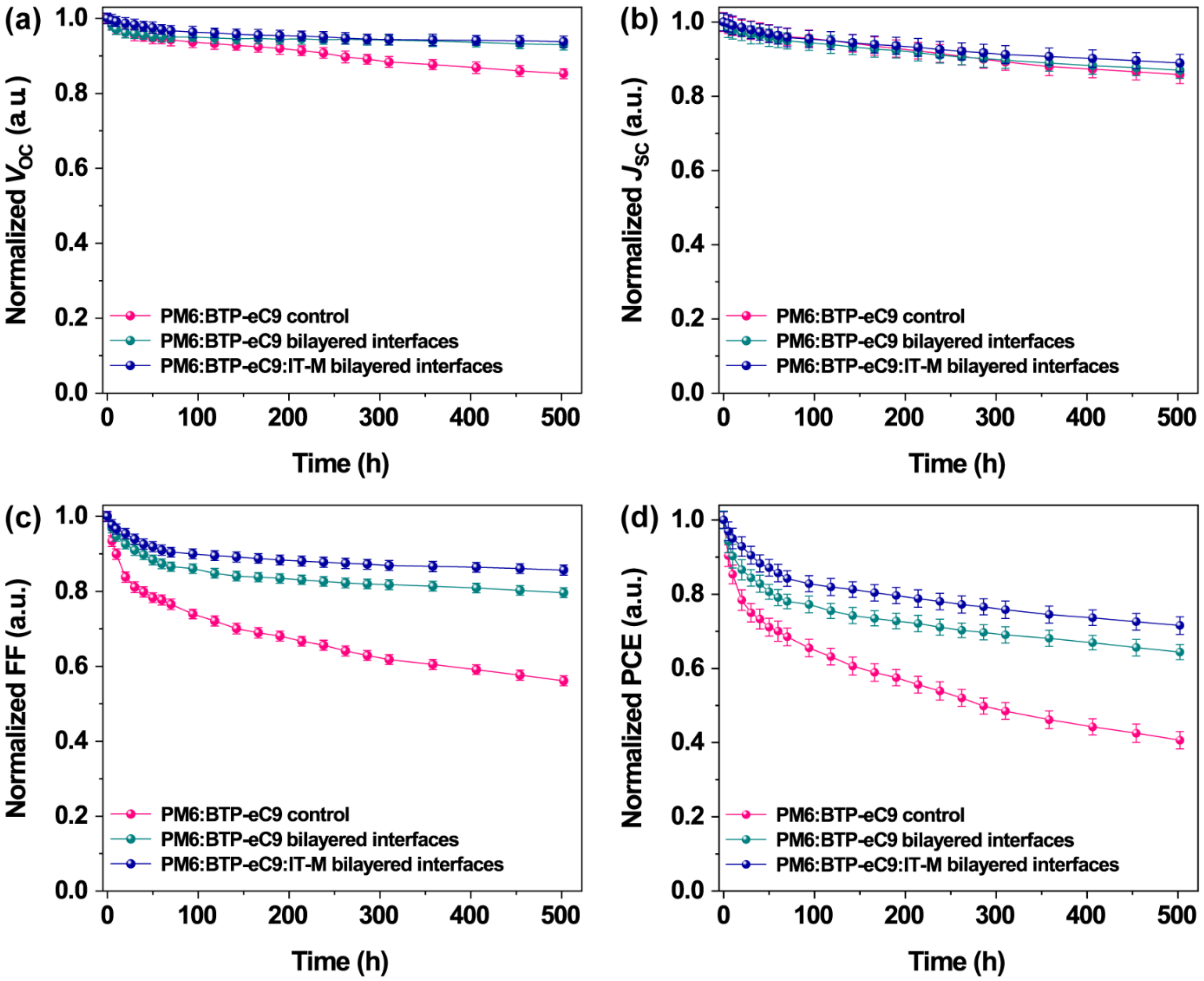

Fig. S17 Normalized (a) V_{OC}, (b) J_{SC}, (c) FF and (d) PCE decay curves of PM6:BTP-eC9-based binary and ternary OSCs with different device structures under continuous illumination of a 100 mW cm^{-2} white LED.

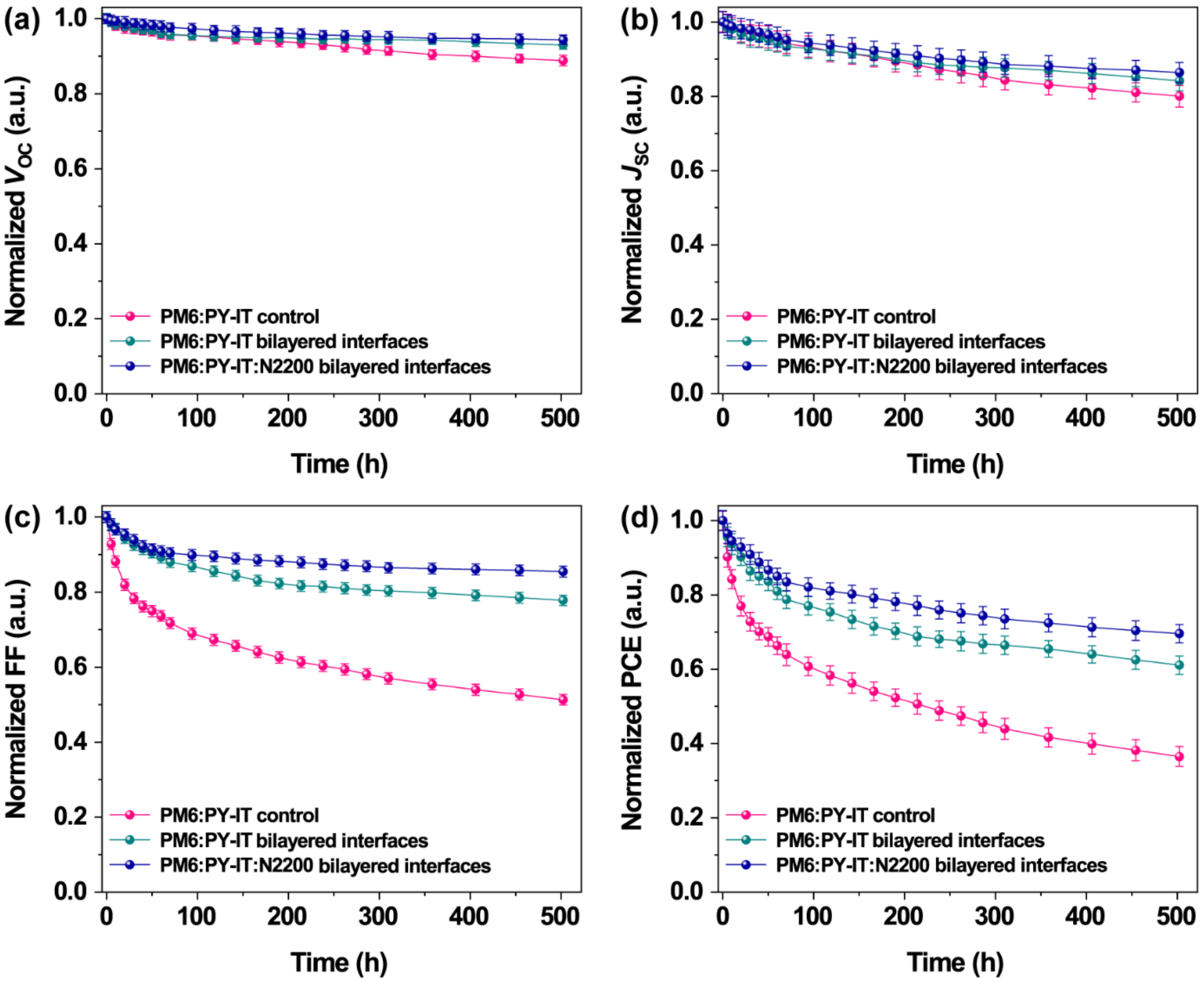

Fig. S18 Normalized (a) V_{OC}, (b) J_{SC}, (c) FF and (d) PCE decay curves of PM6:PY-IT-based binary and ternary OSCs with different device structures under continuous illumination of a 100 mW cm^{-2} white LED.

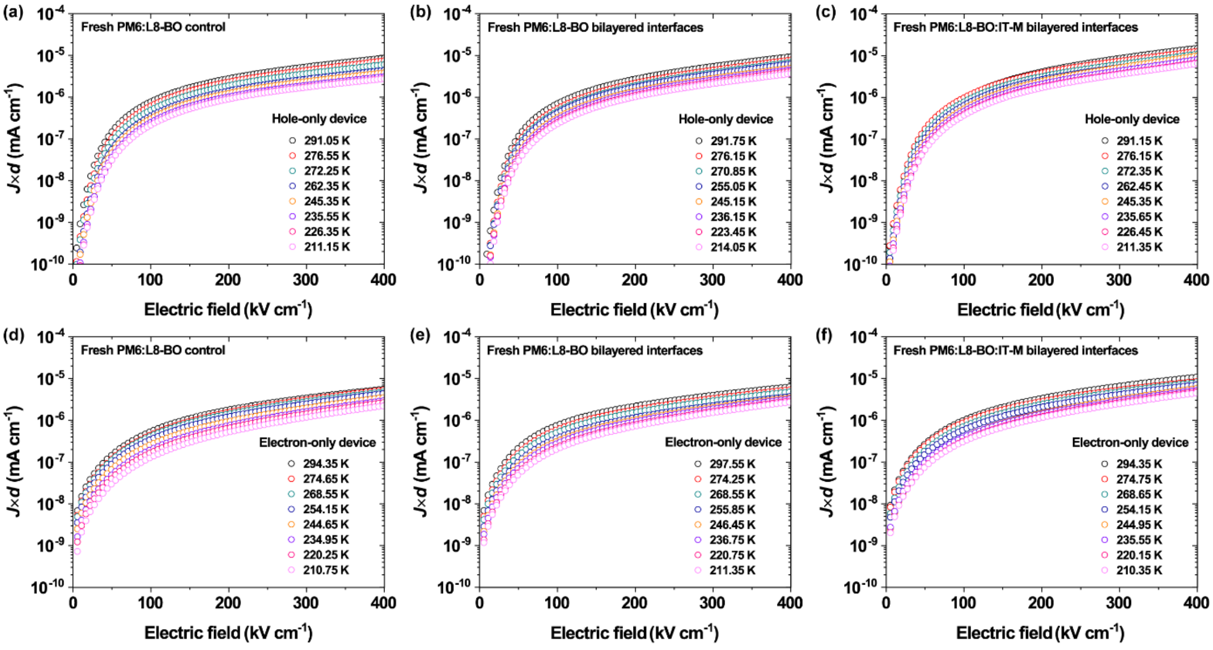

Fig. S19 *J*×*d* as a function of the applied electric field for GDM analysis.

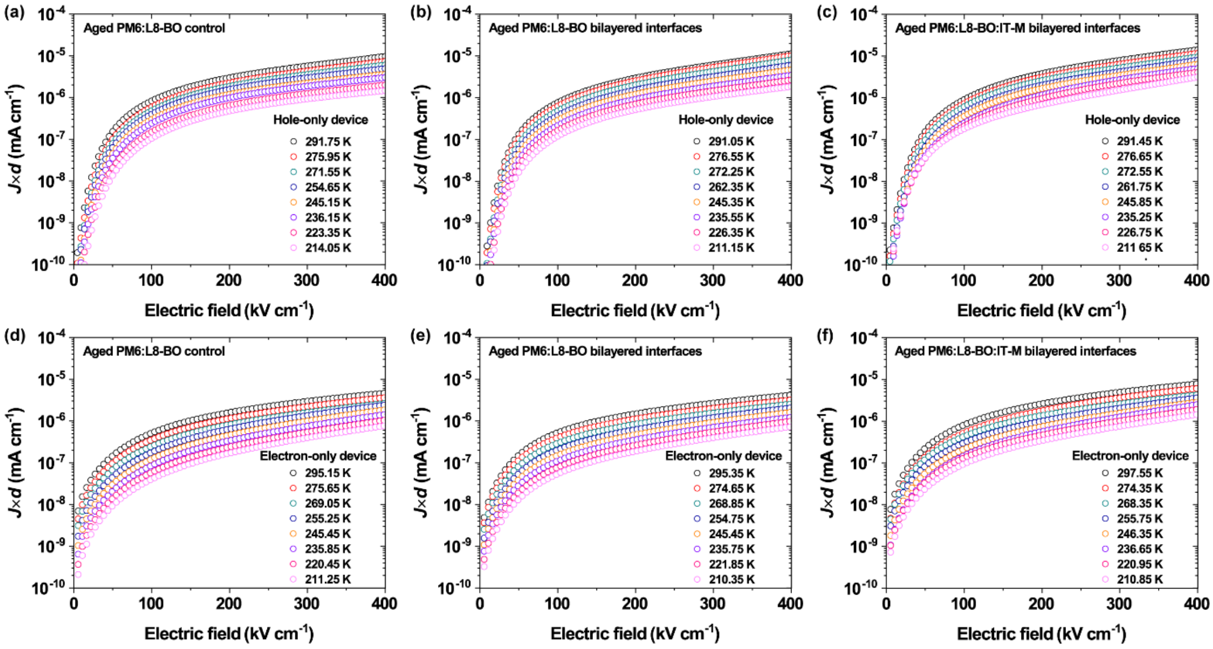

Fig. S20 *J*×*d* as a function of the applied electric field for GDM analysis.

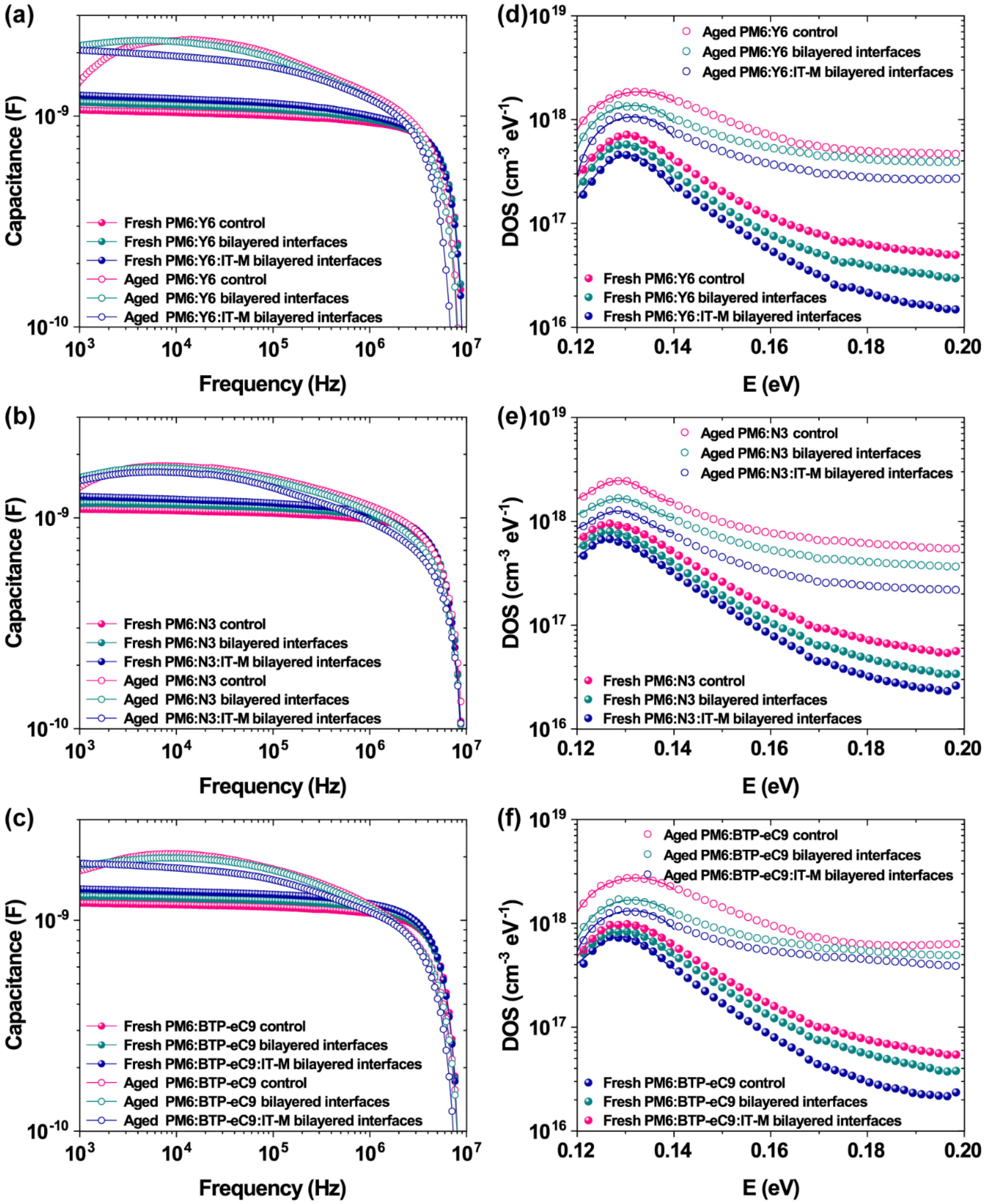

Fig. S21 (a-c) The frequency-dependent capacitance spectra and (d-f) trap DOS as well as corresponding Gaussian fitting results for PM6:Y6, PM6:N3 and PM6:BTP-eC9-based binary and ternary OSCs with different device structures before and after continuous LED illumination, respectively.

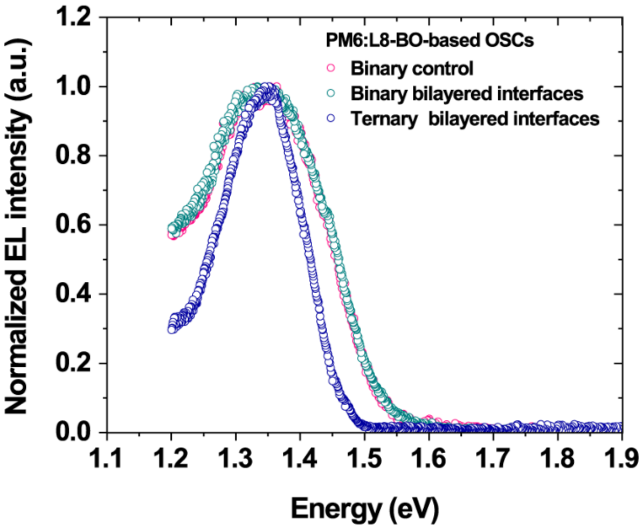

Fig. S22 Normalized EL spectra of PM6:L8-BO-based binary and ternary OSCs with different device structures.

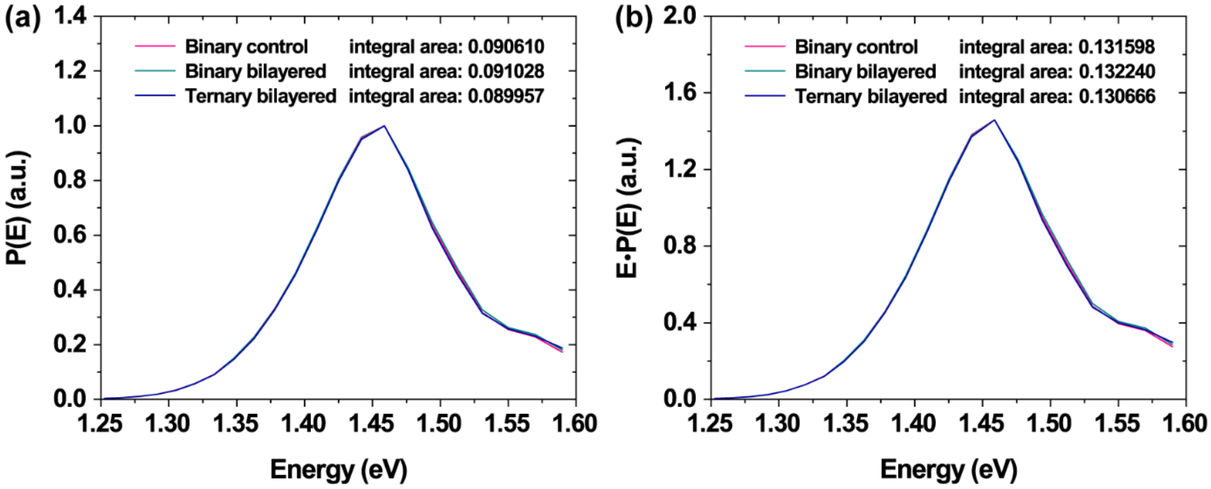

Fig. S23 Bandgap distribution of PM6:L8-BO-based binary and ternary OSCs with different device structures.

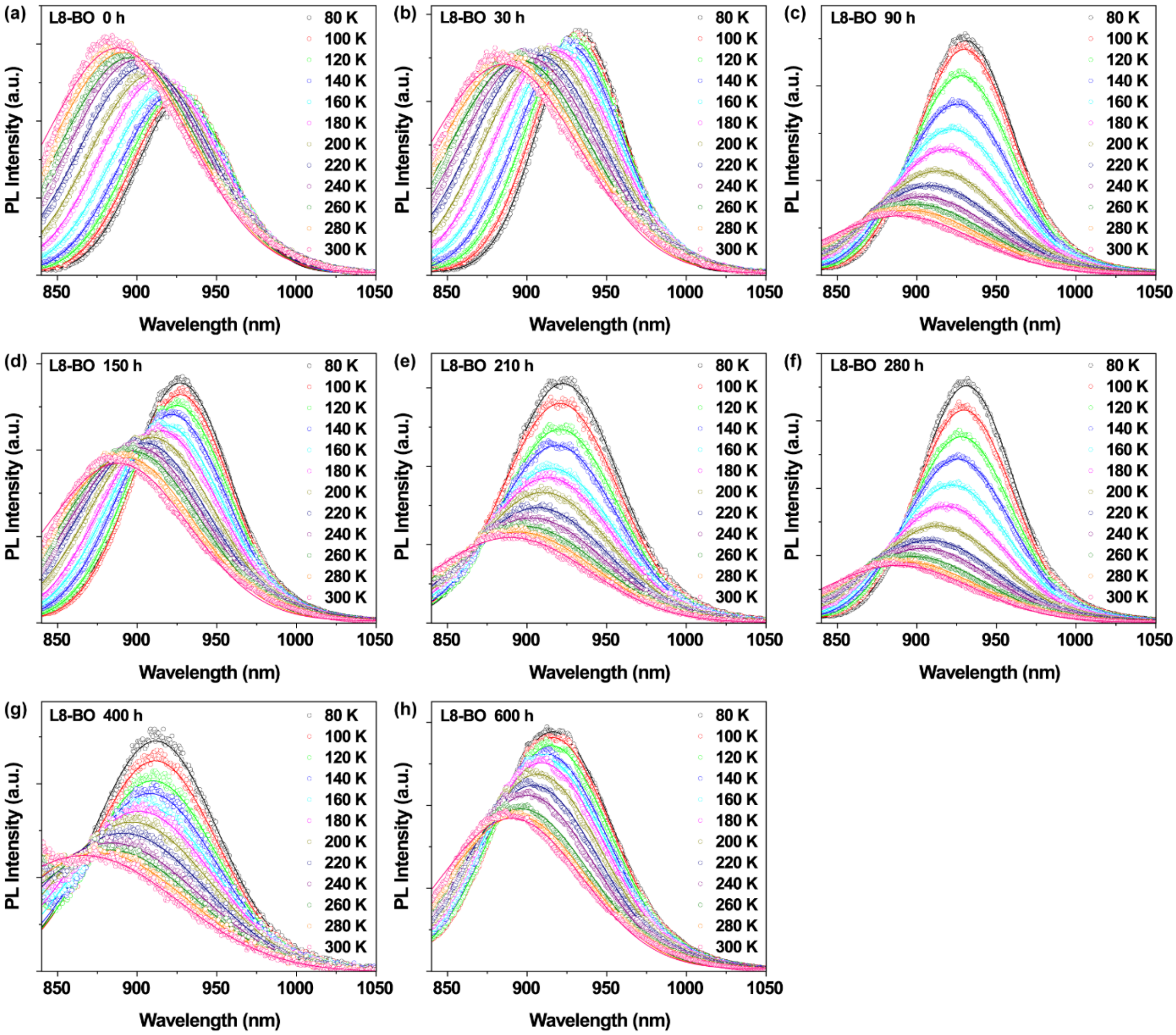

Fig. S24 (a-h) Temperature-dependent emission spectra of neat L8-BO film as a function of time under continuous illumination of a 100 mW cm^{-2} white LED (Excite @ 800 nm).

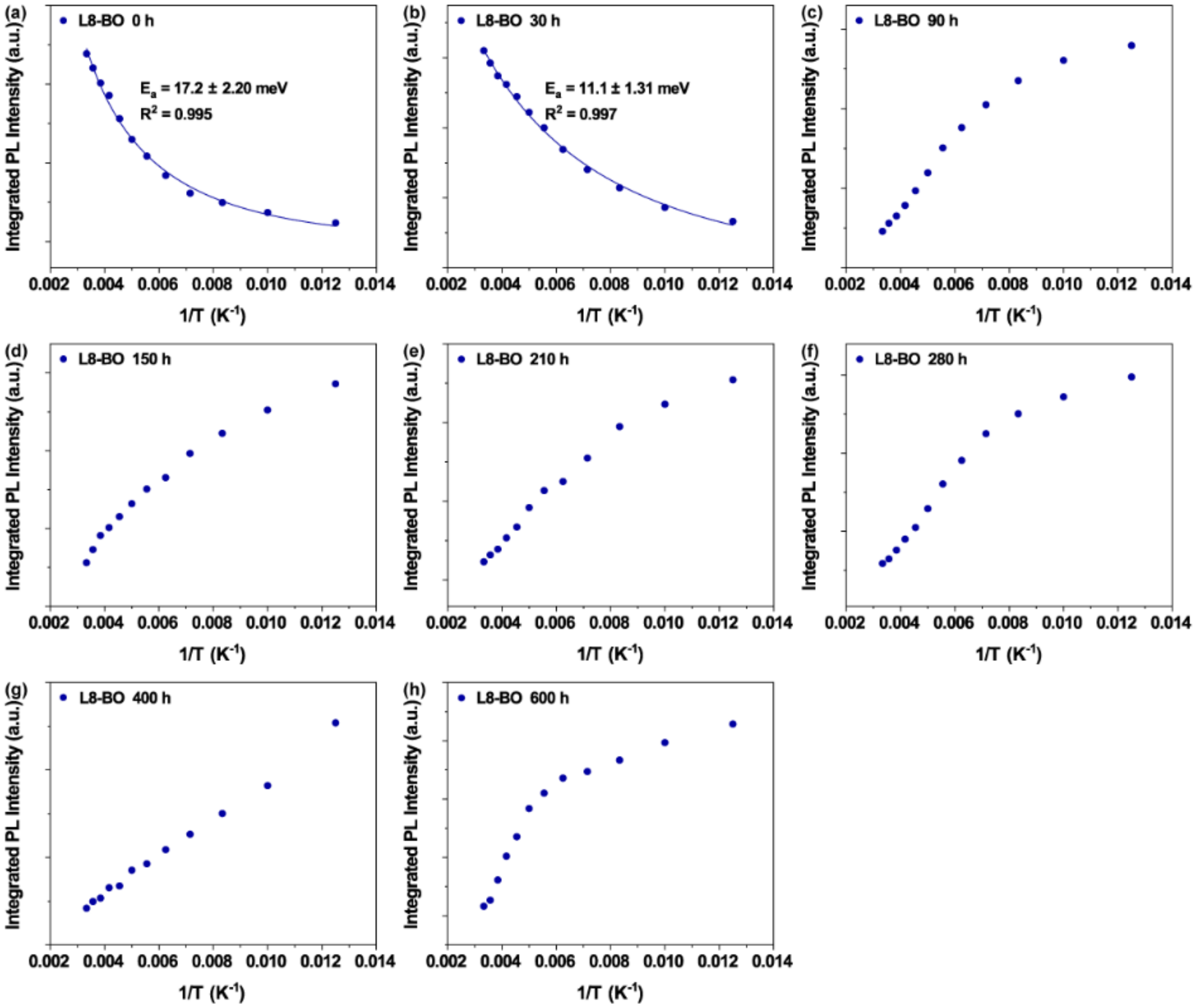

Fig. S25 (a-h) Evolution of emission intensity as a function of temperature from 80 to 300 K for neat L8-BO film under continuous illumination of a 100 mW cm^{-2} white LED.

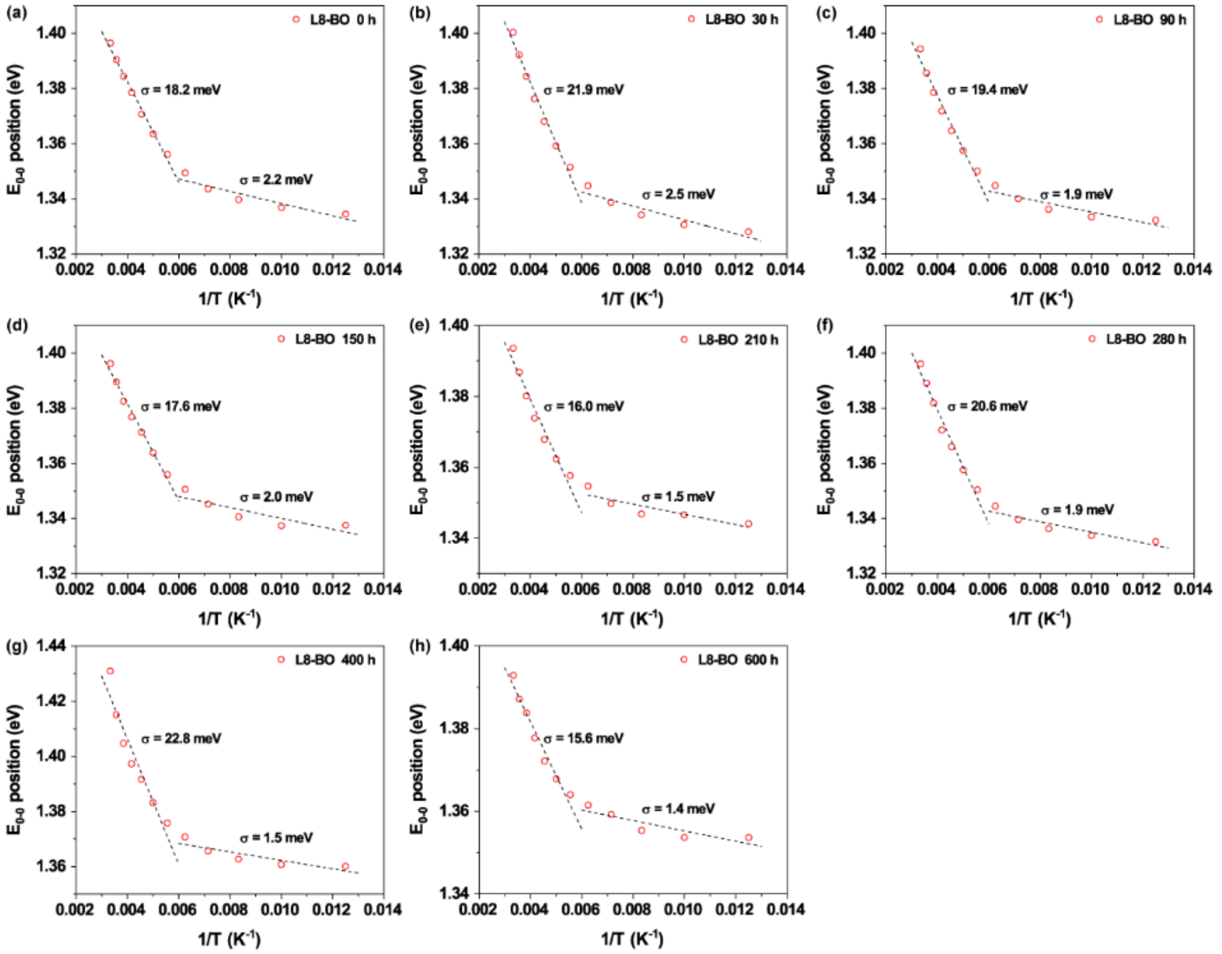

Fig. S26 (a-h) Evolution of 0-0 emission peak energy as a function of temperature from 80 to 300 K for neat L8-BO film under continuous illumination of a 100 mW cm^{-2} white LED.

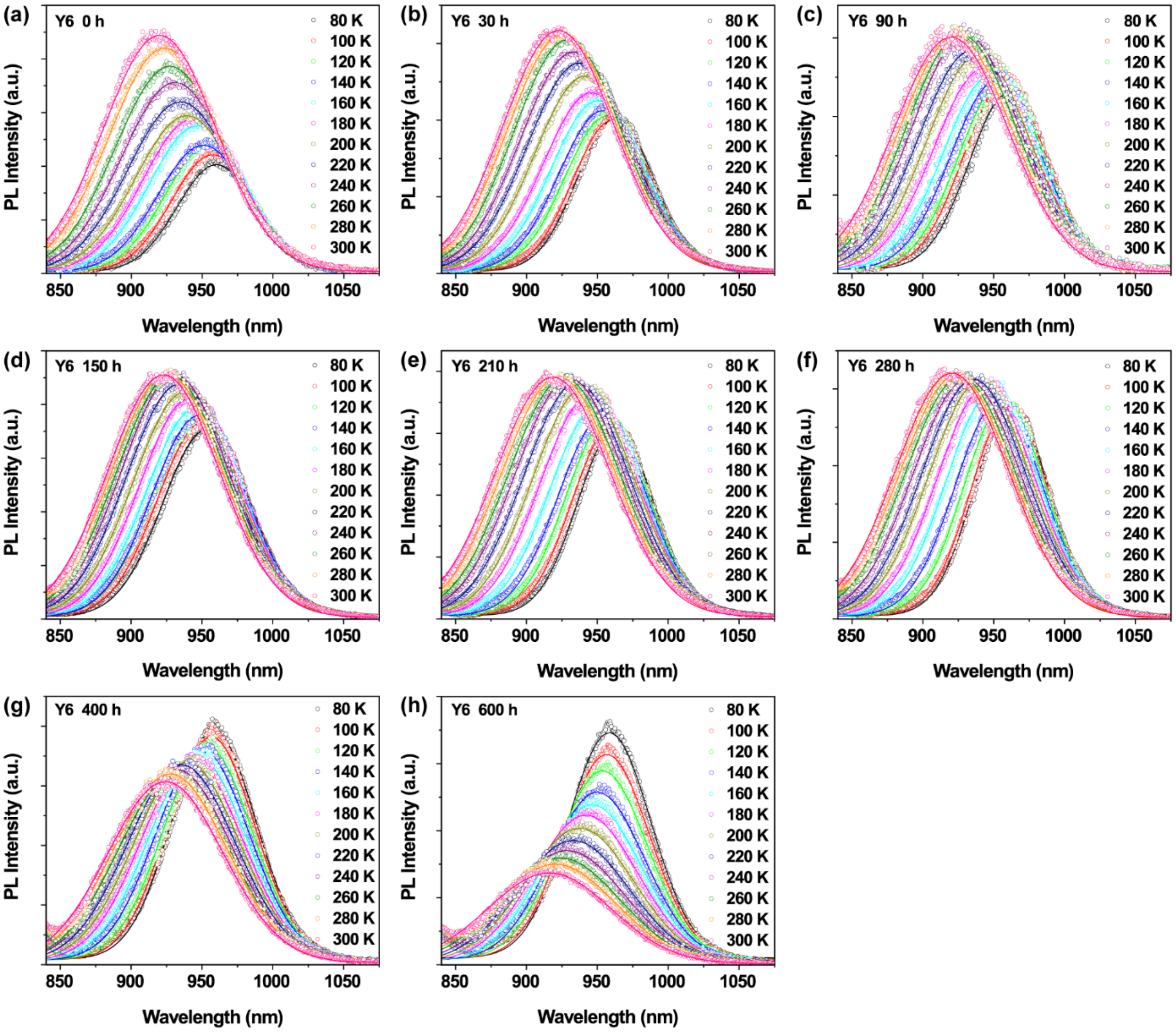

Fig. S27 (a-h) Temperature-dependent emission spectra of neat Y6 film as a function of time under continuous illumination of a 100 mW cm^{-2} white LED (Excite @ 800 nm).

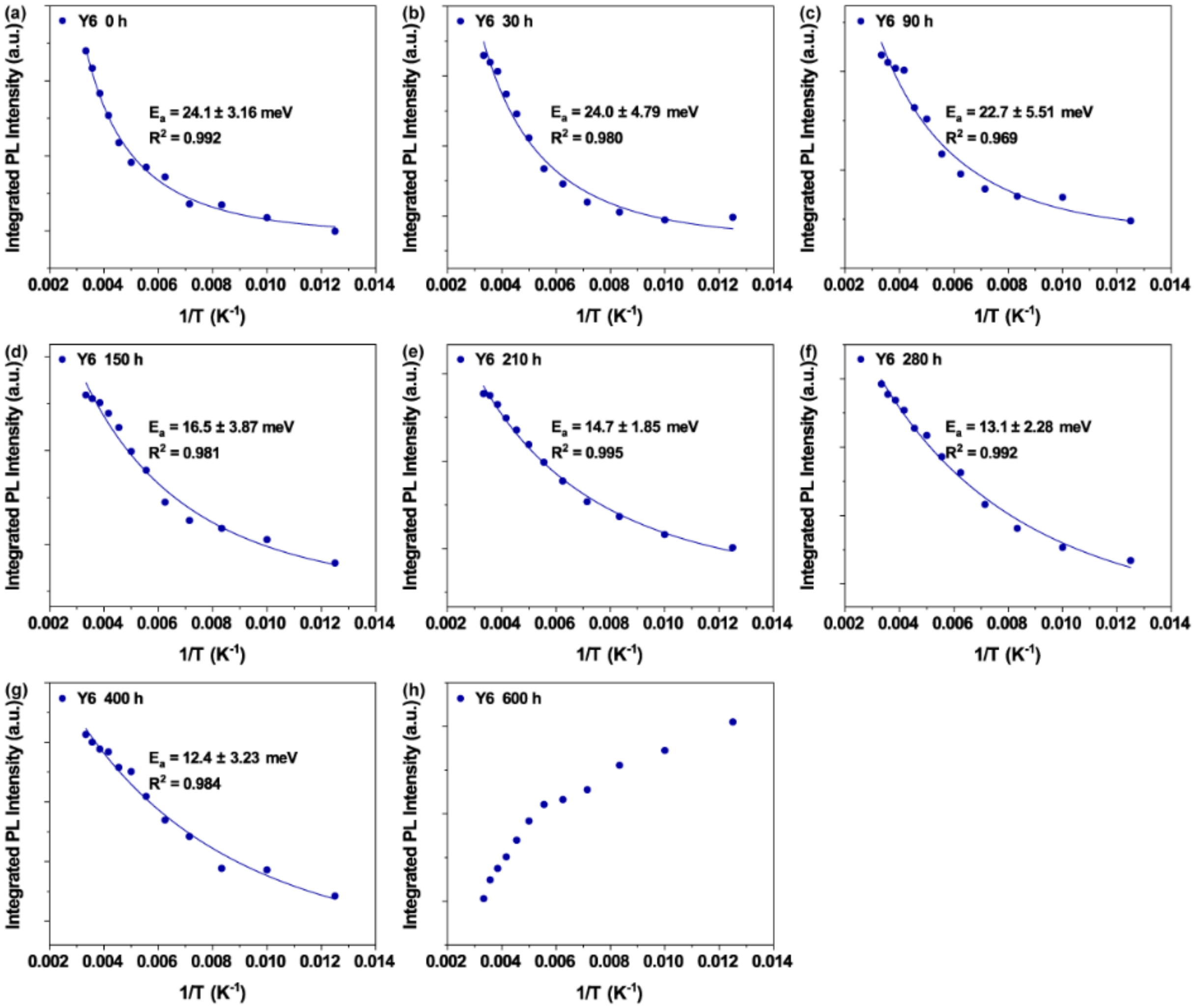

Fig. S28 (a-h) Evolution of emission intensity as a function of temperature from 80 to 300 K for neat Y6 film under continuous illumination of a 100 mW cm^{-2} white LED.

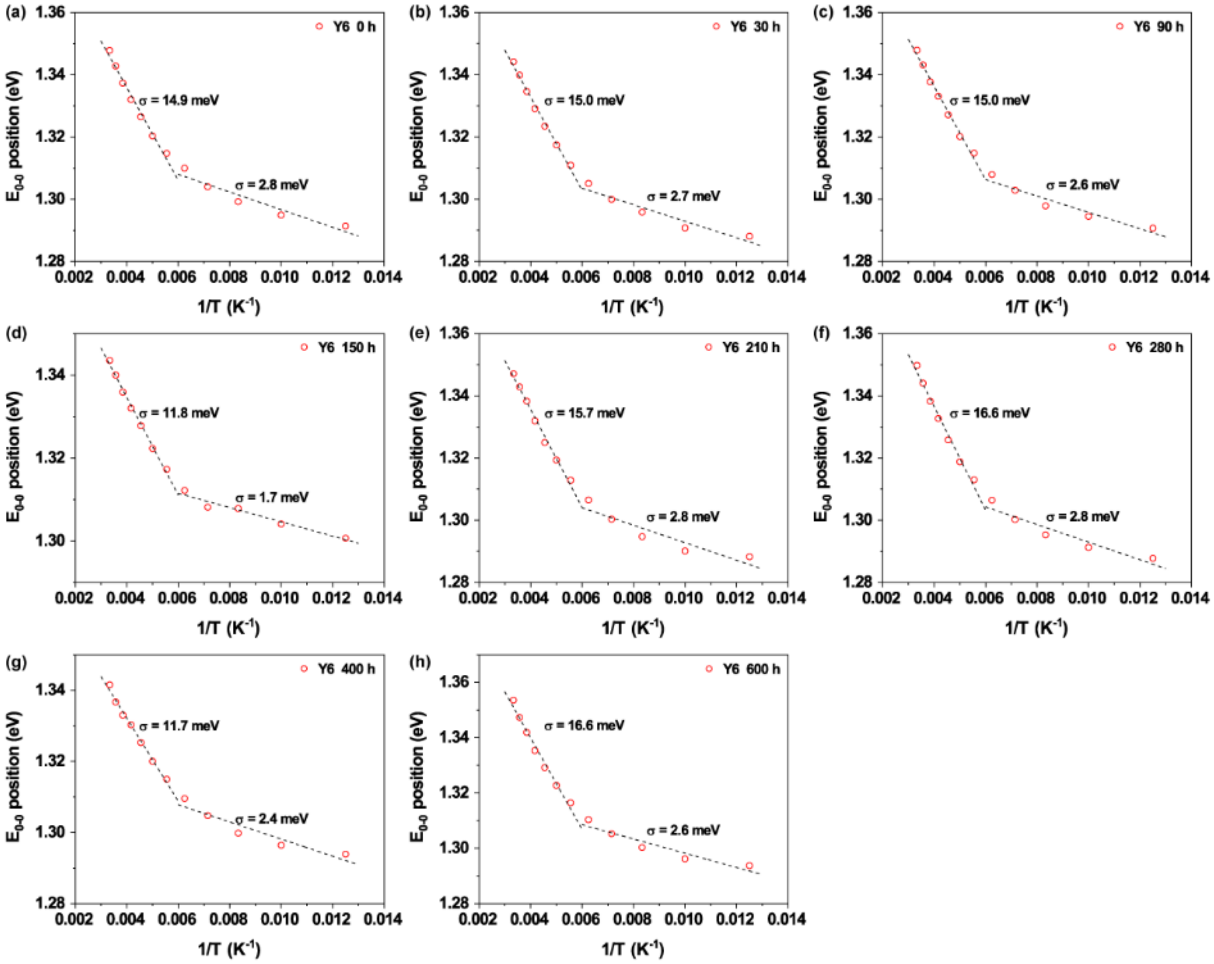

Fig. S29 (a-h) Evolution of 0-0 emission peak energy as a function of temperature from 80 to 300 K for neat Y6 film under continuous illumination of a 100 mW cm^{-2} white LED.

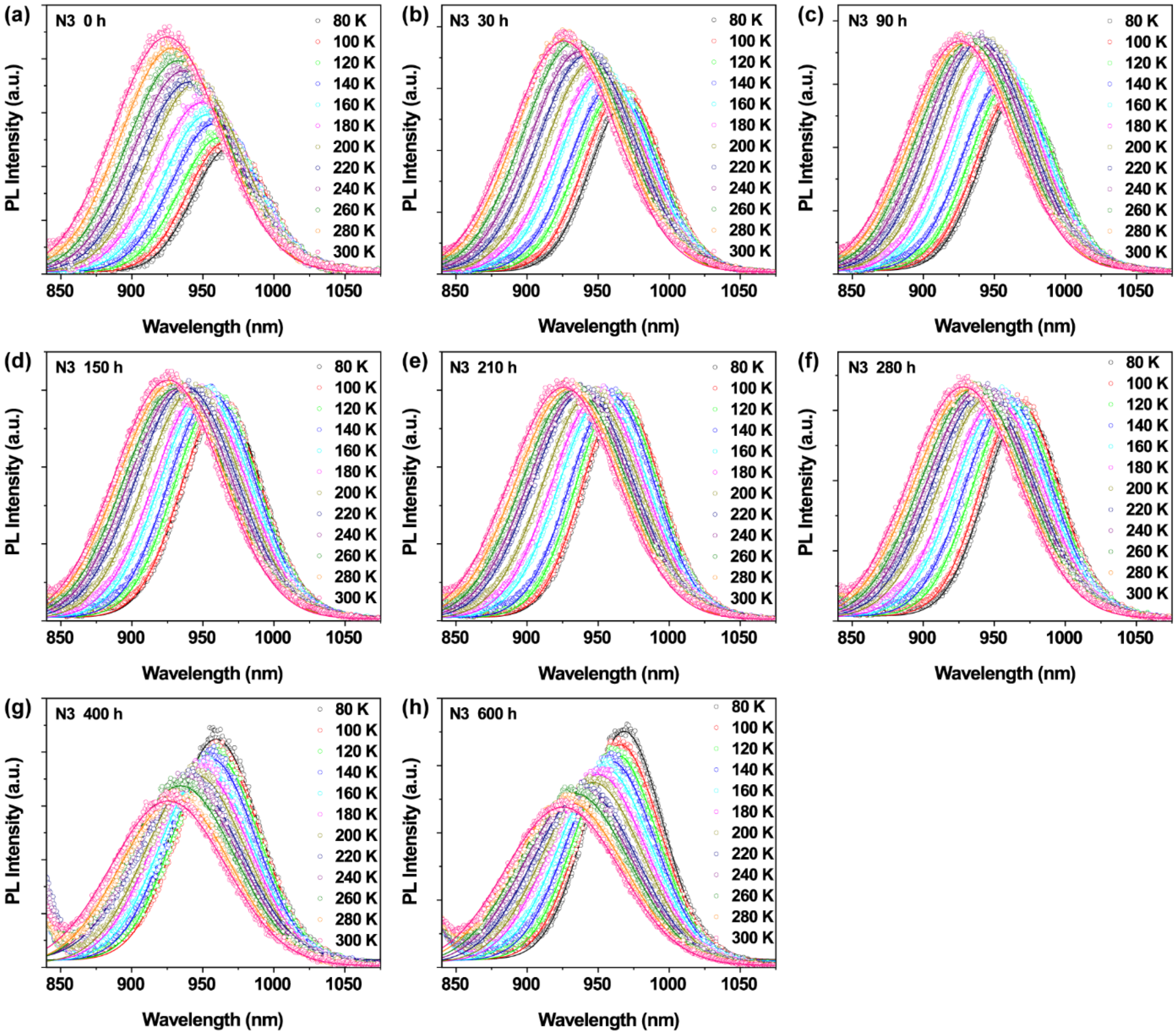

Fig. S30 (a-h) Temperature-dependent emission spectra of neat N3 film as a function of time under continuous illumination of a 100 mW cm^{-2} white LED (Excite @ 800 nm).

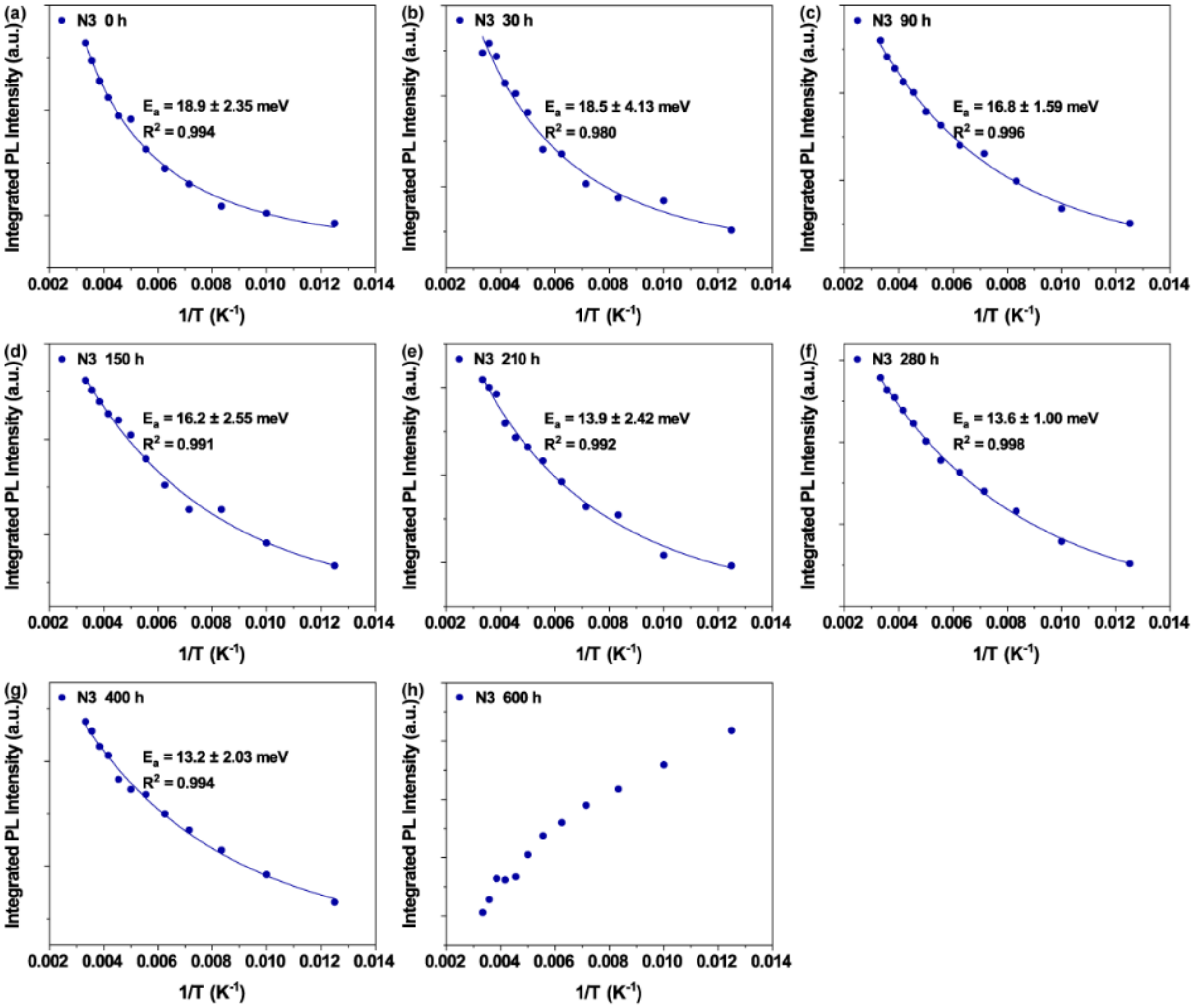

Fig. S31 (a-h) Evolution of emission intensity as a function of temperature from 80 to 300 K for neat N3 film under continuous illumination of a 100 mW cm^{-2} white LED.

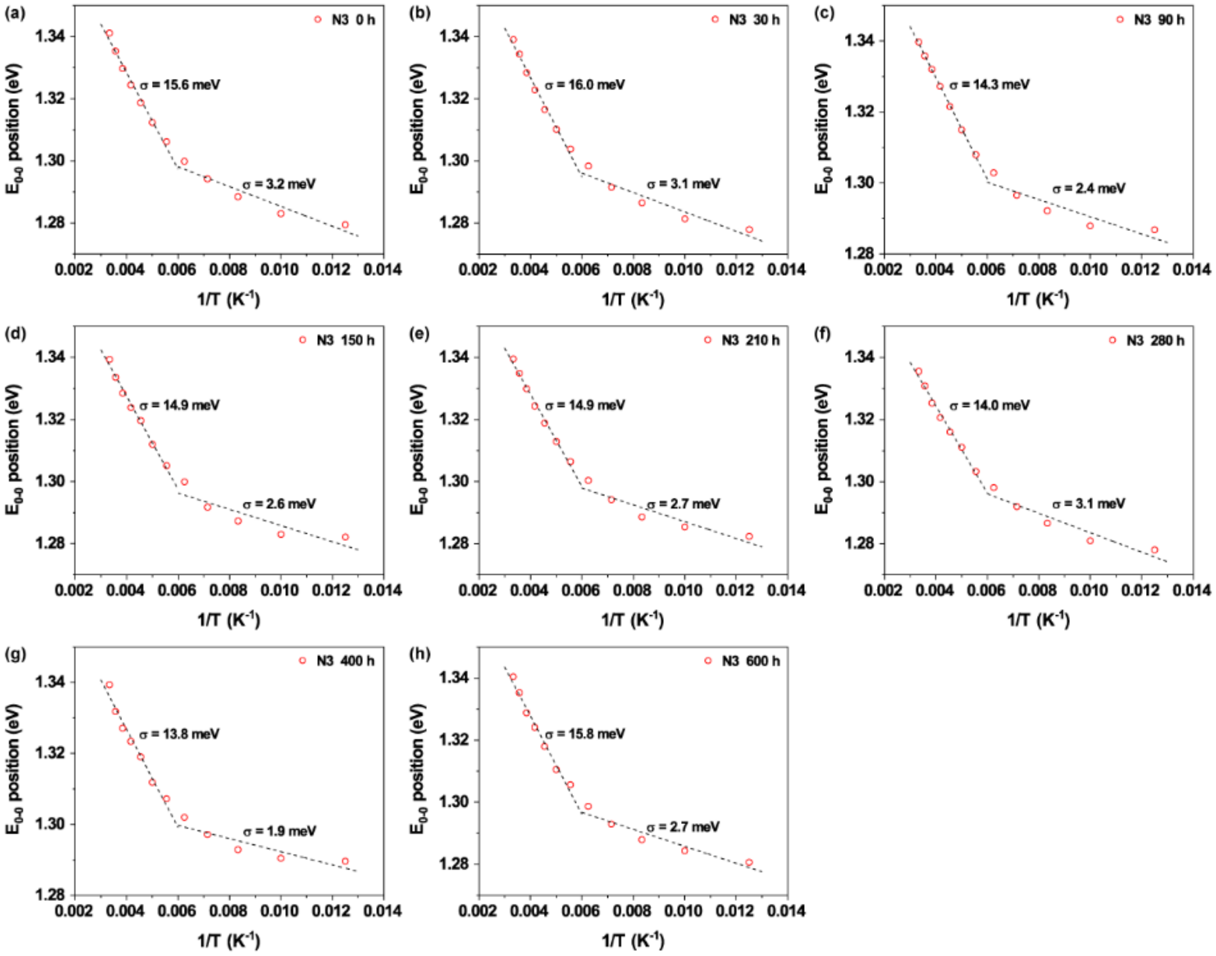

Fig. S32 (a-h) Evolution of 0-0 emission peak energy as a function of temperature from 80 to 300 K for neat N3 film under continuous illumination of a 100 mW cm^{-2} white LED.

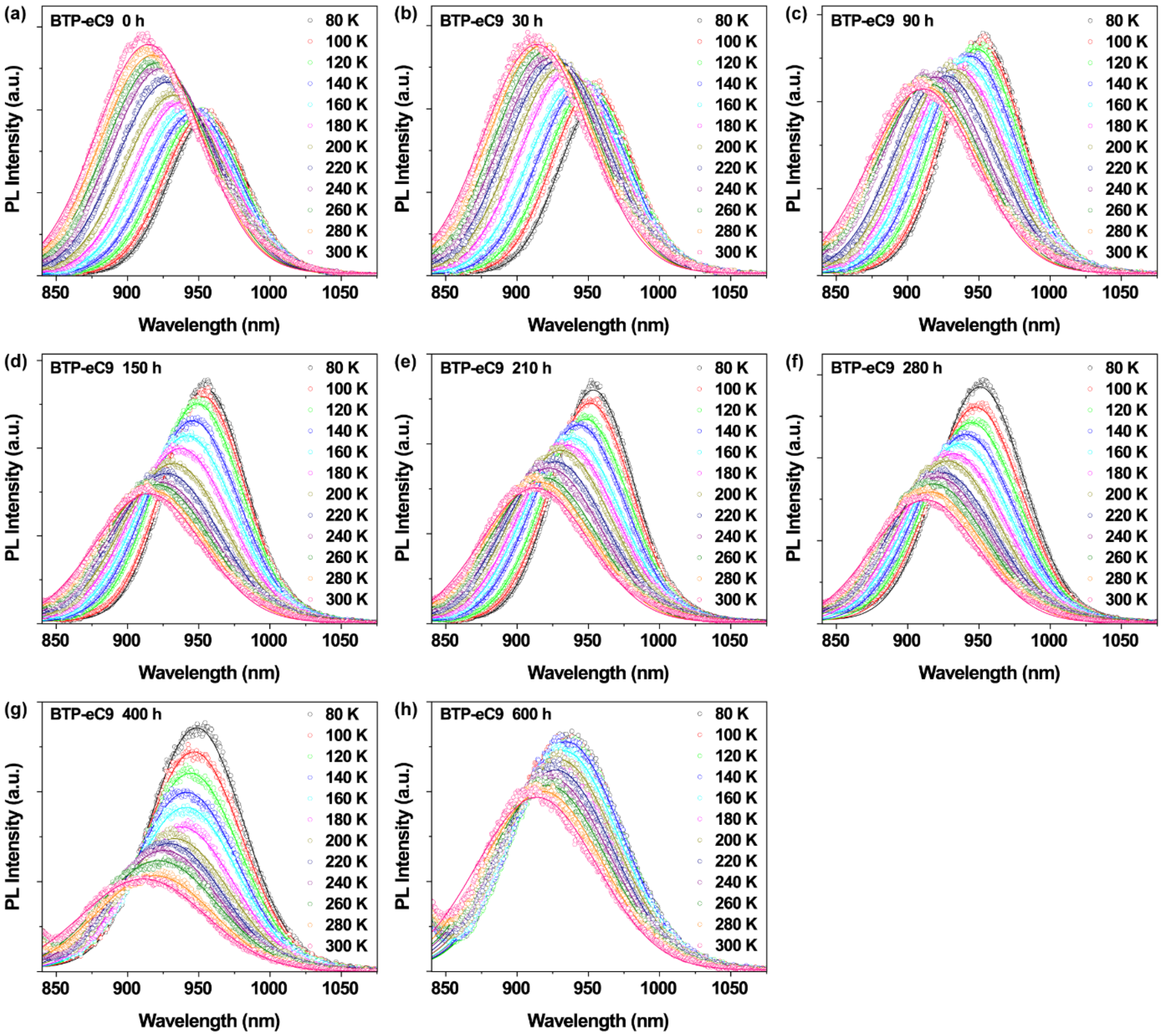

Fig. S33 (a-h) Temperature-dependent emission spectra of neat BTP-eC9 film as a function of time under continuous illumination of a 100 mW cm^{-2} white LED (Excite @ 800 nm).

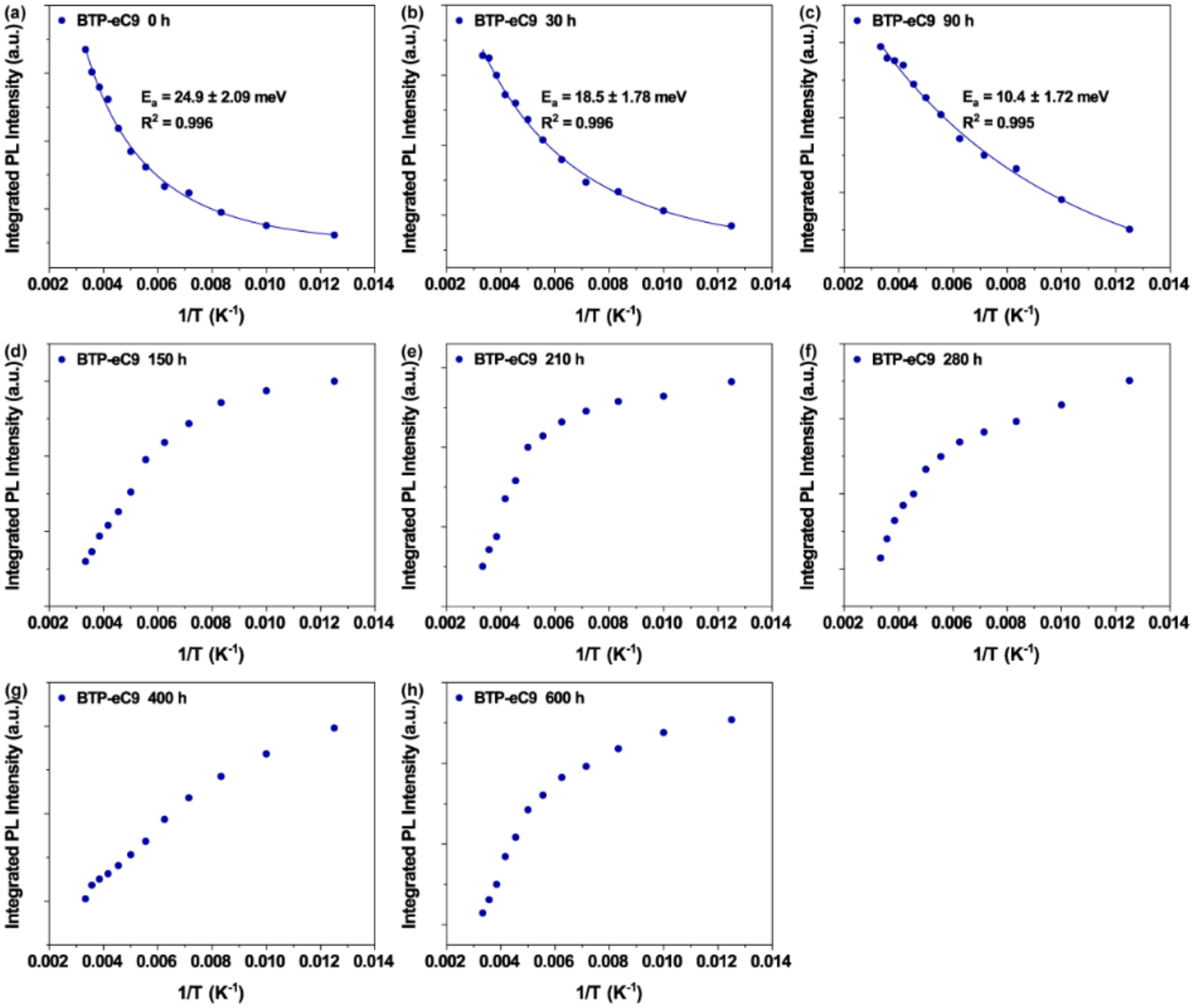

Fig. S34 (a-h) Evolution of emission intensity as a function of temperature from 80 to 300 K for neat BTP-eC9 film under continuous illumination of a 100 mW cm^{-2} white LED.

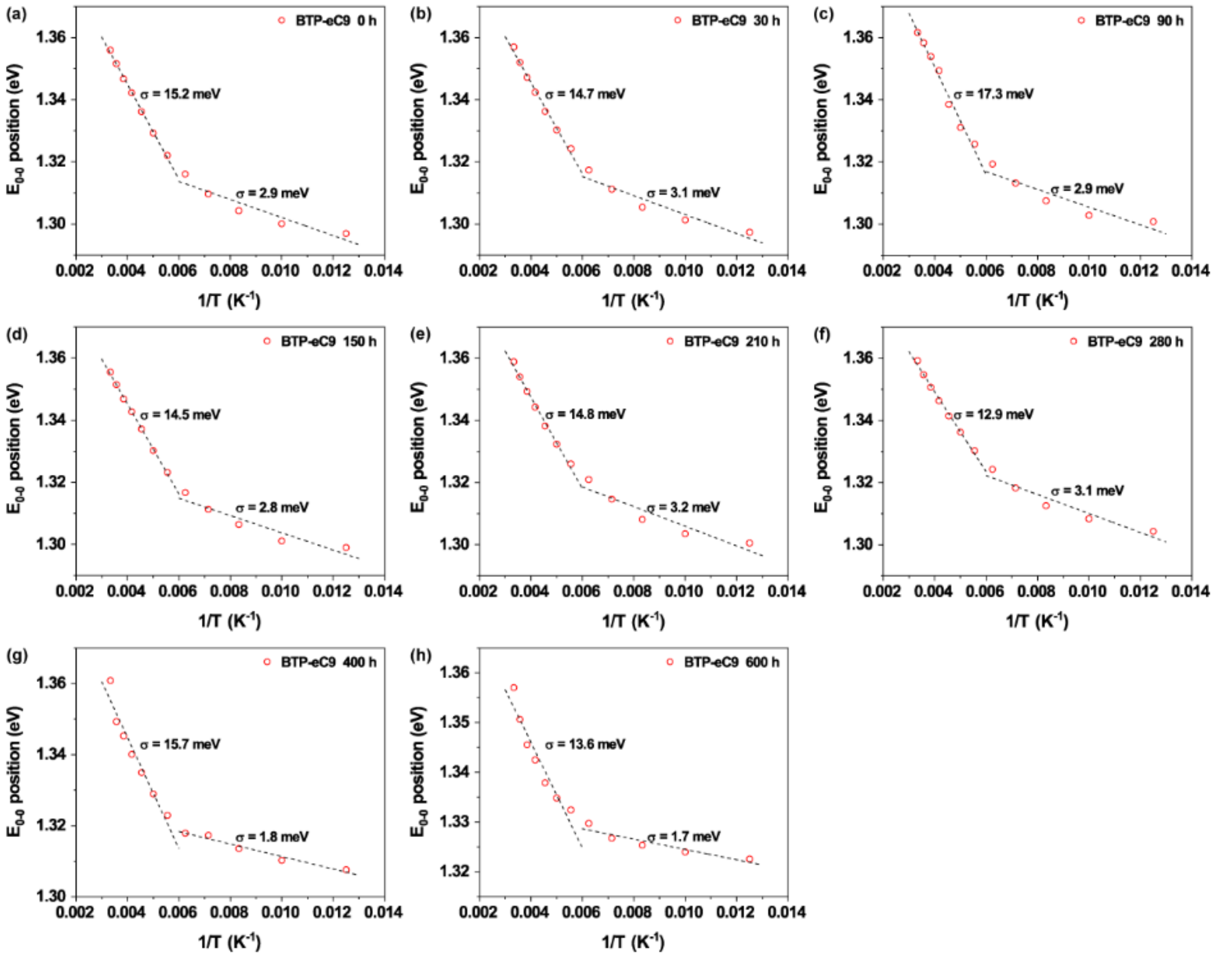

Fig. S35 (a-h) Evolution of 0-0 emission peak energy as a function of temperature from 80 to 300 K for neat BTP-eC9 film under continuous illumination of a 100 mW cm^{-2} white LED.

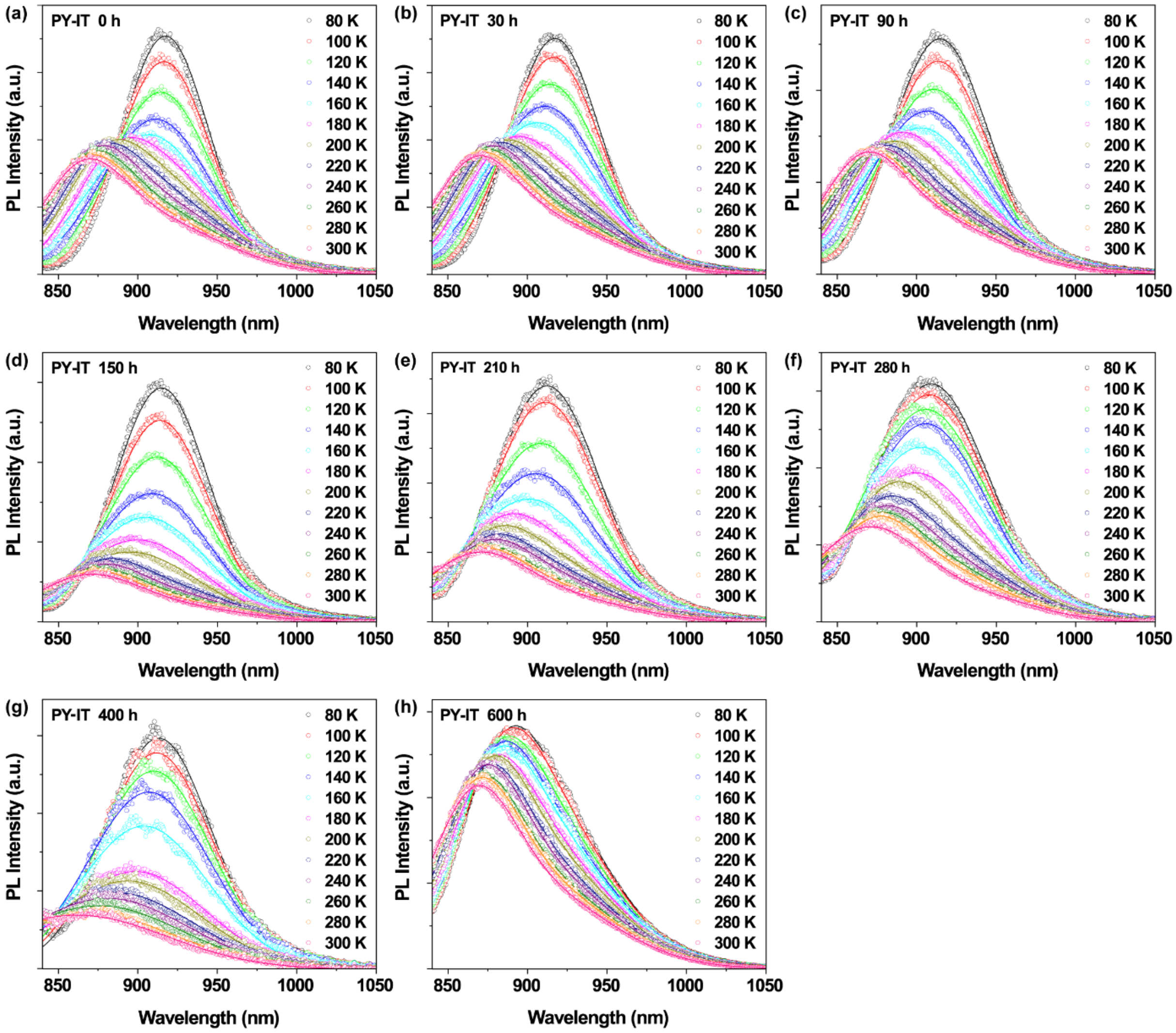

Fig. S36 (a-h) Temperature-dependent emission spectra of neat PY-IT film as a function of time under continuous illumination of a 100 mW cm^{-2} white LED (Excite @ 800 nm).

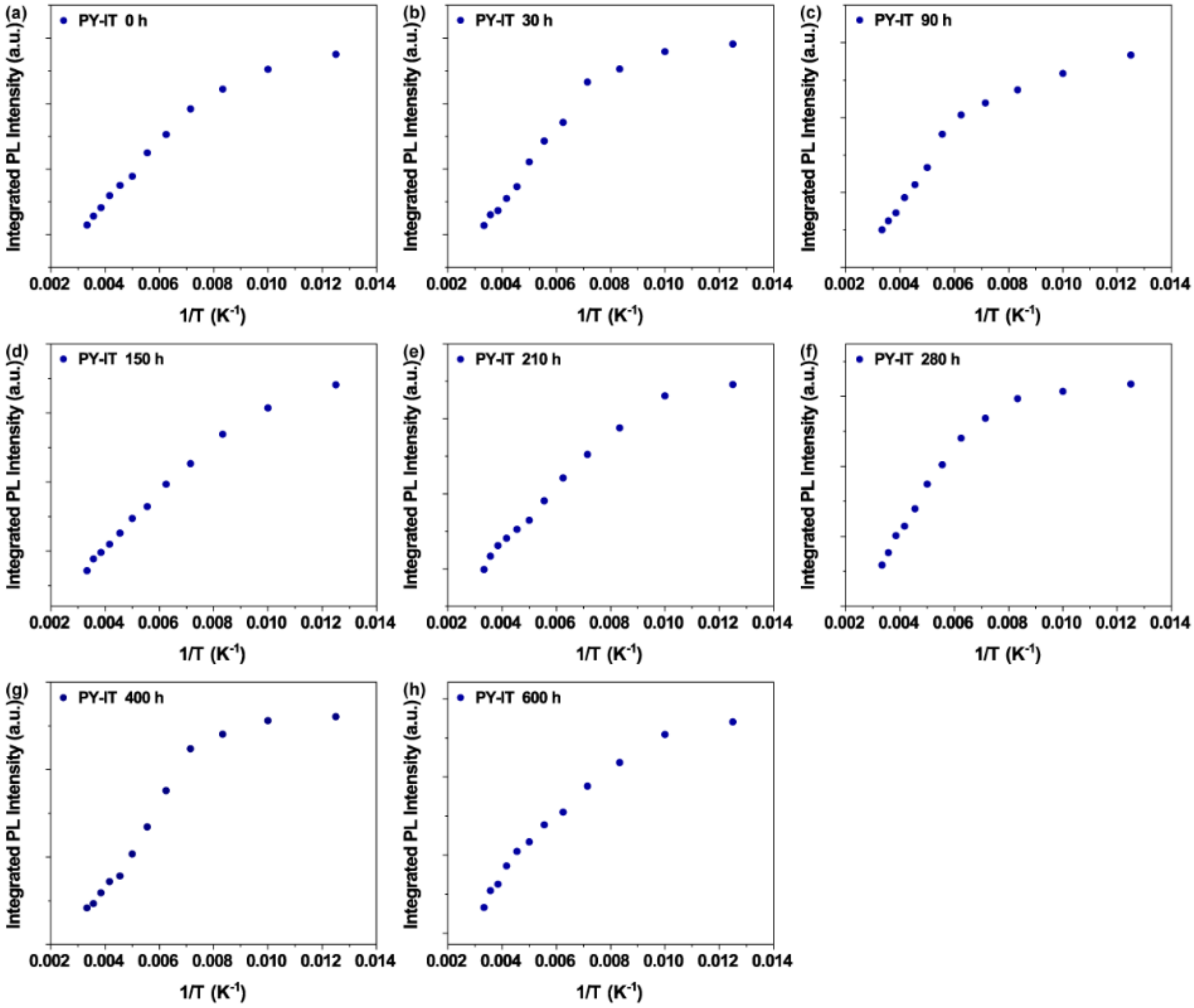

Fig. S37 (a-h) Evolution of emission intensity as a function of temperature from 80 to 300 K for neat PY-IT film under continuous illumination of a 100 mW cm^{-2} white LED.

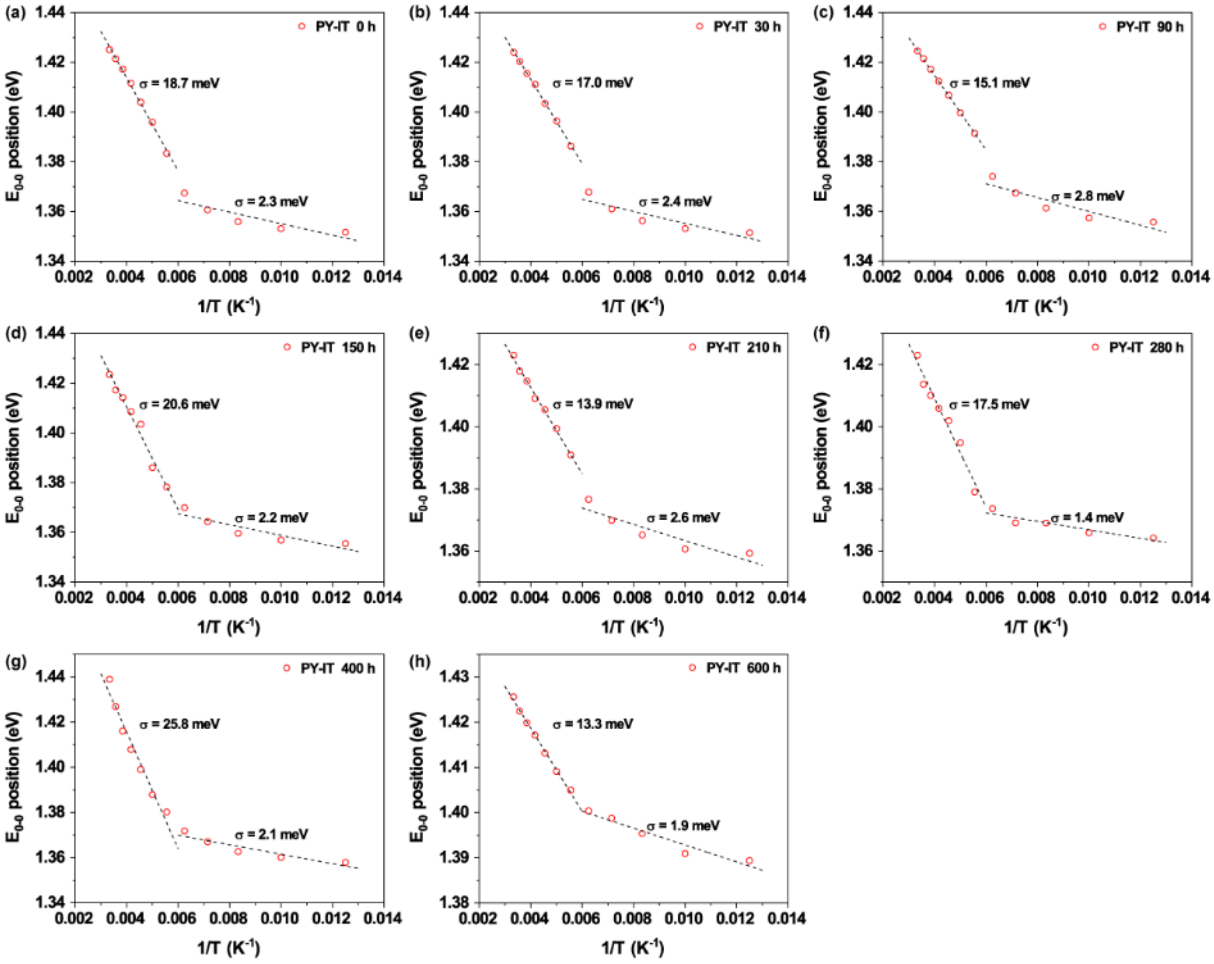

Fig. S38 (a-h) Evolution of 0-0 emission peak energy as a function of temperature from 80 to 300 K for neat PY-IT film under continuous illumination of a 100 mW cm^{-2} white LED.

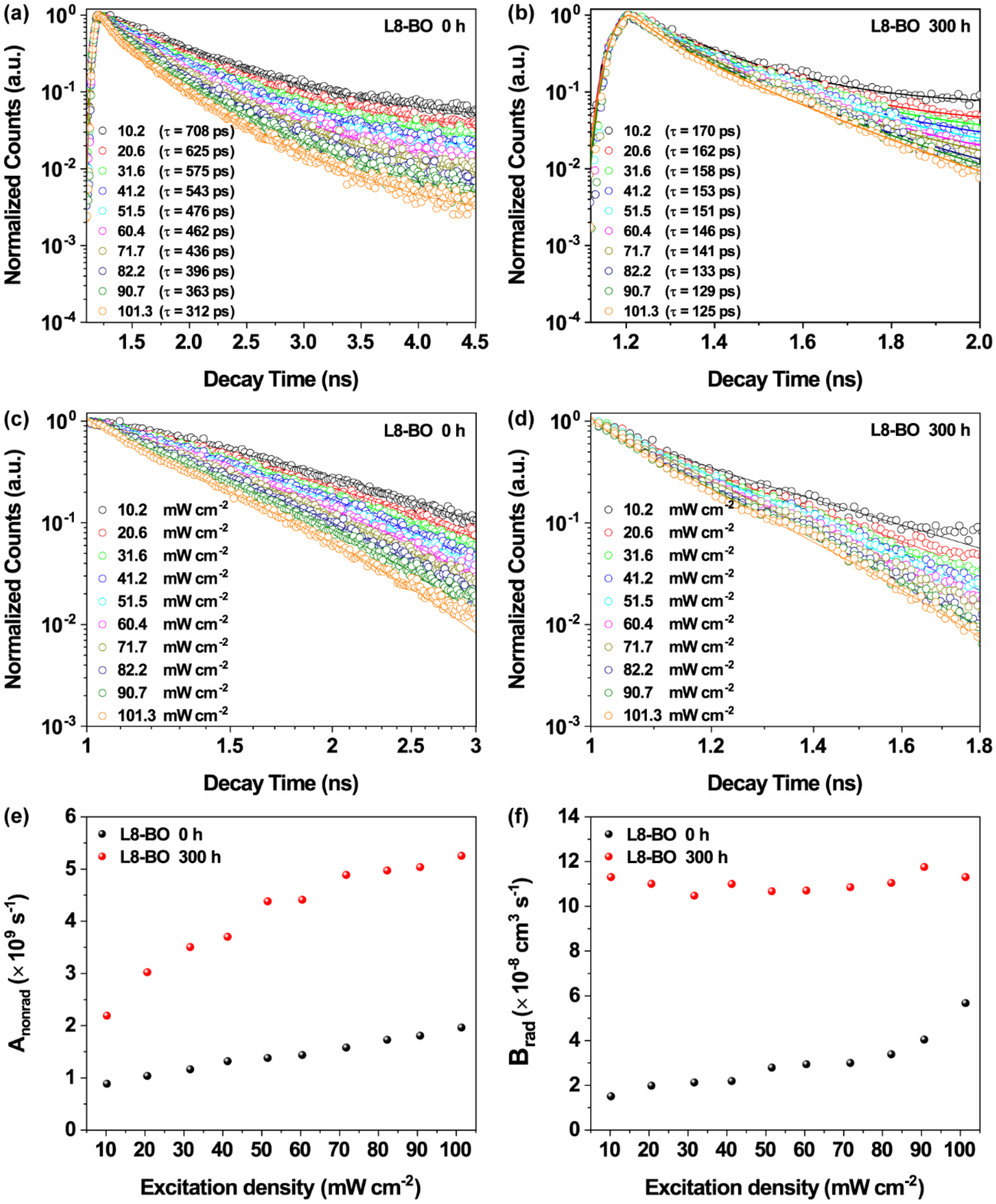

Fig. S39 Excitation density dependent TRPL dynamics at 880 nm of neat L8-BO film under continuous illumination of a 100 mW cm^{-2} white LED for (a) 0 h and (b) 300 h (Excite @ 800 nm). Excitation density dependent TRPL fitting curves of neat L8-BO film under continuous illumination of a 100 mW cm^{-2} white LED for (c) 0 h and (d) 300 h. (e) Nonradiative and (f) radiative recombination parameters as a function of excitation density for neat L8-BO film before and after continuous illumination.

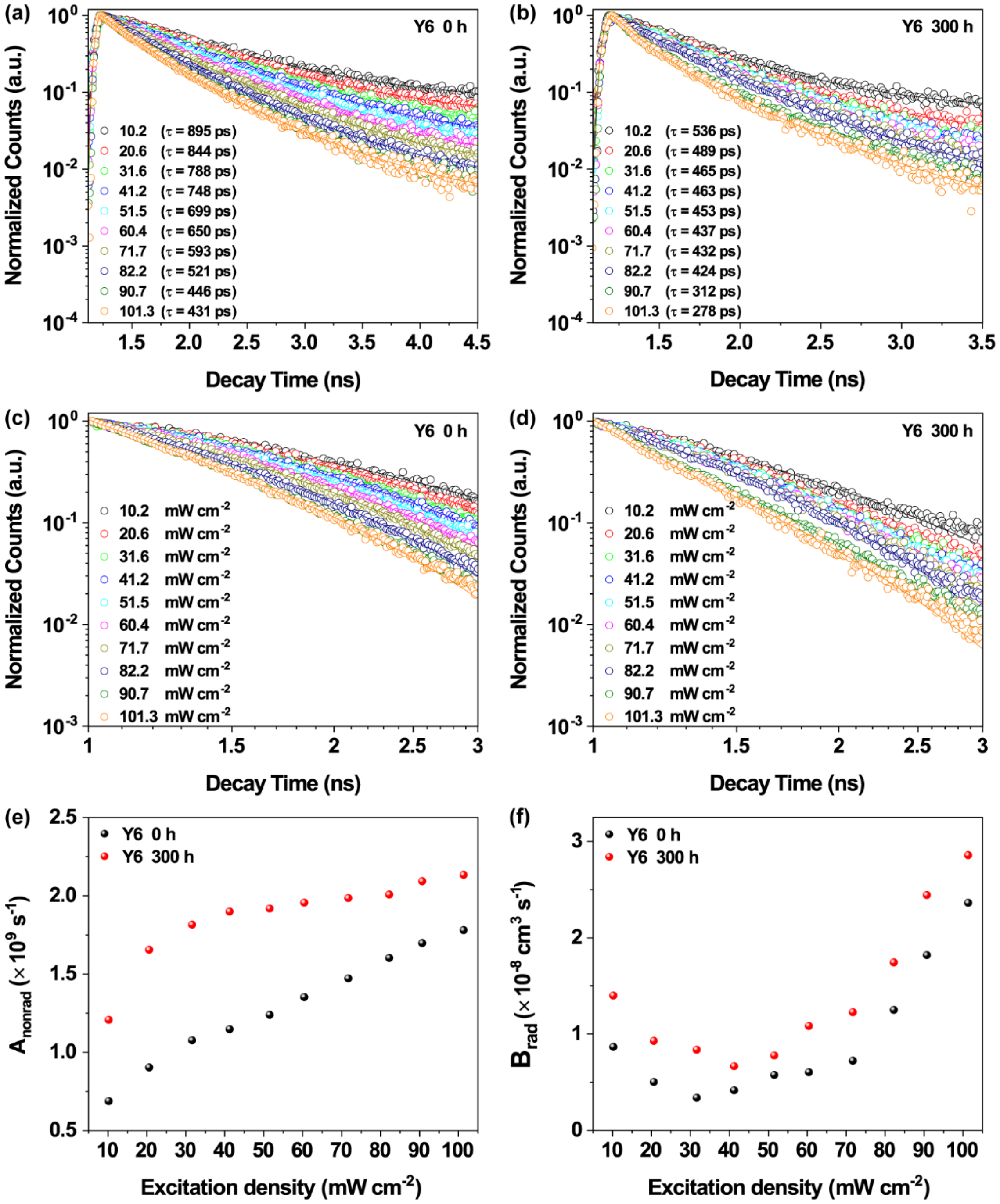

Fig. S40 Excitation density dependent TRPL dynamics at 880 nm of neat Y6 film under continuous illumination of a 100 mW cm^{-2} white LED for (a) 0 h and (b) 300 h (Excite @ 800 nm). Excitation density dependent TRPL fitting curves of neat Y6 film under continuous illumination of a 100 mW cm^{-2} white LED for (c) 0 h and (d) 300 h. (e) Nonradiative and (f) radiative recombination parameters as a function of excitation density for neat Y6 film before and after continuous illumination.

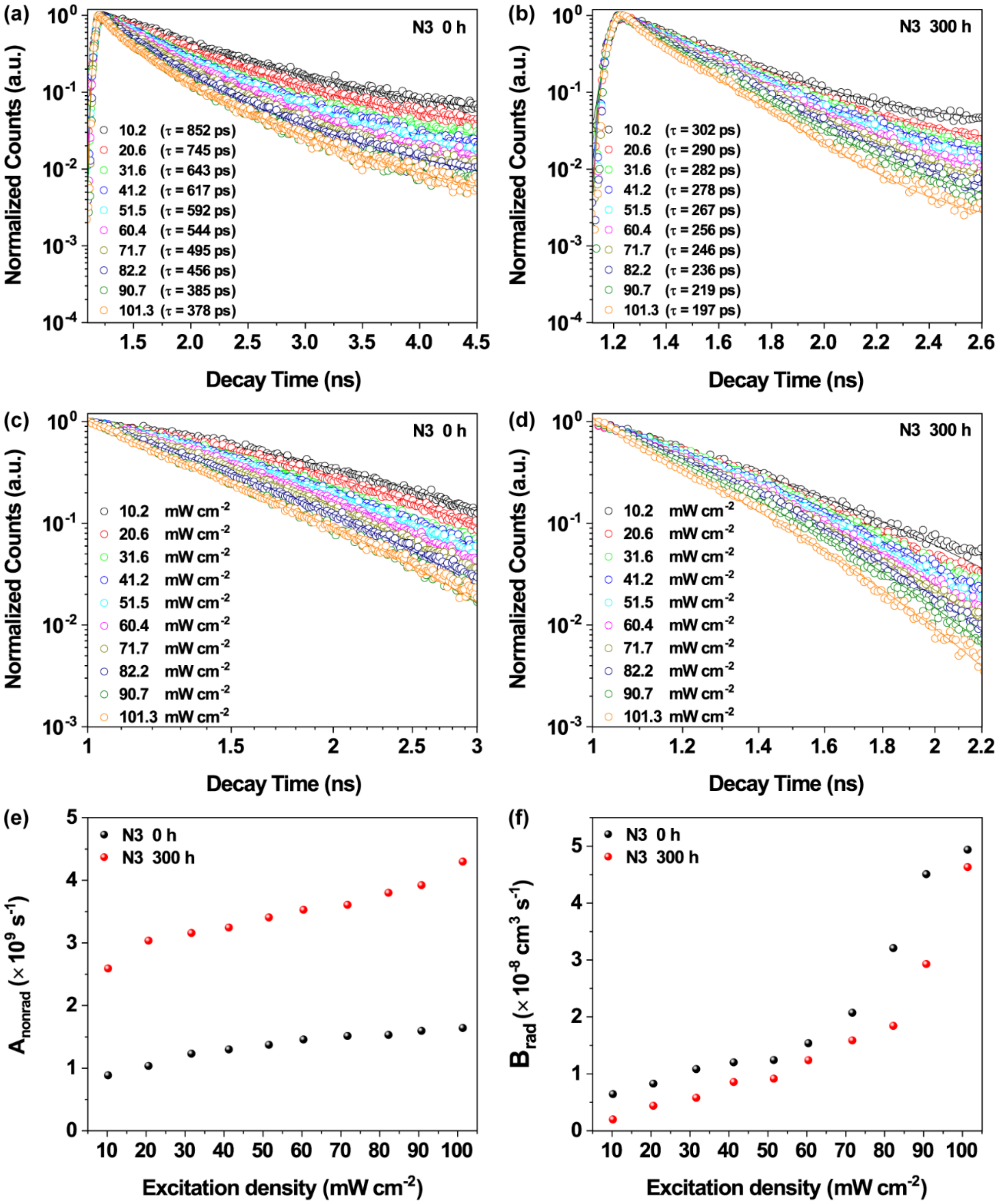

Fig. S41 Excitation density dependent TRPL dynamics at 880 nm of neat N3 film under continuous illumination of a 100 mW cm^{-2} white LED for (a) 0 h and (b) 300 h (Excite @ 800 nm). Excitation density dependent TRPL fitting curves of neat N3 film under continuous illumination of a 100 mW cm^{-2} white LED for (c) 0 h and (d) 300 h. (e) Nonradiative and (f) radiative recombination parameters as a function of excitation density for neat N3 film before and after continuous illumination.

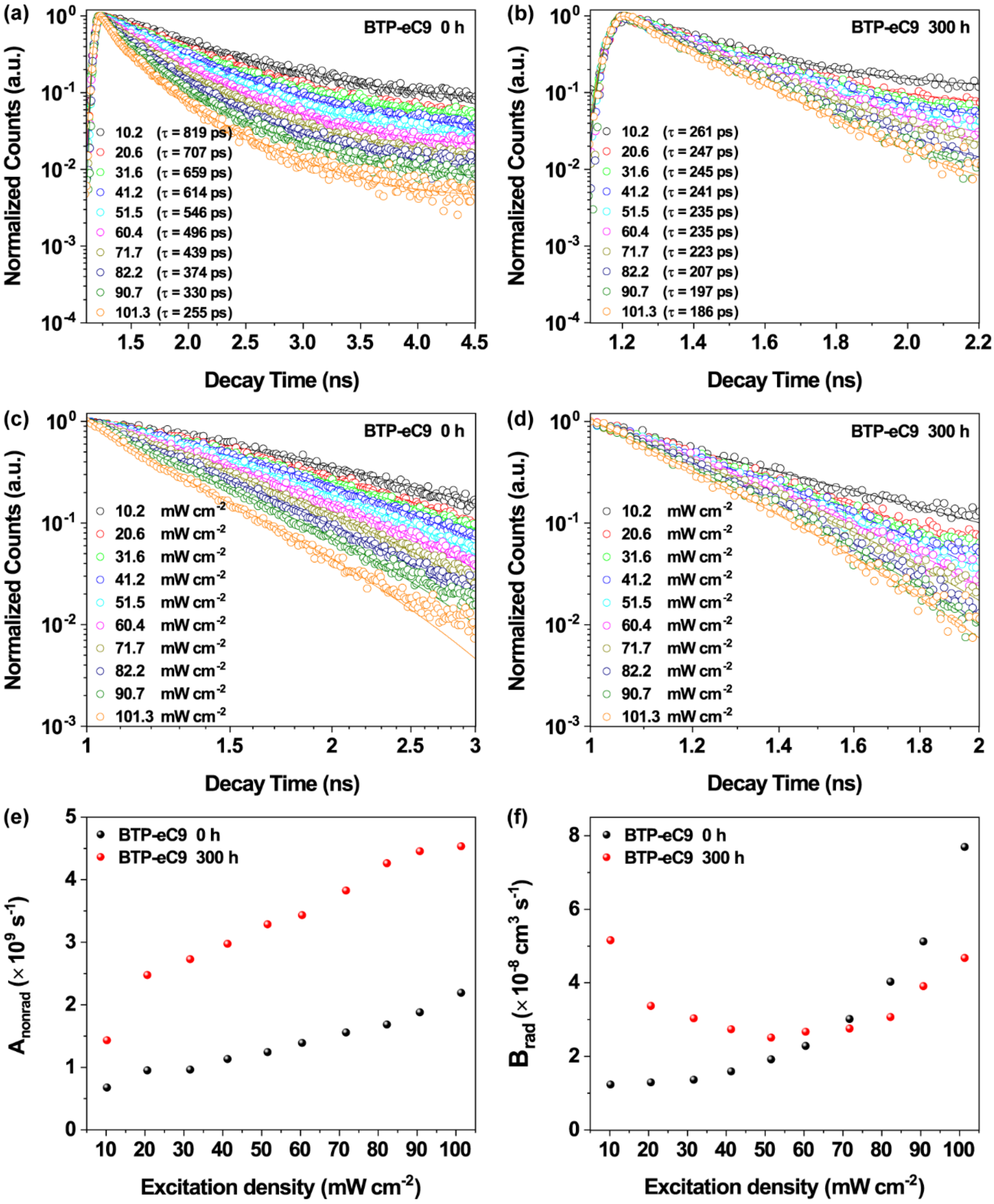

Fig. S42 Excitation density dependent TRPL dynamics at 880 nm of neat BTP-eC9 film under continuous illumination of a 100 mW cm^{-2} white LED for (a) 0 h and (b) 300 h (Excite @ 800 nm). Excitation density dependent TRPL fitting curves of neat BTP-eC9 film under continuous illumination of a 100 mW cm^{-2} white LED for (c) 0 h and (d) 300 h. (e) Nonradiative and (f) radiative recombination parameters as a function of excitation density for neat BTP-eC9 film before and after continuous illumination.

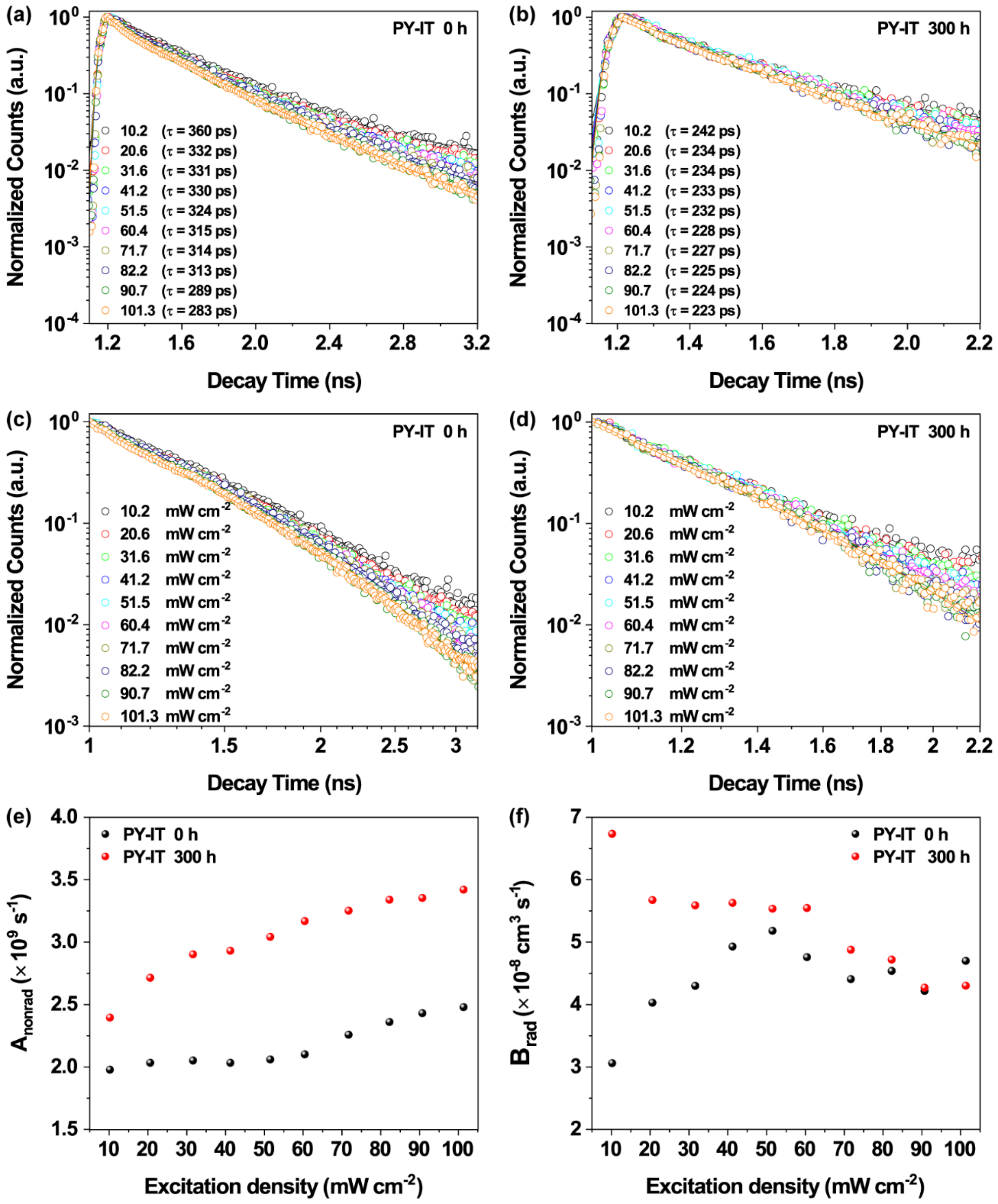

Fig. S43 Excitation density dependent TRPL dynamics at 880 nm of neat PY-IT film under continuous illumination of a 100 mW cm^{-2} white LED for (a) 0 h and (b) 300 h (Excite @ 800 nm). Excitation density dependent TRPL fitting curves of neat PY-IT film under continuous illumination of a 100 mW cm^{-2} white LED for (c) 0 h and (d) 300 h. (e) Nonradiative and (f) radiative recombination parameters as a function of excitation density for neat PY-IT film before and after continuous illumination.

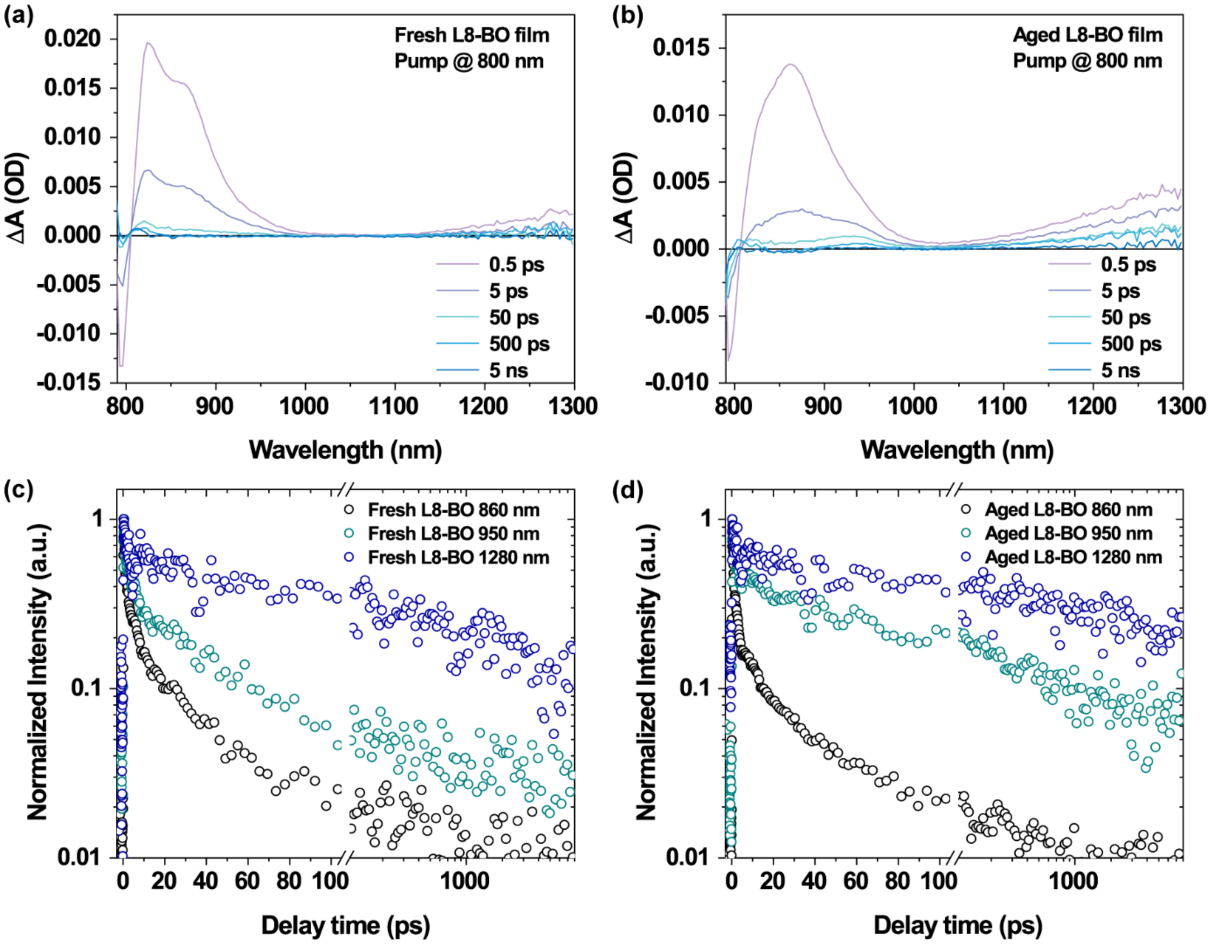

Fig. S44 TA spectra of neat L8-BO film (a) before and (b) after continuous illumination. TA kinetic traces probed at 860 nm, 950 nm and 1280 nm for neat L8-BO film (c) before and (d) after continuous illumination.

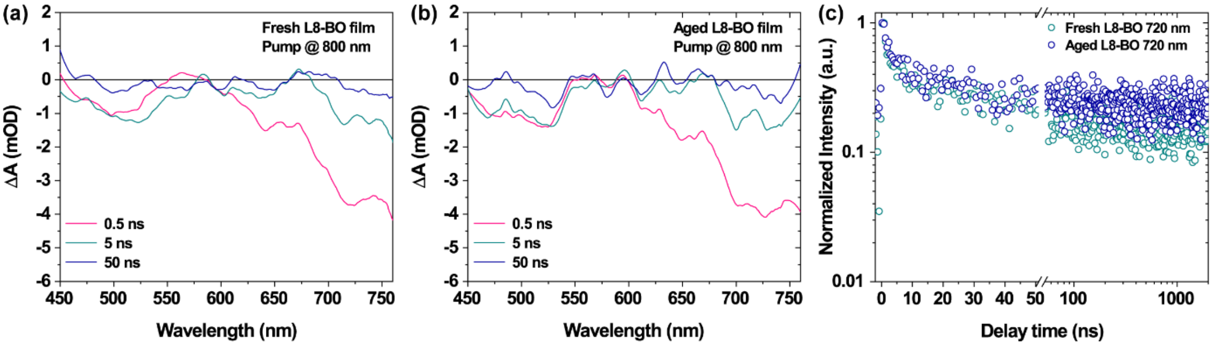

Fig. S45 The nanosecond (ns)-resolved TA spectra of neat L8-BO film (a) before and (b) after continuous illumination. (c) The ns-resolved TA kinetic traces probed at 720 nm for neat L8-BO film before and after continuous illumination.

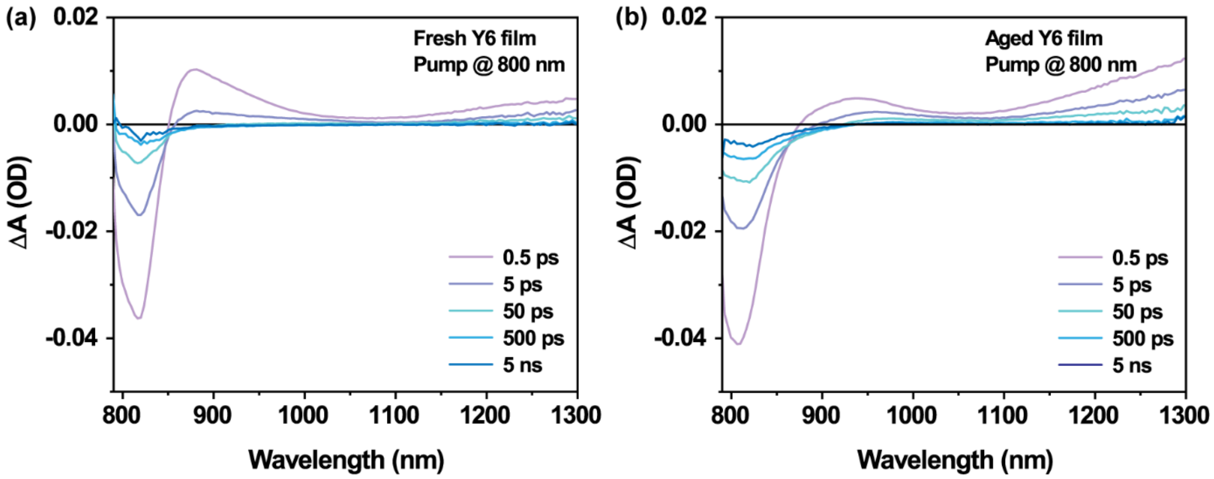

Fig. S46 TA spectra of neat Y6 film (a) before and (b) after continuous illumination.

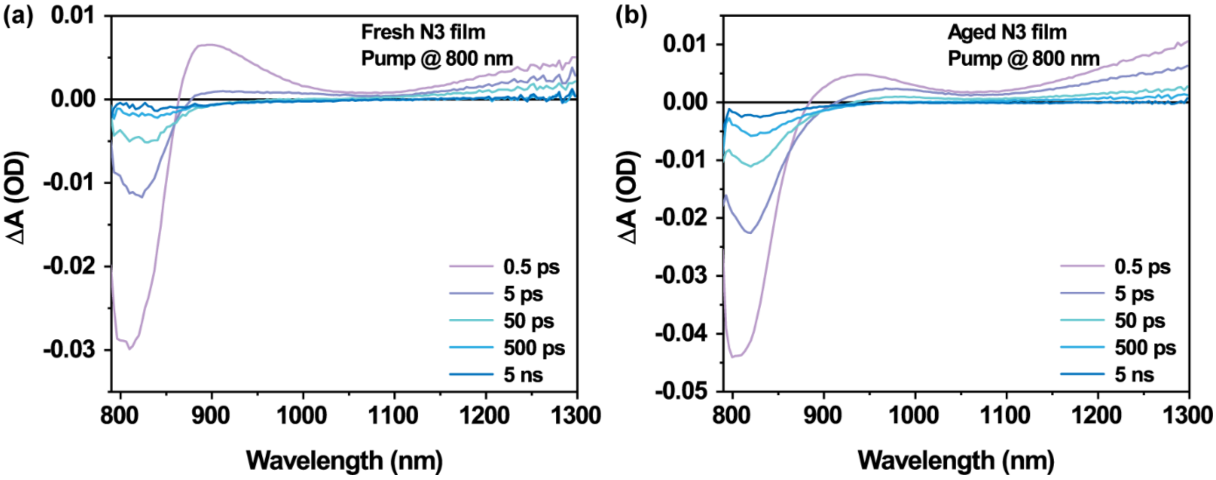

Fig. S47 TA spectra of neat N3 film (a) before and (b) after continuous illumination.

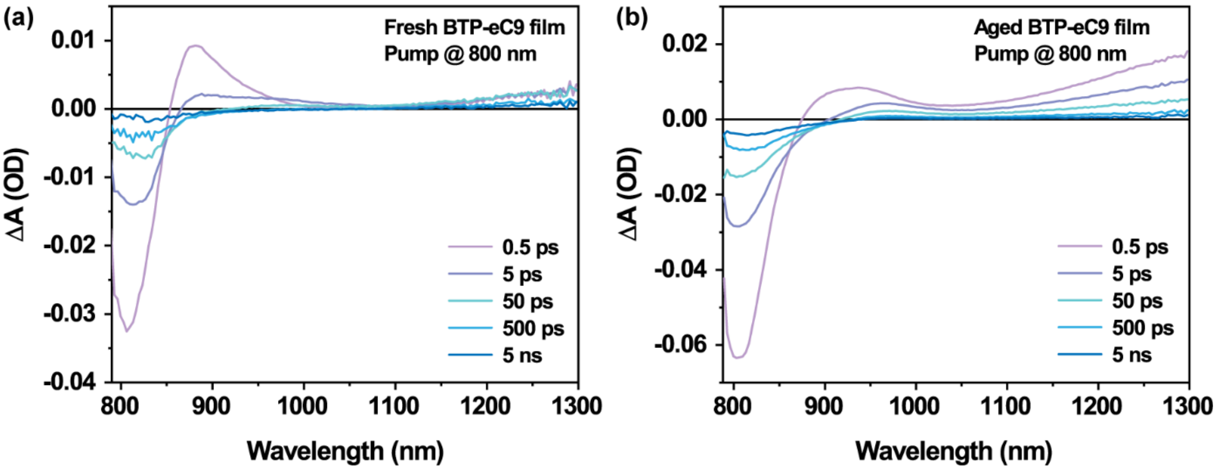

Fig. S48 TA spectra of neat BTP-eC9 film (a) before and (b) after continuous illumination.

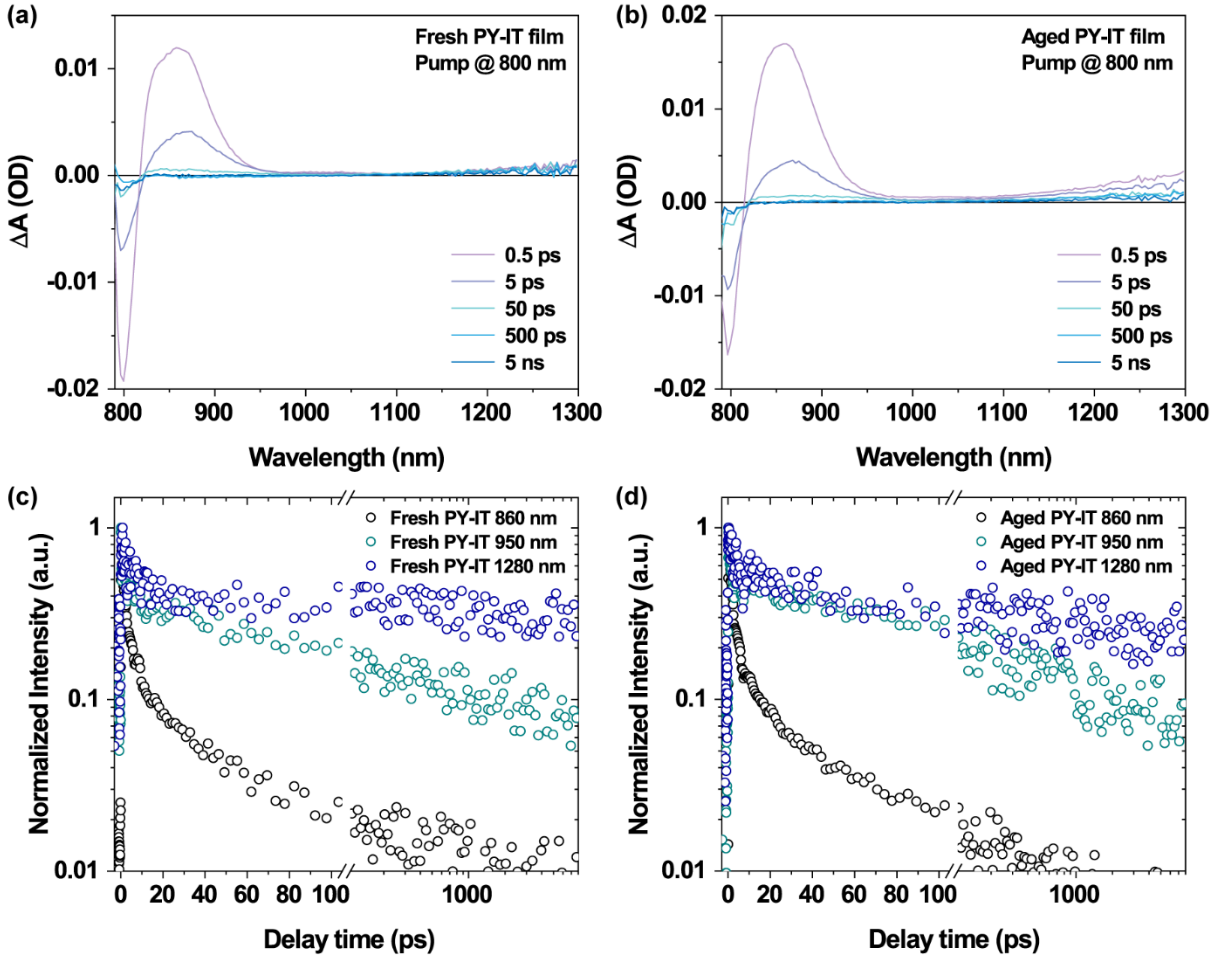

Fig. S49 TA spectra of neat PY-IT film (a) before and (b) after continuous illumination. TA kinetic traces probed at 860 nm, 950 nm and 1280 nm for neat PY-IT film (c) before and (d) after continuous illumination.

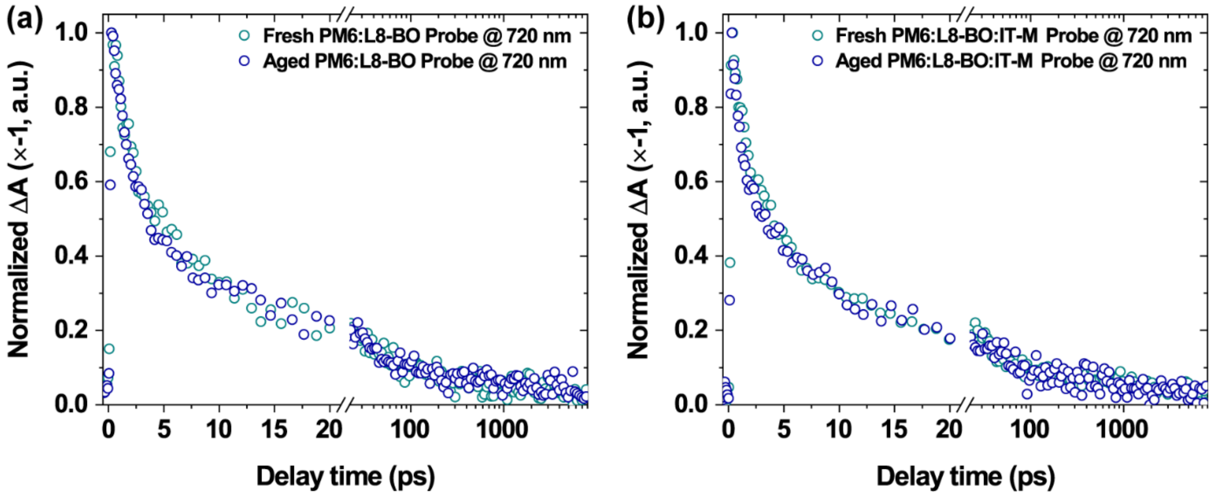

Fig. S50 TA kinetic traces for (a) binary PM6:L8-BO and (b) ternary PM6:L8-BO:IT-M films before and after continuous illumination.

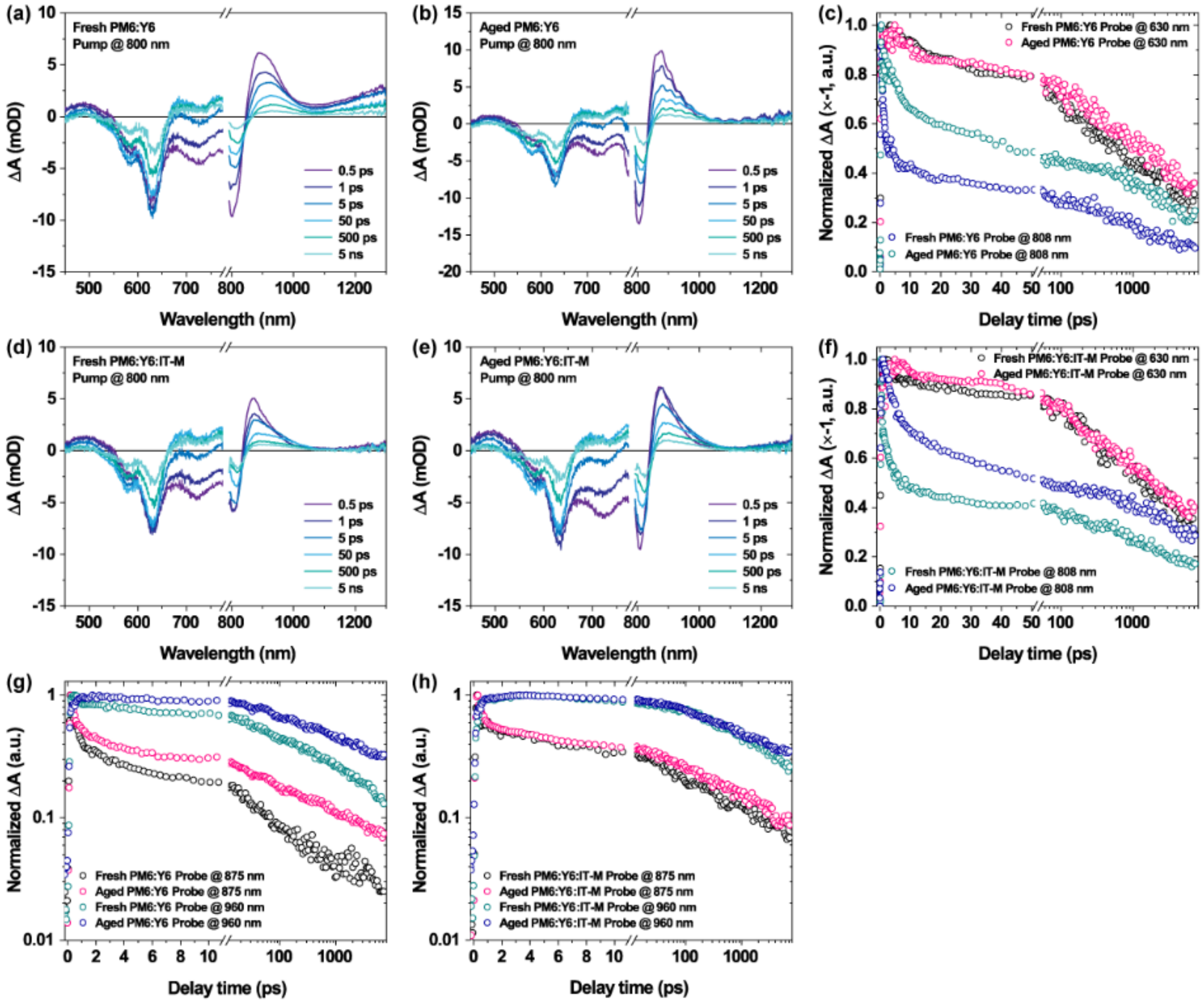

Fig. S51 TA spectra of PM6:Y6 films (a) before and (b) after continuous illumination. (c) TA kinetic traces for PM6:Y6 films before and after continuous illumination. TA spectra of PM6:Y6:IT-M films (d) before and (e) after continuous illumination. (f) TA kinetic traces for PM6:Y6:IT-M films before and after continuous illumination. TA kinetic traces for (g) PM6:Y6 and (h) PM6:Y6:IT-M films before and after continuous illumination.

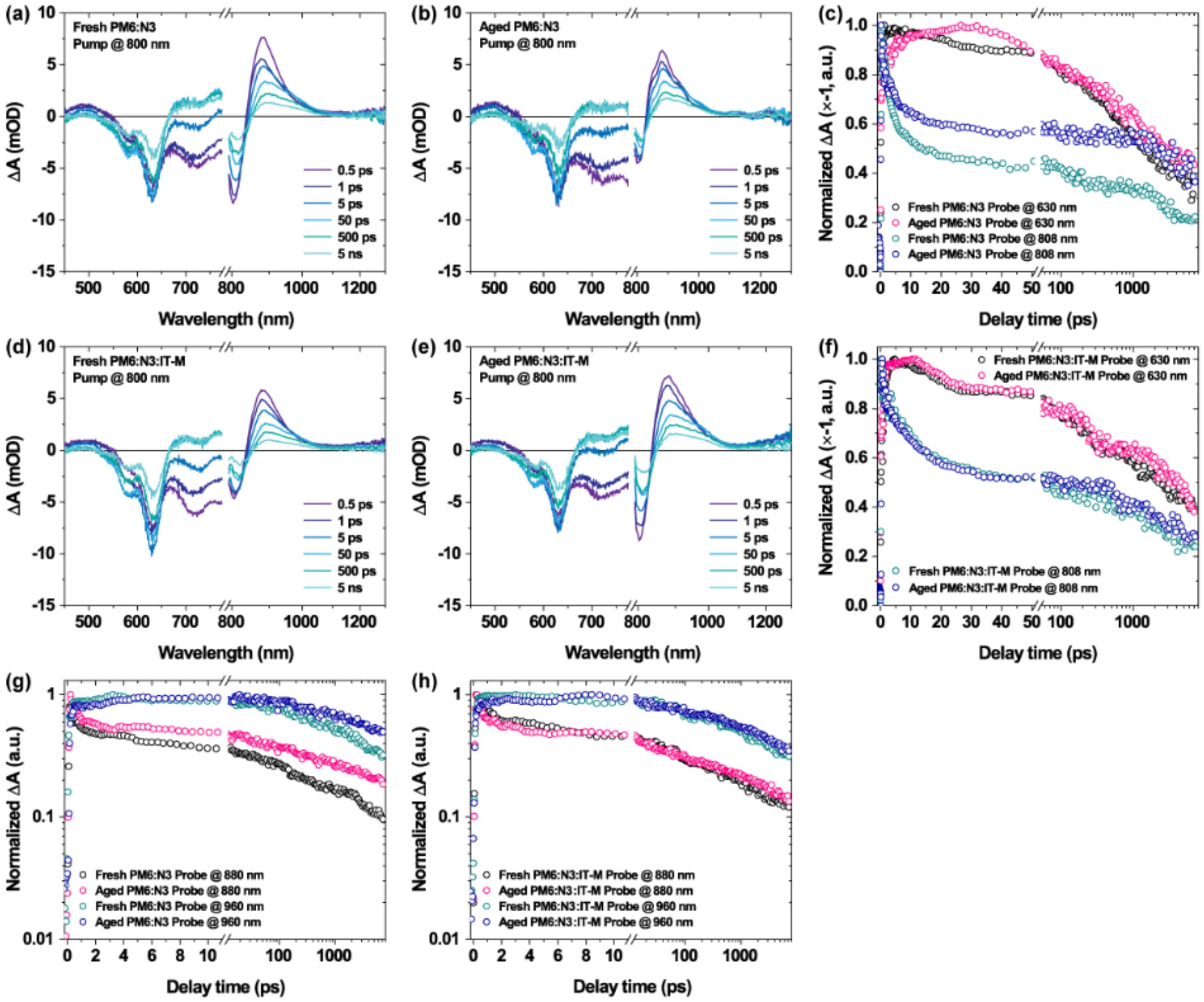

Fig. S52 TA spectra of PM6:N3 films (a) before and (b) after continuous illumination. (c) TA kinetic traces for PM6:N3 films before and after continuous illumination. TA spectra of PM6:N3:IT-M films (d) before and (e) after continuous illumination. (f) TA kinetic traces for PM6:N3:IT-M films before and after continuous illumination. TA kinetic traces for (g) PM6:N3 and (h) PM6:N3:IT-M films before and after continuous illumination.

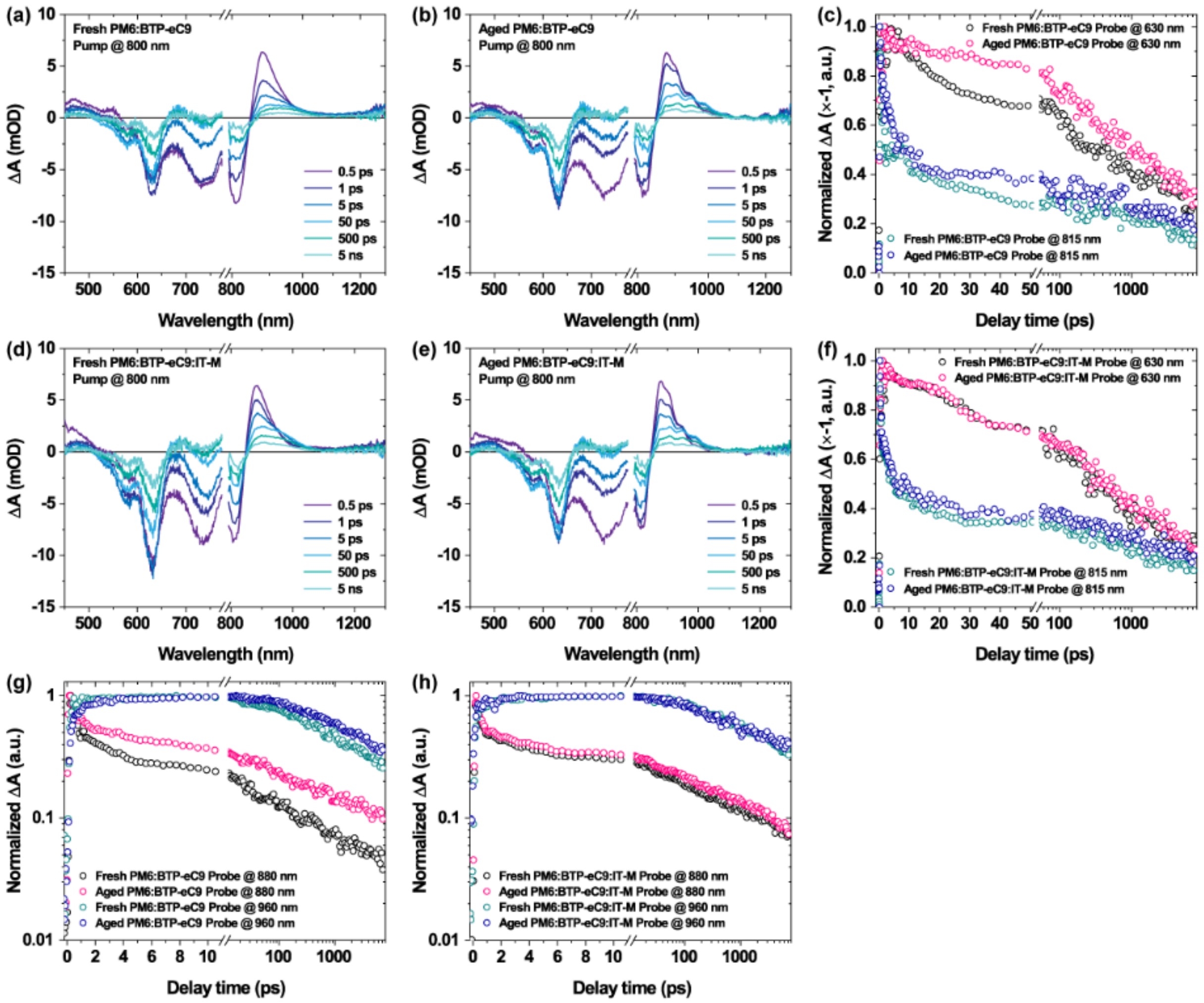

Fig. S53 TA spectra of PM6:BTP-eC9 films (a) before and (b) after continuous illumination. (c) TA kinetic traces for PM6:BTP-eC9 films before and after continuous illumination. TA spectra of PM6:BTP-eC9:IT-M films (d) before and (e) after continuous illumination. (f) TA kinetic traces for PM6:BTP-eC9:IT-M films before and after continuous illumination. TA kinetic traces for (g) PM6:BTP-eC9 and (h) PM6:BTP-eC9:IT-M films before and after continuous illumination.

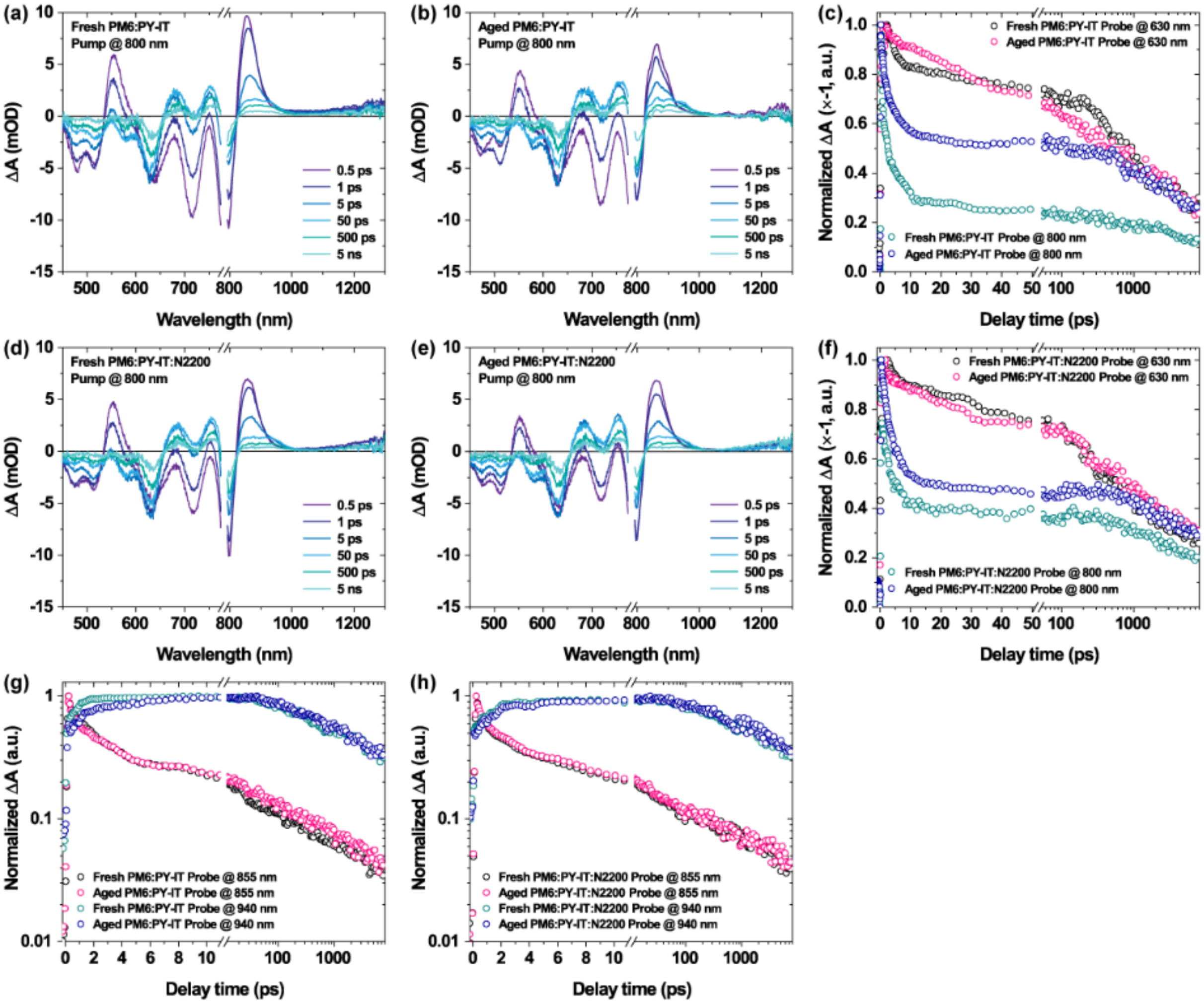

Fig. S54 TA spectra of PM6:PY-IT films (a) before and (b) after continuous illumination. (c) TA kinetic traces for PM6:PY-IT films before and after continuous illumination. TA spectra of PM6:PY-IT:N2200 films (d) before and (e) after continuous illumination. (f) TA kinetic traces for PM6:PY-IT:N2200 films before and after continuous illumination. TA kinetic traces for (g) PM6:PY-IT and (h) PM6:PY-IT:N2200 films before and after continuous illumination.

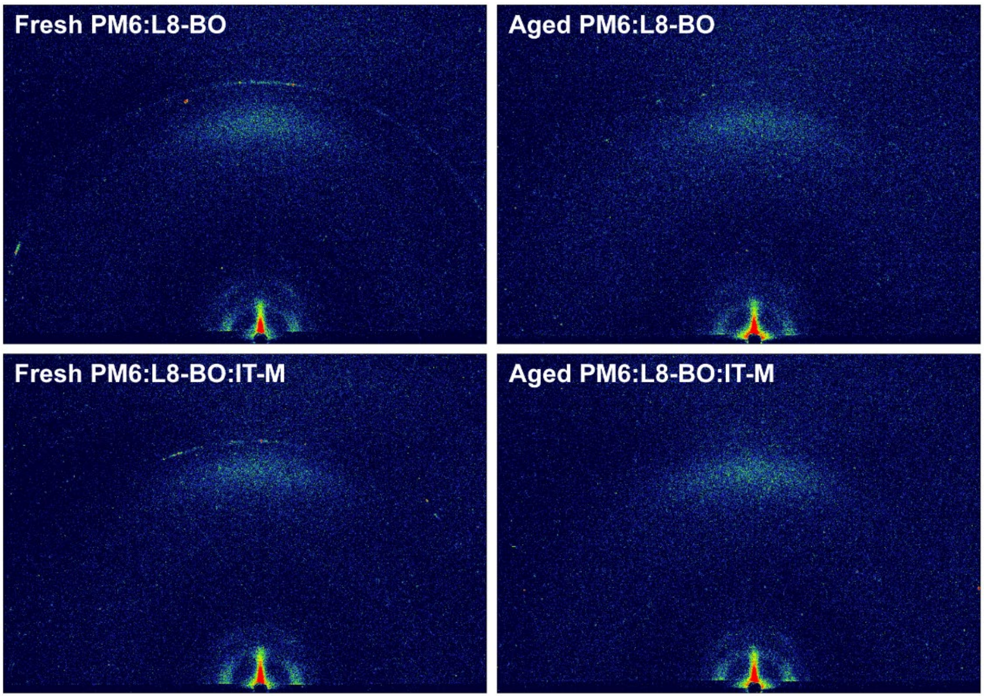

Fig. S55 GIWAXS patterns of PM6:L8-BO-based binary and ternary blends before and after continuous illumination.

Table S1. Key parameters of contact angle measurements by using water and glycerol droplets.

Materials	**θ_{water} (°)**	**$\theta_{glycerol}$ (°)**	**γ (mN m^{-1})**	**χ with PM6**	**χ with L8-BO**
PM6	100.3	88.1	29.4	/	0.130
L8-BO	90.2	77.9	33.4	0.130	/
IT-M	91.5	78.6	35.0	0.250	0.020

Table S2. Photovoltaic parameters of binary PM6:L8-BO OSCs with different device structures under the illumination of AM 1.5G at 100 mW cm^{-2}.

Active layer	**Device structure**	**V_{OC} (V)**	**J_{SC} (mA cm^{-2})**	**FF (%)**	**PCE$^{(a)}$ (%)**
PM6:L8-BO	control	0.865 (0.864±0.005)	25.74 (25.36±0.47)	77.66 (77.35±0.61)	17.29 (17.03±0.25)
PM6:L8-BO	V_2O_5/PEDOT:PSS	0.866 (0.865±0.006)	25.90 (25.57±0.45)	77.89 (77.65±0.58)	17.47 (17.22±0.24)
PM6:L8-BO	LiF/PDINN	0.865 (0.865±0.005)	25.82 (25.44±0.43)	78.44 (78.23±0.64)	17.52 (17.28±0.21)
PM6:L8-BO	bilayered interfaces	0.871 (0.868±0.004)	25.77 (25.48±0.34)	78.68 (78.37±0.66)	17.66 (17.42±0.23)

(a)The statistical values extracted from 8 independent devices.

Table S3. Photovoltaic parameters of PM6:L8-BO-based ternary OSCs with various IT-M content under the illumination of AM 1.5G at 100 mW cm^{-2}.

Active layer	**Device structure**	**V_{OC} (V)**	**J_{SC} (mA cm^{-2})**	**FF (%)**	**PCE$^{(a)}$ (%)**
1:1.20:0	bilayered interfaces	0.871 (0.868±0.004)	25.77 (25.48±0.34)	78.68 (78.37±0.66)	17.66 (17.42±0.23)
1:1.17:0.03	bilayered interfaces	0.873 (0.870±0.006)	26.08 (25.72±0.42)	79.15 (78.56±0.62)	18.02 (17.64±0.36)
1:1.15:0.05	bilayered interfaces	0.875 (0.872±0.005)	26.22 (25.85±0.39	79.29 (78.64±0.83)	18.19 (17.83±0.34)
1:1.13:0.07	bilayered interfaces	0.867 (0.865±0.006)	25.89 (25.54±0.41)	78.41 (77.97±0.54)	17.60 (17.25±0.32)

(a)The statistical values extracted from 8 independent devices.

Table S4. Photovoltaic parameters of PM6:Y6-based ternary OSCs with various IT-M content under the illumination of AM 1.5G at 100 mW cm^{-2}.

Active layer	**Device structure**	**V_{OC} (V)**	**J_{SC} (mA cm^{-2})**	**FF (%)**	**PCE$^{(a)}$ (%)**
1:1.20:0	bilayered interfaces	0.833 (0.830±0.004)	25.31 (25.28±0.28)	77.19 (76.62±0.72)	16.27 (16.08±0.18)
1:1.17:0.03	bilayered interfaces	0.854 (0.851±0.005)	25.68 (25.42±0.37)	77.34 (76.96±0.58)	16.96 (16.67±0.26)
1:1.15:0.05	bilayered interfaces	0.859 (0.855±0.006)	25.87 (25.57±0.32)	77.58 (77.22±0.56)	17.24 (16.91±0.29)
1:1.13:0.07	bilayered interfaces	0.849 (0.845±0.005)	25.41 (25.32±0.34)	76.37 (75.68±0.71)	16.48 (16.12±0.34)

(a)The statistical values extracted from 8 independent devices.

Table S5. Photovoltaic parameters of PM6:N3-based ternary OSCs with various IT-M content under the illumination of AM 1.5G at 100 mW cm^{-2}.

Active layer	Device structure	V_{OC} (V)	J_{SC} (mA cm^{-2})	FF (%)	PCE$^{(a)}$ (%)
1:1.20:0	bilayered interfaces	0.831 (0.828±0.006)	25.49 (25.45±0.26)	77.10 (76.46±0.75)	16.33 (16.11±0.22)
1:1.17:0.03	bilayered interfaces	0.853 (0.847±0.007)	25.84 (25.58±0.33)	77.15 (76.81±0.53)	17.01 (16.71±0.28)
1:1.15:0.05	bilayered interfaces	0.856 (0.852±0.005)	25.96 (25.66±0.34)	77.45 (77.08±0.64)	17.21 (16.86±0.34)
1:1.13:0.07	bilayered interfaces	0.850 (0.843±0.008)	25.60 (25.52±0.37)	75.89 (75.26±0.74)	16.51 (16.15±0.32)

(a) The statistical values extracted from 8 independent devices.

Table S6. Photovoltaic parameters of PM6:BTP-eC9-based ternary OSCs with various IT-M content under the illumination of AM 1.5G at 100 mW cm^{-2}.

Active layer	Device structure	V_{OC} (V)	J_{SC} (mA cm^{-2})	FF (%)	PCE$^{(a)}$ (%)
1:1.20:0	bilayered interfaces	0.847 (0.842±0.006)	26.61 (26.38±0.31)	77.26 (76.89±0.65)	17.41 (17.12±0.28)
1:1.17:0.03	bilayered interfaces	0.859 (0.854±0.005)	26.65 (26.46±0.42)	77.58 (77.21±0.57)	17.76 (17.41±0.33)
1:1.15:0.05	bilayered interfaces	0.865 (0.858±0.007)	26.69 (26.55±0.36)	78.18 (77.46±0.76)	18.05 (17.72±0.31)
1:1.13:0.07	bilayered interfaces	0.852 (0.847±0.006)	26.52 (26.23±0.34)	76.13 (75.61±0.62)	17.20 (16.82±0.35)

(a) The statistical values extracted from 8 independent devices.

Table S7. Photovoltaic parameters of PM6:PY-IT-based ternary OSCs with various N2200 content under the illumination of AM 1.5G at 100 mW cm^{-2}.

Active layer	Device structure	V_{OC} (V)	J_{SC} (mA cm^{-2})	FF (%)	PCE$^{(a)}$ (%)
1:1:0	bilayered interfaces	0.941 (0.937±0.006)	22.89 (22.67±0.29)	71.25 (70.85±0.62)	15.35 (15.06±0.28)
1:0.99:0.01	bilayered interfaces	0.942 (0.938±0.005)	23.01 (22.73±0.35)	72.29 (71.84±0.56)	15.67 (15.33±0.32)
1:0.97:0.03	bilayered interfaces	0.943 (0.939±0.005)	23.05 (22.86±0.38)	73.76 (73.04±0.77)	16.03 (15.72±0.30)
1:0.95:0.05	bilayered interfaces	0.940 (0.936±0.004)	22.86 (22.62±0.33)	71.15 (70.55±0.58)	15.29 (14.97±0.29)

(a) The statistical values extracted from 8 independent devices.

Table S8. Photovoltaic parameters of binary and ternary OSCs based on various OPV systems with different device structures.

Active layer	**Device structure**	J_{sat} (mA cm^{-2})	J_{ph}^{*} (mA cm^{-2})	$J_{\mathrm{ph}}^{\#}$ (mA cm^{-2})	P_{diss} (%)	P_{coll} (%)
PM6:L8-BO	control	26.06	25.74	23.46	98.77	90.02
PM6:L8-BO	bilayered interfaces	26.29	25.97	24.04	98.78	91.44
PM6:L8-BO:IT-M	bilayered interfaces	26.55	26.25	24.58	98.87	92.58
PM6:Y6	control	25.67	25.20	22.94	98.17	89.37
PM6:Y6	bilayered interfaces	25.86	25.48	23.46	98.53	90.72
PM6:Y6:IT-M	bilayered interfaces	26.22	25.87	24.11	98.67	91.95
PM6:N3	control	25.77	25.32	22.97	98.25	89.14
PM6:N3	bilayered interfaces	25.89	25.49	23.47	98.46	90.65
PM6:N3:IT-M	bilayered interfaces	26.32	25.96	23.99	98.63	91.15
PM6:BTP-eC9	control	26.89	26.52	24.07	98.62	89.51
PM6:BTP-eC9	bilayered interfaces	26.97	26.61	24.50	98.67	90.84
PM6:BTP-eC9:IT-M	bilayered interfaces	27.04	26.69	24.93	98.71	92.20
PM6:PY-IT	control	23.43	22.85	19.52	97.53	83.31
PM6:PY-IT	bilayered interfaces	23.61	23.04	19.84	97.59	84.03
PM6:PY-IT:N2200	bilayered interfaces	23.65	23.11	20.70	97.72	87.53

*short-circuit condition, #maximal power output condition, $P_{\mathrm{diss}} = J_{\mathrm{ph}}^{*}/J_{\mathrm{sat}}$, $P_{\mathrm{coll}} = J_{\mathrm{ph}}^{\#}/J_{\mathrm{sat}}$.

Table S9. The hole (μ_{h}) and electron (μ_{e}) mobility of binary and ternary OSCs based on various OPV systems with different device structures.

Active layer	**Device structure**	μ_{h} (×10^{-4} cm^{2} V^{-1} s^{-1})	μ_{e} (×10^{-4} cm^{2} V^{-1} s^{-1})	$\mu_{\mathrm{h}}/\mu_{\mathrm{e}}$
PM6:L8-BO	control	6.14±0.22	4.51±0.24	1.36
PM6:L8-BO	bilayered interfaces	6.32±0.19	4.94±0.20	1.28
PM6:L8-BO:IT-M	bilayered interfaces	6.55±0.15	5.50±0.18	1.19
PM6:Y6	control	5.75±0.34	3.44±0.29	1.67
PM6:Y6	bilayered interfaces	5.91±0.27	3.81±0.31	1.55
PM6:Y6:IT-M	bilayered interfaces	6.09±0.18	4.26±0.23	1.43
PM6:N3	control	5.28±0.37	3.05±0.34	1.73
PM6:N3	bilayered interfaces	5.52±0.32	3.48±0.38	1.59
PM6:N3:IT-M	bilayered interfaces	5.88±0.25	3.97±0.30	1.48
PM6:BTP-eC9	control	6.36±0.26	4.38±0.28	1.45
PM6:BTP-eC9	bilayered interfaces	6.77±0.23	4.93±0.27	1.37
PM6:BTP-eC9:IT-M	bilayered interfaces	7.04±0.20	5.35±0.21	1.32
PM6:PY-IT	control	4.73±0.33	2.46±0.35	1.92
PM6:PY-IT	bilayered interfaces	4.94±0.28	2.68±0.31	1.84
PM6:PY-IT:N2200	bilayered interfaces	5.18±0.24	2.96±0.27	1.75

Table S10. Gaussian fitting results of trap states for PM6:L8-BO-based binary and ternary OSCs with different device structures before and after continuous illumination.

Active layers	N_{t} (cm^{-3} eV^{-1})	**σ (meV)**	E_{t} (eV)
Fresh binary control	3.78×10^{17}	22.8	0.130
Fresh binary bilayered	1.67×10^{17}	18.6	0.130
Fresh ternary bilayered	1.10×10^{17}	15.8	0.129
Aged binary control	1.39×10^{18}	32.4	0.131
Aged binary bilayered	7.20×10^{17}	26.1	0.131
Aged ternary bilayered	3.28×10^{17}	18.8	0.130

Table S11. Gaussian fitting results of trap states for PM6:Y6-based binary and ternary OSCs with different device structures before and after continuous illumination.

Active layers	N_t **(cm^{-3} eV^{-1})**	**σ (meV)**	E_t **(eV)**
Fresh binary control	7.05×10^{17}	22.0	0.131
Fresh binary bilayered	6.17×10^{17}	18.1	0.131
Fresh ternary bilayered	3.74×10^{17}	16.3	0.131
Aged binary control	6.77×10^{18}	38.7	0.133
Aged binary bilayered	4.88×10^{18}	29.8	0.132
Aged ternary bilayered	1.71×10^{18}	20.2	0.132

Table S12. Gaussian fitting results of trap states for PM6:N3-based binary and ternary OSCs with different device structures before and after continuous illumination.

Active layers	N_t **(cm^{-3} eV^{-1})**	**σ (meV)**	E_t **(eV)**
Fresh binary control	4.77×10^{17}	26.0	0.128
Fresh binary bilayered	4.14×10^{17}	22.7	0.127
Fresh ternary bilayered	3.49×10^{17}	15.2	0.127
Aged binary control	1.01×10^{18}	47.8	0.129
Aged binary bilayered	6.30×10^{17}	30.7	0.129
Aged ternary bilayered	5.13×10^{17}	20.2	0.128

Table S13. Gaussian fitting results of trap states for PM6:BTP-eC9-based binary and ternary OSCs with different device structures before and after continuous illumination.

Active layers	N_t **(cm^{-3} eV^{-1})**	**σ (meV)**	E_t **(eV)**
Fresh binary control	7.32×10^{17}	24.8	0.130
Fresh binary bilayered	5.64×10^{17}	17.0	0.130
Fresh ternary bilayered	4.53×10^{17}	15.7	0.129
Aged binary control	5.14×10^{18}	36.7	0.132
Aged binary bilayered	4.94×10^{18}	30.7	0.132
Aged ternary bilayered	1.67×10^{18}	20.2	0.131

Table S14. Fitting parameters of excitation density dependent TRPL dynamics at 880 nm for neat L8-BO film under continuous illumination of a 100 mW cm^{-2} white LED for 0 h.

Excitation density (mW cm^{-2})	N_0 **(a.u.)**	A_{nonrad} **(× 10^{-9} s^{-1})**	B_{rad} **(× 10^{-8} cm^3 s^{-1})**
10.2	1.055	0.888	1.516
20.6	1.026	1.038	1.989
31.6	1.031	1.165	2.129
41.2	1.029	1.321	2.195
51.5	1.034	1.383	2.800
60.4	1.037	1.441	2.947
71.7	1.024	1.581	3.003
82.2	1.041	1.731	3.389
90.7	1.033	1.810	4.051
101.3	1.051	1.967	5.681

Table S15. Fitting parameters of excitation density dependent TRPL dynamics at 880 nm for neat L8-BO film under continuous illumination of a 100 mW cm^{-2} white LED for 300 h.

Excitation density (mW cm^{-2})	N_0 (a.u.)	A_{nonrad} (× 10^{-9} s^{-1})	B_{rad} (× 10^{-8} cm^3 s^{-1})
10.2	1.075	2.195	11.307
20.6	1.049	3.022	11.007
31.6	1.043	3.504	10.471
41.2	1.031	3.702	10.994
51.5	1.074	4.380	10.670
60.4	1.036	4.411	10.702
71.7	1.053	4.887	10.853
82.2	1.018	4.970	11.046
90.7	1.021	5.034	11.306
101.3	1.068	5.252	11.759

Table S16. Fitting parameters of excitation density dependent TRPL dynamics at 900 nm for neat Y6 film under continuous illumination of a 100 mW cm^{-2} white LED for 0 h.

Excitation density (mW cm^{-2})	N_0 (a.u.)	A_{nonrad} (× 10^{-9} s^{-1})	B_{rad} (× 10^{-8} cm^3 s^{-1})
10.2	1.015	0.689	0.868
20.6	0.998	0.904	0.504
31.6	0.995	1.077	0.341
41.2	1.009	1.149	0.418
51.5	1.013	1.240	0.578
60.4	1.023	1.353	0.605
71.7	1.028	1.472	0.725
82.2	1.024	1.602	1.253
90.7	1.025	1.698	1.819
101.3	1.033	1.780	2.362

Table S17. Fitting parameters of excitation density dependent TRPL dynamics at 900 nm for neat Y6 film under continuous illumination of a 100 mW cm^{-2} white LED for 300 h.

Excitation density (mW cm^{-2})	N_0 (a.u.)	A_{nonrad} (× 10^{-9} s^{-1})	B_{rad} (× 10^{-8} cm^3 s^{-1})
10.2	1.007	1.209	1.399
20.6	1.013	1.655	0.931
31.6	1.007	1.815	0.839
41.2	1.001	1.899	0.668
51.5	1.014	1.918	0.779
60.4	1.019	1.956	1.086
71.7	1.009	1.985	1.228
82.2	1.025	2.008	1.744
90.7	1.043	2.092	2.442
101.3	1.045	2.133	2.856

Table S18. Fitting parameters of excitation density dependent TRPL dynamics at 900 nm for neat N3 film under continuous illumination of a 100 mW cm^{-2} white LED for 0 h.

Excitation density (mW cm^{-2})	N_0 **(a.u.)**	A_{nonrad} **(× 10^{-9} s^{-1})**	B_{rad} **(× 10^{-8} cm^{3} s^{-1})**
10.2	1.023	0.889	0.647
20.6	1.011	1.039	0.831
31.6	1.019	1.235	1.087
41.2	1.030	1.301	1.205
51.5	1.025	1.375	1.244
60.4	1.034	1.460	1.542
71.7	1.046	1.518	2.076
82.2	1.044	1.535	3.208
90.7	1.028	1.598	4.507
101.3	1.028	1.643	4.938

Table S19. Fitting parameters of excitation density dependent TRPL dynamics at 900 nm for neat N3 film under continuous illumination of a 100 mW cm^{-2} white LED for 300 h.

Excitation density (mW cm^{-2})	N_0 **(a.u.)**	A_{nonrad} **(× 10^{-9} s^{-1})**	B_{rad} **(× 10^{-8} cm^{3} s^{-1})**
10.2	1.039	2.591	0.201
20.6	1.028	3.036	0.443
31.6	1.018	3.159	0.582
41.2	1.024	3.245	0.858
51.5	1.030	3.408	0.919
60.4	1.027	3.528	1.242
71.7	1.040	3.608	1.589
82.2	1.035	3.799	1.846
90.7	1.041	3.922	2.928
101.3	1.041	4.299	4.631

Table S20. Fitting parameters of excitation density dependent TRPL dynamics at 900 nm for neat BTP-eC9 film under continuous illumination of a 100 mW cm^{-2} white LED for 0 h.

Excitation density (mW cm^{-2})	N_0 **(a.u.)**	A_{nonrad} **(× 10^{-9} s^{-1})**	B_{rad} **(× 10^{-8} cm^{3} s^{-1})**
10.2	1.039	0.678	1.239
20.6	1.028	0.955	1.301
31.6	1.018	0.965	1.370
41.2	1.024	1.136	1.598
51.5	1.030	1.246	1.926
60.4	1.027	1.392	2.290
71.7	1.040	1.559	3.019
82.2	1.035	1.687	4.031
90.7	1.041	1.883	5.124
101.3	1.041	2.194	7.691

Table S21. Fitting parameters of excitation density dependent TRPL dynamics at 900 nm for neat BTP-eC9 film under continuous illumination of a 100 mW cm^{-2} white LED for 300 h.

Excitation density (mW cm^{-2})	N_0 (a.u.)	A_{nonrad} (× 10^{-9} s^{-1})	B_{rad} (× 10^{-8} cm^3 s^{-1})
10.2	1.013	1.436	5.158
20.6	1.013	2.476	3.377
31.6	1.015	2.729	3.039
41.2	1.013	2.975	2.742
51.5	0.997	3.284	2.518
60.4	1.039	3.432	2.675
71.7	1.008	3.826	2.759
82.2	1.017	4.261	3.073
90.7	1.038	4.453	3.909
101.3	1.068	4.533	4.677

Table S22. Fitting parameters of excitation density dependent TRPL dynamics at 870 nm for neat PY-IT film under continuous illumination of a 100 mW cm^{-2} white LED for 0 h.

Excitation density (mW cm^{-2})	N_0 (a.u.)	A_{nonrad} (× 10^{-9} s^{-1})	B_{rad} (× 10^{-8} cm^3 s^{-1})
10.2	1.019	1.980	3.063
20.6	1.017	2.035	4.031
31.6	1.010	2.053	4.300
41.2	1.011	2.035	4.929
51.5	1.034	2.062	5.181
60.4	1.012	2.103	4.760
71.7	1.025	2.260	4.407
82.2	1.023	2.361	4.537
90.7	0.997	2.432	4.220
101.3	0.982	2.480	4.699

Table S23. Fitting parameters of excitation density dependent TRPL dynamics at 870 nm for neat PY-IT film under continuous illumination of a 100 mW cm^{-2} white LED for 300 h.

Excitation density (mW cm^{-2})	N_0 (a.u.)	A_{nonrad} (× 10^{-9} s^{-1})	B_{rad} (× 10^{-8} cm^3 s^{-1})
10.2	1.055	2.397	6.733
20.6	1.058	2.716	5.672
31.6	1.053	2.902	5.587
41.2	1.049	2.930	5.629
51.5	1.034	3.042	5.534
60.4	1.053	3.168	5.546
71.7	1.040	3.252	4.879
82.2	1.053	3.339	4.718
90.7	1.027	3.353	4.273
101.3	1.027	3.420	4.302

Table S24. Fitting parameters of energy density dependent TA dynamics at 860 nm for neat L8-BO film under continuous illumination of a 100 mW cm^{-2} white LED for 300 h.

Neat L8-BO film	**Energy density (μJ cm^{-2})**	**N_0 (a.u.)**	**k (× 10^{-9} s^{-1})**	**γ (× 10^{-9} cm^3 s^{-1})**
Fresh	3	0.950	5.05	1.99
	5	0.949	5.13	2.31
	9	0.913	5.29	2.82
	20	0.908	7.30	4.18
	40	0.897	12.32	6.49
Aged	3	0.941	14.13	2.62
	5	0.933	14.76	2.76
	9	0.943	16.26	4.35
	20	0.958	18.93	6.11
	40	0.932	23.27	11.90

Table S25. Summary of GIWAXS (010) π-π stacking peak information in the OOP direction for PM6:L8-BO-based binary and ternary blends before and after continuous illumination.

Sample	**$q_{z(010)}$ (nm^{-1})**	**d-spacing (nm)**	**FWHM (nm^{-1})**	**CCL (nm)**
Fresh binary blend	17.85	0.352	2.05	2.76
Aged binary blend	17.80	0.353	2.28	2.48
Fresh ternary blend	18.09	0.347	1.97	2.87
Aged ternary blend	18.01	0.349	2.11	2.68

References

1. H. Yin, L. Ma, Y. Wang, J. Huang, H. Yu, J. Zhang, P. C. Y. Chow, W. Ma, S. K. So and H. Yan, *Adv. Mater.*, 2019, **31**, 1903998.
2. H. Yin, K. L. Chiu, P. Bi, G. Li, C. Yan, H. Tang, C. Zhang, Y. Xiao, H. Zhang, W. Yu, H. Hu, X. Lu, X. Hao and S. K. So, *Adv. Electron. Mater.*, 2019, **5**, 1900497.
3. J. Song, C. Li, L. Zhu, J. Guo, J. Xu, X. Zhang, K. Weng, K. Zhang, J. Min, X. Hao, Y. Zhang, F. Liu and Y. Sun, *Adv. Mater.*, 2019, **31**, 1905645.
4. Y. Cai, Y. Li, R. Wang, H. Wu, Z. Chen, J. Zhang, Z. Ma, X. Hao, Y. Zhao, C. Zhang, F. Huang and Y. Sun, *Adv. Mater.*, 2021, **33**, 2101733.
5. L. Zhu, J. Zhang, Y. Guo, C. Yang, Y. Yi and Z. Wei, *Angew. Chem. Int. Ed.*, 2021, **60**, 15348-15353.
6. T. Handa, D. M. Tex, A. Shimazaki, A. Wakamiya and Y. Kanemitsu, *J. Phys. Chem. Lett.*, 2017, **8**, 954-960.
7. G. Delport, G. Chehade, F. Ledee, H. Diab, C. Milesi Brault, G. Trippe Allard, J. Even, J. S. Lauret, E. Deleporte and D. Garrot, *J. Phys. Chem. Lett.*, 2019, **10**, 5153-5159.
8. Q. Sun, C. Zhao, Z. Yin, S. Wang, J. Leng, W. Tian and S. Jin, *J. Am. Chem. Soc.*, 2021, **143**, 19128-19136.
9. S. Chandrabose, K. Chen, A. J. Barker, J. J. Sutton, S. K. K. Prasad, J. Zhu, J. Zhou, K. C. Gordon, Z. Xie, X. Zhan and J. M. Hodgkiss, *J. Am. Chem. Soc.*, 2019, **141**, 6922-6929.
10. S. Khelifi, K. Decock, J. Lauwaert, H. Vrielinck, D. Spoltore, F. Piersimoni, J. Manca, A. Belghachi and M. Burgelman, *J. Appl. Phys.*, 2011, **110**, 094509.
11. S. Liu, J. Yuan, W. Deng, M. Luo, Y. Xie, Q. Liang, Y. Zou, Z. He, H. Wu and Y. Cao, *Nat. Photon.*, 2020, **14**, 300-305.
12. X. Chen, D. Qian, Y. Wang, T. Kirchartz, W. Tress, H. Yao, J. Yuan, M. Hülsbeck, M. Zhang, Y. Zou, Y. Sun, Y. Li, J. Hou, O. Inganäs, V. Coropceanu, J. Bredas and F. Gao, *Nat. Energy*, 2021, **6**, 799-806.

13. B. Fan, X. Du, F. Liu, W. Zhong, L. Ying, R. Xie, X. Tang, K. An, J. Xin, N. Li, W. Ma, C. J. Brabec, F. Huang and Y. Cao, *Nat. Energy*, 2018, **3**, 1051-1058.
14. L. Ye, K. Weng, J. Xu, X. Du, S. Chandrabose, K. Chen, J. Zhou, G. Han, S. Tan, Z. Xie, Y. Yi, N. Li, F. Liu, J. M. Hodgkiss, C. J. Brabec and Y. Sun, *Nat. Commun.*, 2020, **11**, 6005.
15. P. Bi, S. Zhang, Z. Chen, Y. Xu, Y. Cui, T. Zhang, J. Ren, J. Qin, L. Hong, X. Hao and J. Hou, *Joule*, 2021, **5**, 2408-2419.
16. L. Zhan, S. Li, Y. Li, R. Sun, J. Min, Z. Bi, W. Ma, Z. Chen, G. Zhou, H. Zhu, M. Shi, L. Zuo and H. Chen, *Joule*, 2022, **6**, 662-675.
17. U. Rau, B. Blank, T. C. M. Müller and T. Kirchartz, *Phy. Rev. Appl.*, 2017, **7**, 044016
18. Y. Wang, D. Qian, Y. Cui, H. Zhang, J. Hou, K. Vandewal, T. Kirchartz and F. Gao, *Adv. Energy Mater.*, 2018, **8**, 1801352.